



저작자표시-비영리-변경금지 2.0 대한민국

이용자는 아래의 조건을 따르는 경우에 한하여 자유롭게

- 이 저작물을 복제, 배포, 전송, 전시, 공연 및 방송할 수 있습니다.

다음과 같은 조건을 따라야 합니다:



저작자표시. 귀하는 원저작자를 표시하여야 합니다.



비영리. 귀하는 이 저작물을 영리 목적으로 이용할 수 없습니다.



변경금지. 귀하는 이 저작물을 개작, 변형 또는 가공할 수 없습니다.

- 귀하는, 이 저작물의 재이용이나 배포의 경우, 이 저작물에 적용된 이용허락조건을 명확하게 나타내어야 합니다.
- 저작권자로부터 별도의 허가를 받으면 이러한 조건들은 적용되지 않습니다.

저작권법에 따른 이용자의 권리는 위의 내용에 의하여 영향을 받지 않습니다.

이것은 [이용허락규약\(Legal Code\)](#)을 이해하기 쉽게 요약한 것입니다.

[Disclaimer](#)

공학박사 학위논문

**Design of Reduced Titania Cathode for  
High-Performance Li-Air Batteries**

고성능 리튬 공기 전지를 위한  
환원된 이산화티타늄 기반의 전극 설계

2017년 2월

서울대학교 대학원  
재료공학부  
강 준 현

# Design of Reduced Titania Cathode for High-Performance Li-Air Batteries

고성능 리튬 공기 전지를 위한  
환원된 이산화티타늄 기반의 전극 설계

지도교수 박 병 우

이 논문을 공학박사 학위논문으로 제출함  
2017 년 2 월

서울대학교 대학원  
재료공학부  
강 준 현

강준현의 박사학위논문을 인준함  
2017 년 2 월

|         |              |     |
|---------|--------------|-----|
| 위 원 장   | <u>오 승 모</u> | (인) |
| 부 위 원 장 | <u>박 병 우</u> | (인) |
| 위 원     | <u>남 승 훈</u> | (인) |
| 위 원     | <u>박 용 준</u> | (인) |
| 위 원     | <u>강 기 석</u> | (인) |

Ph.D. Thesis

**Design of Reduced Titania Cathode for  
High-Performance Li-Air Batteries**

**Joonhyeon Kang**

February 2017

Department of Materials Science and Engineering

Seoul National University

## **Abstract**

While human society is becoming progressively more reliant upon energy, one of the most important natural resources, petroleum, has been rapidly diminishing now, and finally, will be exhausted near future. Aside from this, dramatic increase in use of fossil fuels for automobiles, power plants, and factories is giving rise to greenhouse effect or global warming, which comes to be a direct threat to mankind. In such situations, there is great attention to development of environment-friendly power sources such as solar cells, fuel cells, and lithium-ion batteries. Especially, electric vehicles (EVs) or hybrid electric vehicles (HEVs) based on fuel cells or Li-ion batteries are expected to alleviate such issues according to the degree of replacement for the conventional fossil fuel-powered vehicles. For the complete transition to the electric vehicles, longer mileage and stability should be guaranteed, which are strongly dependent on the electrochemical system and electrode materials, but it cannot be satisfied by current stage of Li-ion battery technologies.

As alternatives, metal-air batteries and fuel cells operate basically on a similar fashion which include chemical reactions between metal (or hydrogen) and oxygen. Since their electrochemical systems are based on reactions from lightweight elements, theoretical energy densities are relatively high compared to that of Li-ion batteries which generally contain heavy transition metals in the cathode. In the cathodes of both systems, oxygen-reduction reaction (ORR) occurs in common, and therefore understanding of oxygen reduction reaction (ORR) is of significant importance in realizing these advanced electrochemical technologies.

Although fuel cells and Li-air battery systems mutually use oxygen-reduction reactions, the detailed reaction mechanisms, products and following properties are quite

different from each other. Therefore, in order to achieve high energy density, stability, and thereby to realize the practical use of these future technologies, suitable strategies have to be applied.

In this thesis, based on the fundamental understanding of ORR mechanisms in aqueous/non-aqueous media, suitable design principles for the electrodes are suggested for fuel cells and Li-air batteries, respectively. Both systems use oxygen as a fuel, and include (pseudo-)catalytic reactions which are strongly dependent upon the electrode properties. While ORR in fuel cells produces water as a soluble product, the operation of Li-air batteries leads to the accumulation of insoluble solid  $\text{Li}_2\text{O}_2$  on the cathode side. Therefore, each system requires different strategies to enhance the electrochemical performances. In fuel cells, designing a new catalyst or enhancing an established catalyst is a main issue. The design rule for a new catalyst based on transition metals and following development of advanced catalyst will be presented. Finally, based on the perception from catalytic phenomena in fuel cells, effective air-cathode for Li-air batteries is suggested, as well.

In Chapter 1, basic concept for catalytic reactions and fuel cells are introduced. Subsequently, the strategies for enhancing catalytic activity for oxygen-reduction reaction and methanol oxidation reaction are presented. Then, ORR in aqueous/non-aqueous electrolytes are compared, with brief introduction of Li-air batteries. Finally, critical issues in Li-air batteries and promising solutions for overcoming property-limiting issues are suggested.

In Chapter 2, for the understanding of catalytic reactions and role of the catalyst, a relationship between the catalytic activity and electronic structure of Pt surface was investigated. By systematically controlling the electrode potential, I simplified the reaction paths, excluding other unfavorable effects, and thereby obtained only the methanol-dehydrogenation activity in terms of the electronic structure of Pt surface. I

observed that methanol-dehydrogenation activity of Pt decreases when the position of the *d*-band center relative to the Fermi-level is lower, and this fundamental relation provides advanced insight into the design of an optimal catalyst as the anode for direct-methanol fuel cells.

In Chapter 3, based on the understanding in the catalytic reactions from fuel cells, and considering the discharge/charge mechanisms of Li-air batteries, I tried to design an efficient and stable cathode for Li-air batteries. I fabricated oxygen-deficient titanium dioxide with hierarchically-ordered porous structure by the hydrogen thermal treatment as a carbon- and binder-free cathode, demonstrating high energy density and stability. With the high electronic conductivity derived from oxygen vacancies or  $\text{Ti}^{3+}$  ions, this unique electrode has large surface area with the micron-sized empty voids for the effective accommodation of discharge products and for rapid transport of reaction molecules without the electrode being clogged. Therefore, large discharge product ( $\text{Li}_2\text{O}_2$ ) grown from solution could be effectively charged by incorporating a soluble catalyst into the electrode, resulting in a very small polarization.

**Keywords:** fuel cells, Li-air batteries, oxygen-reduction reaction, catalytic reaction, catalyst, transition metal, aqueous electrolyte, non-aqueous electrolyte, platinum, electronic structure, methanol-dehydrogenation reaction, discharge, charge, cathode, titanium dioxide, soluble catalyst

**Student Number: 2010-20574**

# Table of Contents

|   |              |
|---|--------------|
| <b>Abstract</b>   | <b>i</b>     |
| <b>List of Figures</b>  | <b>vii</b>   |
| <b>List of Table</b>  | <b>xviii</b> |
| <b>Chapter 1. Overview</b>  | <b>1</b>     |
| <b>1.1. Introduction to Fuel Cells</b>  | <b>3</b>     |
| <b>1.2. Fundamental Understanding of Electrocatalyst</b>  | <b>7</b>     |
| <b>1.3. Modification of Catalytic Activity</b>  | <b>15</b>    |
| <b>1.4. Introduction to Li-Air Batteries</b>  | <b>20</b>    |
| <b>1.5. Heterogeneous Catalysis in Li-Air Batteries</b>   | <b>22</b>    |
| <b>1.6. Issues in Air-Cathodes for Li-Air Batteries</b>   | <b>24</b>    |
| <b>1.7. Design Strategy for High-Performance Air-Cathodes</b>   | <b>29</b>    |
| <b>1.8. References</b>  | <b>36</b>    |
| <b>Chapter 2. Electronic Effect in Methanol Dehydrogenation on Pt Surface:<br/>    Potential Control during Methanol Electrooxidation</b> | <b>41</b>    |
| <b>2.1. Introduction</b>  | <b>41</b>    |
| <b>2.2. Experimental Section</b>  | <b>45</b>    |
| <b>2.3. Results and Discussion</b>  | <b>46</b>    |
| <b>2.4. Conclusions</b>   | <b>62</b>    |
| <b>2.5. References</b>  | <b>63</b>    |

|  |            |
|--|------------|
| <b>Chapter 3. Breathable Carbon-Free Electrode: Black TiO<sub>2</sub> with Hierarchically Ordered Porous Structure for Stable Li-Air Batteries</b> | <b>72</b>  |
| <b>3.1. Introduction</b>   | <b>72</b>  |
| <b>3.2. Experimental Section</b>   | <b>76</b>  |
| 3.2.1. Materials Preparation   |            |
| 3.2.2. Materials Characterization  |            |
| 3.2.3. Electrochemistry  |            |
| <b>3.3. Results and Discussion</b>   | <b>79</b>  |
| 3.3.1. Synthesis and Characterization of Hierarchically-Ordered Porous Black TiO <sub>2</sub> electrode  |            |
| 3.3.2. Electrochemical Properties of HOP- <i>b</i> TiO <sub>2</sub> Electrode  |            |
| 3.3.3. Combination of electrode architecture and redox mediator  |            |
| 3.3.4. Origin of High Stability of Black TiO <sub>2</sub> Electrodes   |            |
| <b>3.4. Conclusions</b>  | <b>111</b> |
| <b>3.5. References</b>   | <b>112</b> |
| <b>Appendix</b>  | <b>118</b> |
| <b>A. 1. Synergistic Improvement of Oxygen Reduction Reaction on Gold/Cerium-Phosphate Catalysts</b>   | <b>118</b> |
| A.1.1. Introduction  | 118        |
| A.1.2. Experimental Section  | 120        |
| A.1.3. Results and Discussion  | 122        |
| A.1.4. Conclusions   | 132        |
| A.1.5. References  | 133        |

|              |   |            |
|--------------|---|------------|
| <b>A. 2.</b> | <b>List of Publications and Presentations</b> | <b>138</b> |
|              | <b>A.2.1. Publications</b>                    | <b>138</b> |
|              | <b>A.2.2. Presentations</b>                   | <b>142</b> |
|              | <b>국문 초록</b>                                  | <b>146</b> |

# List of Figures

## Chapter 1.

Fig. 1-1. (Color) Ragone chart representing specific energy versus specific power for various energy conversion systems compared to an internal combustion engine. From reference [1].

Fig. 1-2. (Color) Scheme of the electrochemical conversion system (fuel cells) with hydrogen oxidation and oxygen reduction and with methanol oxidation and oxygen reduction, as the combination of anode reaction and cathode reaction.

Fig. 1-3. Schematic representation of the Gibbs energy curves for the reaction  $A + e \rightarrow B \rightarrow C$ . It is a non-spontaneous reaction that requires an input of energy. Intermediate  $B$  is adsorbed on the catalyst surface and energy state changes from state (1) to state (2). The activation barriers for two situations are indicated as (a) and (b), respectively. From reference [6].

Fig. 1-4. (Top) Exchange current densities for hydrogen evolution reaction on various metal surface as a function of the hydrogen chemisorption energy per atom,  $\Delta E_H$ , (Bottom) volcano type activity as a function of the free energy for hydrogen adsorption,  $\Delta G_{H^*}$ . From reference [7].

Fig. 1-5. (Color) Bond formation at a transition-metal surface. Schematic illustration of the formation of a chemical bond between an adsorbate valence level and the  $s$  and  $d$  states of a transition-metal surface. The bond is characterized by the degree to which the antibonding state between the adsorbate state and the metal  $d$  state is occupied. From reference [8].

Fig. 1-6. Illustration of the use of the  $d$ -band model. Electrochemically measured changes in the hydrogen adsorption energy ( $E_{\text{SCE}}$ ) for Pd overlayers on various metals. It scales well with the calculated shift of the  $d$ -band center ( $\delta\varepsilon_d$ ). From reference [8].

Fig. 1-7. (Color) Charge difference for (a) a gold cluster on a perfect MgO surface, (b) a gold cluster on an oxygen deficient MgO surface, and (c) with adsorbed reactants. From reference [17].

Fig. 1-8. Scheme of the formation of hydrous iron phosphates with respect to anhydrous phase: the variscite orthorhombic ( $Pbca$ )  $\text{FePO}_4 \cdot 2\text{H}_2\text{O}$  and tridymite triclinic ( $P1$ )  $\text{FePO}_4$ . From reference [18].

Fig. 1-9. (Color) Schematic representation of non-aqueous Li-air battery system.

Fig. 1-10. (Color) Schematic representation of degradation mechanism in carbon electrodes. Carbon is relatively stable below 3.5 V (vs. Li/LI<sup>+</sup>), but is unstable on charging above 3.5 V (in the presence of Li<sub>2</sub>O<sub>2</sub>). Electrolyte decomposition occurs during discharge/charge and is promoted on carbon. From reference [29].

Fig. 1-11. SEM images of CNT powders of: (a) as-prepared, and (b) after the first discharge. From reference [32].

Fig. 1-12. (Color) (a) Galvanostatic discharge and charge profile of a Li-O<sub>2</sub> cell employing Ti<sub>4</sub>O<sub>7</sub> nanomaterial as cathode. (b) Scheme showing the gradual gradient of sub-stoichiometric TiO<sub>2-x</sub> formed at the surface of the Magneli Ti<sub>4</sub>O<sub>7</sub> cathode host in the Li-air cell that acts as a thin passivating interphase. From reference [37].

Fig. 1-13. (Color) (a) Schematic of the O<sub>2</sub> reduction mechanism in an aprotic solvent containing Li<sup>+</sup> showing the surface pathway and solution pathway. The table shows the donor number of various solvents. (b) SEM image showing the Li<sub>2</sub>O<sub>2</sub> morphology obtained in DMSO electrolyte. From reference [39].

Fig. 1-14. (Color) Catalytic mechanism of the OER with a redox mediator as the soluble catalyst in an aprotic Li-O<sub>2</sub> battery. From reference [42].

## Chapter 2.

- Fig. 2-1. (Color) X-ray diffraction of Pt and Pt/FePO<sub>4</sub> nanocomposites to determine the grain size of Pt nanocrystals from the  $\Delta k$  vs.  $k$  plot.
- Fig. 2-2. (Color) Cyclic voltammograms of the Pt and Pt/FePO<sub>4</sub>-nanocomposite electrodes with various sputtering powers of FePO<sub>4</sub> in 0.1 M HClO<sub>4</sub>.
- Fig. 2-3. (Color) Cyclic voltammograms of Pt and FePO<sub>4</sub> in 0.1 M HClO<sub>4</sub> + 0.1 M CH<sub>3</sub>OH at a scan rate of 50 mV/s.
- Fig. 2-4. (Color) Cyclic voltammograms including the available potential region of the Au-O chemisorption/desorption reaction. The Au and Au/AlPO<sub>4</sub> nanocomposite electrodes were examined in an oxygen-free (nitrogen-purged) 0.5 M H<sub>2</sub>SO<sub>4</sub> solution at a scan rate of 50 mV/s.
- Fig. 2-5. (Color) Fast scan (3 V/s) cyclic voltammogram of Pt showing the CO<sub>ad</sub> stripping peak (1st cycle) and subsequent 3 cycles (total 4 cycles), measured from potential control (Fig. 1) in 0.1 M HClO<sub>4</sub> + 0.1 M CH<sub>3</sub>OH (red solid line). The second and subsequent scans are almost identical, and also similar to the CV curve in 0.1 M HClO<sub>4</sub> (dotted line) except for slight current around 0.7 V from methanol-decomposition process forming soluble species [46]. Thus, the second scan of CV was used as background to obtain the charge corresponding to the oxidation of CO<sub>ad</sub>.

- Fig. 2-5. (Color) Cyclic voltammograms including the available potential region of the Au-O chemisorption/desorption reaction. The Au and Au/AlPO<sub>4</sub> nanocomposite electrodes were examined in an oxygen-free (nitrogen-purged) 0.5 M H<sub>2</sub>SO<sub>4</sub> solution at a scan rate of 50 mV/s.
- Fig. 2-6. (Color) CO coverage vs. time for each Pt surface prepared by different sputtering powers of FePO<sub>4</sub>. The CO<sub>ad</sub> coverage was obtained from CV scan at the rate of 3 V/s in 0.1 M HClO<sub>4</sub> + 0.1 M CH<sub>3</sub>OH (Fig. 2), and fitted from Eq. (4).
- Fig. 2-7. (Color) Plot of  $\alpha$  as a function of FePO<sub>4</sub> sputtering power. In Eq. (4),  $\alpha$  reflects the effect of repulsive CO interactions on the rate of methanol dehydrogenation; we did not find any considerable variations or tendency in  $\alpha$  for different samples. So,  $\alpha$  was obtained from each data, and the average value of  $\alpha$  ( $19.2 \pm 0.9 \text{ ML}^{-1}$ ) was used to obtain the rate constant  $k_a$  for methanol dehydrogenation with the fitting from Fig. 2-6.
- Fig. 2-8. (Color) Rate constant for methanol dehydrogenation on Pt surfaces as a function of the  $d$ -band center, as measured from the valence-band spectra in Fig. 2-9 (relative to pure Pt).
- Fig. 2-9. (Color) The valence-band spectra for Pt and Pt/FePO<sub>4</sub> composites with various sputtering powers of FePO<sub>4</sub>.

Fig. 2-10. (Color) Rate constant for methanol dehydrogenation on Pt surfaces as a function of the  $d$ -band center, as measured from the valence-band spectra in Fig. S5 (relative to pure Pt).

### Chapter 3.

Fig. 3-1. (Color) Schematic illustration on the preparation for carbon-free electrode, composed of hierarchically-ordered porous black  $\text{TiO}_2$  (HOP- $b\text{TiO}_2$ ) on a Ni mesh. PS and OP- $\text{TiO}_2$  denote the polystyrene bead and ordered-porous  $\text{TiO}_2$  before  $\text{H}_2$  thermal treatment, respectively.

Fig. 3-2. SEM images of polystyrene filled Ni mesh (PS/Ni mesh) used as a template for the fabrication of ordered porous  $\text{TiO}_2$ .

Fig. 3-3. SEM images of the HOP- $b\text{TiO}_2$  in various magnifications.

Fig. 3-4. (Color) SEM images and X-ray diffraction patterns of (a) the OP- $\text{TiO}_2$  (before  $\text{H}_2$  thermal reduction) and (b) the HOP- $b\text{TiO}_2$  (after  $\text{H}_2$  thermal reduction). (c) XPS spectra in the Ti  $2p$  region for the black  $\text{TiO}_2$  and control  $\text{TiO}_2$  (rutile phase). (d) Raman spectra for the black  $\text{TiO}_2$  and control  $\text{TiO}_2$ .

Fig. 3-5. (Color) Ti  $L$ -edge soft x-ray absorption spectroscopy (sXAS). Total electron yield (TEY) and partial electron yield (PEY) spectra of black  $\text{TiO}_2$  and control  $\text{TiO}_2$  are displayed with fitted lines. The area ratios of fitted peaks for  $e_g$  to  $t_{2g}$  are also present in the table.

Fig. 3-6. (Color) XPS spectra in the O 1s region for the black TiO<sub>2</sub> and reference rutile TiO<sub>2</sub>. A shoulder peak of the black TiO<sub>2</sub> (marked by a circle) corresponds to the OH species, indicating that the relatively larger amount of OH species are incorporated to the black TiO<sub>2</sub> surface than that of control TiO<sub>2</sub>.

Fig. 3-7. (Color) Size distribution of TiO<sub>2</sub> grains in HOP-*b*TiO<sub>2</sub>.

Fig. 3-8. (Color) Pellets of TiO<sub>2</sub> and black TiO<sub>2</sub> for the measurement of 4-point probe.

Fig. 3-9. (Color) (a) Discharge/charge profiles of the HOP-*b*TiO<sub>2</sub> electrode at a rate of 0.05 mA cm<sup>-2</sup>. (b) Discharge/charge profiles of HOP-*b*TiO<sub>2</sub> at a rate of 0.05 mA cm<sup>-2</sup>, with the specific capacity limited to 1000 mAh g<sup>-1</sup>. (c) Cyclability and terminal voltages of the HOP-*b*TiO<sub>2</sub>. (d) SEM images of the HOP-*b*TiO<sub>2</sub> electrode after first discharge to 1000 mAh g<sup>-1</sup>, (e) after fully discharged, and (f) after recharged. Marked by solid circles (d-e) are correspondent states in the voltage profiles in Fig. 3(a). (g) Schematic representations of growing tendency of Li<sub>2</sub>O<sub>2</sub> that is guided by the ordered electrode architecture. (h) STEM image of the stacked Li<sub>2</sub>O<sub>2</sub> toroids in a fully-discharged state.

Fig. 3-10. SEM images of the HOP-*b*TiO<sub>2</sub> (a) at a discharged state to 1000 mAh g<sup>-1</sup> and (b) at fully discharged state.

Fig. 3-11. TEM images for the HOP-*b*TiO<sub>2</sub> electrode with the discharge product (a) at a discharged state to 1000 mAh g<sup>-1</sup> and (b) at fully discharged state.

Fig. 3-12. (Color) (a) SEM image and (b) XPS spectra in the Li 1s region of HOP-*b*TiO<sub>2</sub> electrode after cell death.

Fig. 3-13. (Color) (a) First discharge/charge profiles of the HOP-*b*TiO<sub>2</sub> with and without LiI catalyst. (b) Selected voltage profiles of the HOP-*b*TiO<sub>2</sub> with LiI catalyst (1st and 340th cycle). (c) Schemes representing the effect of electrode architecture (HOP-*b*TiO<sub>2</sub> and nanoparticle electrode) on the activity of a redox mediator. (d) Cyclability and terminal voltages of the HOP-*b*TiO<sub>2</sub> with and without LiI catalyst. All of the electrodes are discharged and charged at a rate of 0.05 mA cm<sup>-2</sup>, with the specific capacity limited to 1000 mAh g<sup>-1</sup>.

Fig. 3-14. (Color) SEM images of (a) the pristine nanoporous black TiO<sub>2</sub> (NP-*b*TiO<sub>2</sub>) and (b) after discharge to 1000 mAh g<sup>-1</sup>. (c) Voltage profiles showing the effect of electrode architecture on the activity of LiI catalyst (HOP-*b*TiO<sub>2</sub> and NP-*b*TiO<sub>2</sub>).

Fig. 3-15. (Color) Photographs of the pristine HOP-*b*TiO<sub>2</sub> electrode and cycled HOP-*b*TiO<sub>2</sub> electrode after cell death. The retained black color even after long cycles is indicative of the preserved Ti<sup>3+</sup> ions and oxygen vacancies in the crystal structure.

Fig. 3-16. (Color) XPS spectra in the (a) Ti  $2p$  and (b) Li  $1s$  region for the HOP- $b\text{TiO}_2$  at pristine, discharged ( $1000 \text{ mAh g}^{-1}$ ), and recharged states. TEM images of the HOP- $b\text{TiO}_2$  electrode at different states that are correspondent with the XPS spectra: (c) pristine, (d) discharged, and (e) recharged state.

Fig. 3-17. TEM images of the black  $\text{TiO}_2$  with various  $\text{H}_2$ -treatment time of 0 h, 10 h, and 40 h. As  $\text{H}_2$ -annealing time increases, amorphous surface layers become thicker.

Fig. 3-18. (Color) A schematic representation with TEM images summarizing functions of the HOP- $b\text{TiO}_2$  electrode.

## Appendix 1.

- Fig. A1-1. (Color) X-ray diffraction of the Au thin film and Au/CePO<sub>4</sub> nanocomposites. The ideal peak positions and intensities for Au (JCPDS 04-0784) are marked at the bottom.
- Fig. A1-2. (Color) Underpotential deposition (UPD) experiments of lead on Au and Au/CePO<sub>4</sub> nanocomposites. The desorption potential of lead on Au (111), (100), and (110) are marked with dashed lines.
- Fig. A1-3. (Color) Oxygen-reduction activities for the Au, Pt, and CePO<sub>4</sub> thin films, and Au/CePO<sub>4</sub> nanocomposites. The calculated current densities corresponding to two-electron and four-electron reactions are also marked, respectively.
- Fig. A1-4. (Color) Au 4f XPS spectra for the Au and Au/CePO<sub>4</sub> nanocomposite electrodes. The dashed lines are from the standard Au.
- Fig. A1-5. (Color) ORR-enhancement mechanisms. (a-c) Hydrogen-peroxide reduction activities measured by chronoamperometry by adding H<sub>2</sub>O<sub>2</sub> at 100 s. (a) The Au, CePO<sub>4</sub>, and Au/CePO<sub>4</sub> nanocomposites at 0.709 V (vs. RHE). (b-c) The pure CePO<sub>4</sub> and AlPO<sub>4</sub> at different applied potentials. (d) ORR-activity comparisons between the Au/CePO<sub>4</sub> and Au/AlPO<sub>4</sub> nanocomposites. (e-f) Schemes representing the ORR mechanisms on (e) Au/CePO<sub>4</sub> and (f) Au/AlPO<sub>4</sub>.

# List of Table

## Chapter 2.

Table 2-1. (Color) Grain size of crystalline Pt at various sputtering powers of FePO<sub>4</sub>, obtained from the  $\Delta k$  vs.  $k$  plot of Fig. 2-1.

## Chapter 1. Overview

With depletion of traditional fossil fuels and increasing demands for electric vehicles (EVs) or hybrid electric vehicles (HEV), galvanic cells utilizing reactions between metal (or hydrogen) and oxygen, such as fuel cells and Li-air batteries, are generating substantial interest due to their high energy density (Fig. 1-1) and its environment-friendliness [1]. Both systems are based on the conversion of chemical energy into the electrical energy by separating the paths of the two charge carriers (e. g. ions and electrons) and by rendering electrochemical redox-reactions in positive and negative electrodes. Especially, in the positive electrode of both systems, oxygen-reduction reactions (ORR) take place while the oxygen-evolution reaction is only incorporated in Li-air batteries during charge. Depending on the type of electrolytes, fuel cells and Li-air batteries are classified into several categories, and consequent ORR mechanisms and reaction products are quite different. Excluding the use of solid electrolyte, fuel cells generally operate by aqueous electrolyte (acidic or alkaline), while Li-air batteries use both aqueous and non-aqueous (aprotic) media, although aprotic Li-air batteries are of current interest.

In this chapter, reaction mechanisms of fuel cells and aprotic Li-air batteries are briefly introduced, and compared with special focus on the ORR in cathode side. Next, current problems and limitations on the application of fuel cells and Li-air batteries are discussed. Finally, based on the understanding of each system, various efforts in these fields of research are summarized with suggested strategies to overcome the barriers and to realize high theoretical energy densities.

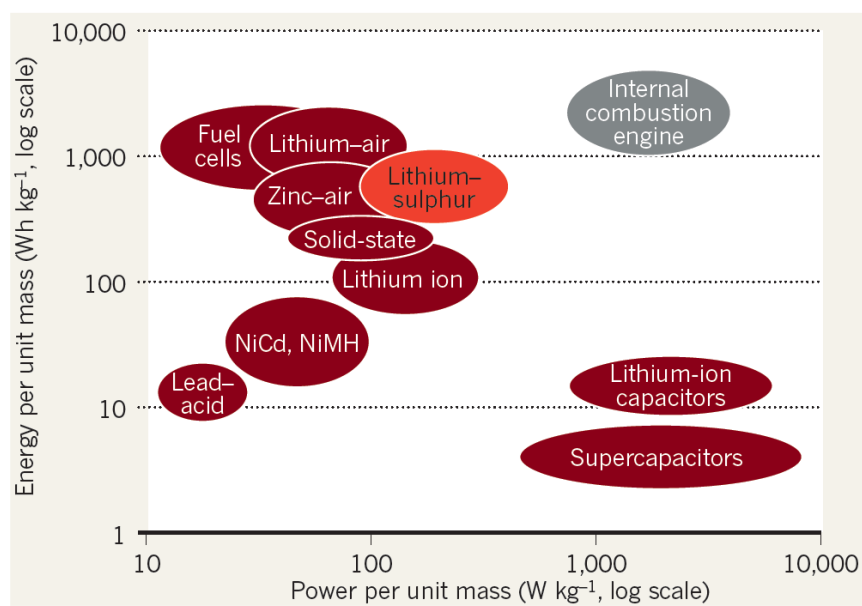


Fig. 1-1 (Color) Ragone chart representing specific energy versus specific power for various energy conversion systems compared to an internal combustion engine. From reference [1].

## **1.1. Introduction to Fuel Cells**

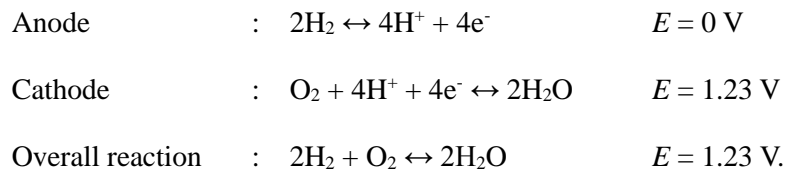
As energy consumption is dramatically increased, and green-house effect or global warming are raised as critical issues for future generations, various alternatives for replacing the internal-combustion engine that uses fossil fuels are of tremendous interests. Such alternatives include solar energy, wind energy, nuclear source, chemical energy conversion, and etc.

Among various approaches, electrochemical conversion system is one of the most efficient ways to substitute the existing combustion system with some obvious advantages. The electrochemical cell involves the conversion of chemical energy into electrical energy, and vice versa. The driving force that cause electrochemical transduction to occur in electrochemical system is the chemical energy difference between the reactant and product, which generates the corresponding potential difference in an electrochemical cell.

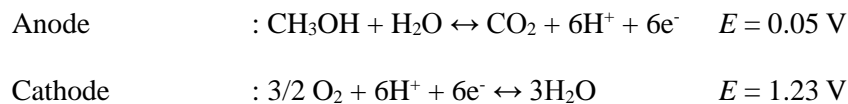
As an electrochemical conversion system, fuel cells convert the chemical energy of a fuel into electricity by the electrochemical reactions with generation of almost no pollutants, and are therefore regarded as one of the most promising electrical generators for various applications. Fuel cells can generally be classified by types of electrolyte, and following five major types of fuel cells are polymer electrolyte fuel cell or proton exchange membrane fuel cell (PEMFC), alkaline fuel cell (AFC), phosphoric acid fuel cell (PAFC), molten carbonate fuel cell (MCFC), and solid oxide fuel cell (SOFC).

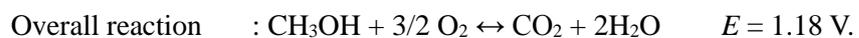
Among the various kinds of fuel cells, polymer electrolyte membrane fuel cells (PEMFCs) are considered to be most commercially-available due to its low operating temperature. This type of fuel cells are based on the hydrogen oxidation (0 V vs.

reversible hydrogen potential (RHE)) and the oxygen reduction reaction (1.23 V vs. RHE) with water product, as shown in Fig. 1-2. Chemical energy of hydrogen and oxygen can be converted to electrical energy via each electrochemical redox reaction [2]. Typically, proton-exchange-membrane (Nafion®) is used as the electrolyte for low temperature operating types. Such membrane shows ionic-conductivity when it has enough humidity and proton ions (low pH). Overall cell reaction occurs as follows:



The cathode side takes advantage of direct supply of oxygen from air, although further improvement is necessary for the development of stable and active oxygen catalysts [3]. On the other hands, the hydrogen fuel is a potential hazard because of the probability of explosion and difficulty in storage and transportation with low volumetric energy density. Therefore, alternative fuels for anode are needed to be explored such as alcohol, formic acid, borohydride, small organic molecules, and etc. Above all, methanol is firstly noted, and the direct methanol fuel cell (DMFC) is considered as usable energy source for portable devices due to the various advantages of methanol such as higher volumetric density, and easy handling of liquid phase [5]. The overall reactions of DMFC are as follows:





The electrochemical reactions that occur on the both cathode and anode of fuel cells include breaking and formation of chemical bonds, and their kinetics vary dramatically upon different electrode materials or electrocatalysts. Therefore, in order to make the fuel cells more practical, development of inexpensive, stable, and active catalysts is indeed necessary. For the systematic design of catalysts rather than trial-and-error approach, it is important to develop a fundamental understanding of the catalytic reactions on different electrode materials.



## 1.2. Fundamental Understanding of Electrocatalyst

Generally, catalyst accelerates a rate of reaction by lowering an activation barrier, and catalytic properties originate from an adsorption phenomena. Catalyst can provide an adsorption site for reactants and the adsorbed reactants can be considered as the intermediate state during whole reaction process. The different intermediate states on catalysts leads to different reaction paths, which results in the variation of an activation barrier.

Catalytically-effective adsorption is chemical adsorptions, and is distinguished from such physical adsorptions as van der Waals interactions. Chemical adsorption leads to the relatively strong interactions (several eV) by sharing electronic density (forming a bond) or by transferring charges between reactant molecules and catalyst surface [6]. These strong electronic interactions modify the orbital of reactant molecule as well as the geometry of reactant molecule. Therefore, effective catalysis by dissociative chemical adsorptions and reaction path deviations can occur with mixing or interactions between orbital of objective reactant and electronic structure of catalyst surface.

Deviation of activation barrier depends on energy state of adsorbed species as shown in Fig. 1-3. The adsorbed species has a lower energy state and activation barrier of adsorption ( $A$  to  $B$ ) is decreased and the adsorption takes place at higher rate. In this situation, activation barrier of desorption ( $B$  to  $C$ ) is increased, and further adsorption is hindered with firstly adsorbed species on the active site of catalyst, thus rate of overall reaction is limited [6]. These tendencies are represented with a volcano type curve as shown in Fig. 1-4. Therefore, the suitable heat of adsorption is considered a key factor

for the change of catalytic activity [7]. Therefore, the description of the chemical bond between a catalyst surface and a reactant molecule is the fundamental basis for understanding surface chemical reactivity and catalysis. In this respect, extensive studies has been done on the adsorption of simple atoms and molecules onto transition-metal surfaces.

The *d*-band model has proven particularly useful in understanding bond formation and trends in surface reactivity (catalytic activity) among the various transition metals. The *d*-band model is an approximate description of the bond formation on a transition-metal surface, as illustrated in Fig. 1-5. It describes the interaction between adsorbate valence states and the valence *s* and *d* states of a transition-metal surface. The coupling of a molecule state to the broad metal *s* band leads to a broadening and shift of the adsorbate states. Since all the transition metals have a half-filled *s* band and the *s* band is broad, there will be only small differences in this interaction for the transition metals [8].

The different reactivity between different transition metals comes from the formation of bonding and antibonding states between the (renormalized) valence states and the metal *d* states. The strength of the bond is determined by the filling of the antibonding states, and this filling is determined by the energy of the antibonding states relative to the Fermi level, due to an infinite sea of metallic electrons. Assuming that the antibonding states are always above the *d* states, the energy of the *d* states (the center of the *d* states) relative to the Fermi level can be a good indicator of the bond strength. The higher the position of the *d*-band center relative to the Fermi level, the more vacant the antibonding states, which leads to a stronger bond [8].

It corroborates the trends in catalytic activity from one transition metal to the next, and variation in reactivity by alloying, structure, strain, defects, and so forth. A large number of theoretical and experimental results have been accounted for in this way (22–36). An example of experimental results explained by the *d*-band model is included in Fig. 1-6.

The catalytic reactions are dependent on the electronic structure of transition metal and the reaction mechanisms. Most effective catalyst for oxygen-reduction reaction is Pt or Pt-based catalysts. Oxygen binds well on Pt surface with orbital mixing of oxygen and Pt surface atom [9], which can be explained with the intermediate state of oxygen reduction process, and the oxygen reduction reaction occurs in the different reaction path. During this orbital mixing, electron densities of the Pt-O bond are increased, and electron densities of O-O double bond are decreased. This indicates that oxygen molecule are dissociated. Each dissociated oxygen atom forms water with neighboring protons. Then, the water molecules are detached from Pt surface, and diffuse into electrolyte. Typically, oxygen reduction on Pt has an efficient pathway with the dissociation of oxygen double bond which corresponds to the 4-electron direct pathway [10].

On the other hand, oxygen does not bind well on Au surface with an inactive orbital mixing. The different electronic structure and interaction lead to different intermediate states, and thereby ORR on Au undergoes different reaction path from that of Pt. In this orbital mixing, electron densities of the Au-O bond are slightly increased, and electron densities of O-O double bond are insignificantly decreased compared to those of Pt. Therefore, oxygen molecules are not dissociated and form a hydrogen peroxide ( $\text{H}_2\text{O}_2$ )

as a product in acidic solution [11], which corresponds to the 2-electron path with a half of efficiency compared with the complete reduction path. It is reported that 4-electron serial path can occur through several intermediate states in the alkaline environment [12].

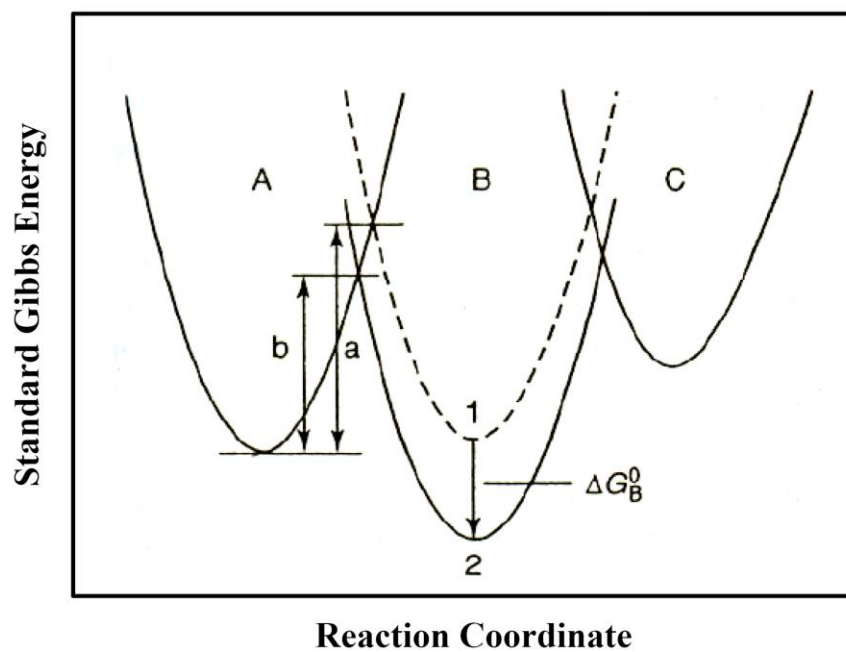


Fig. 1-3. Schematic representation of the Gibbs energy curves for the reaction  $A + e \rightarrow B \rightarrow C$ . It is a non-spontaneous reaction that requires an input of energy. Intermediate  $B$  is adsorbed on the catalyst surface and energy state changes from state (1) to state (2). The activation barriers for two situations are indicated as (a) and (b), respectively. From reference [6].

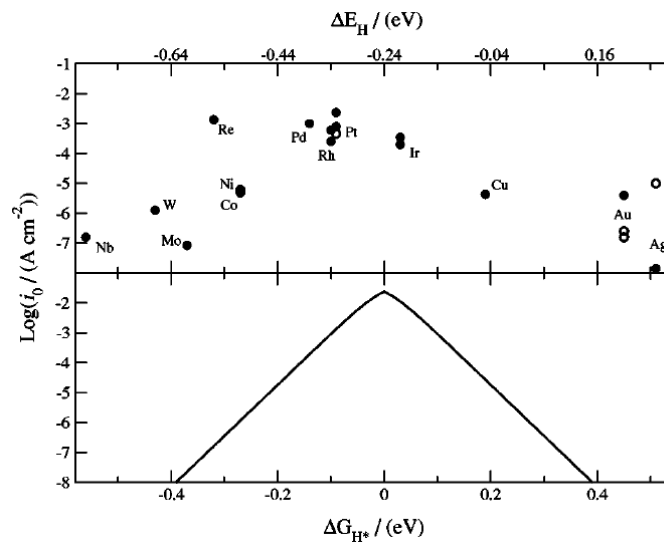


Fig. 1-4. (Top) Exchange current densities for hydrogen evolution reaction on various metal surface as a function of the hydrogen chemisorption energy per atom,  $\Delta E_H$ , (Bottom) volcano type activity as a function of the free energy for hydrogen adsorption,  $\Delta G_{H^*}$ . From reference [7].

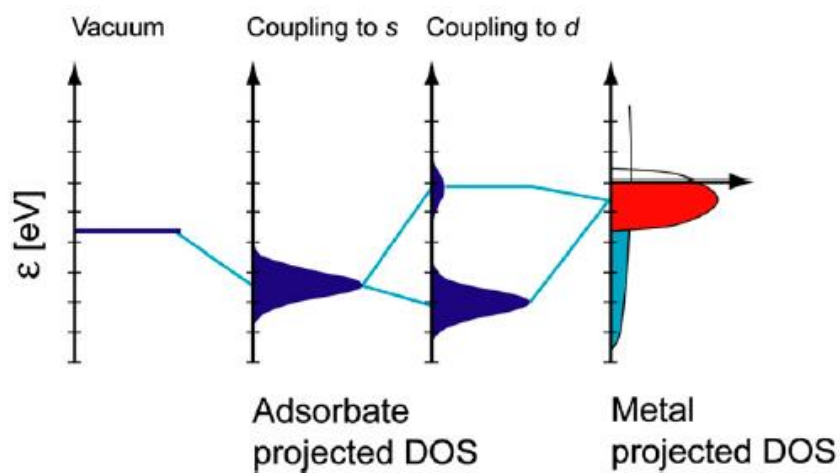


Fig. 1-5. (Color) Bond formation at a transition-metal surface. Schematic illustration of the formation of a chemical bond between an adsorbate valence level and the *s* and *d* states of a transition-metal surface. The bond is characterized by the degree to which the antibonding state between the adsorbate state and the metal *d* state is occupied. From reference [8].

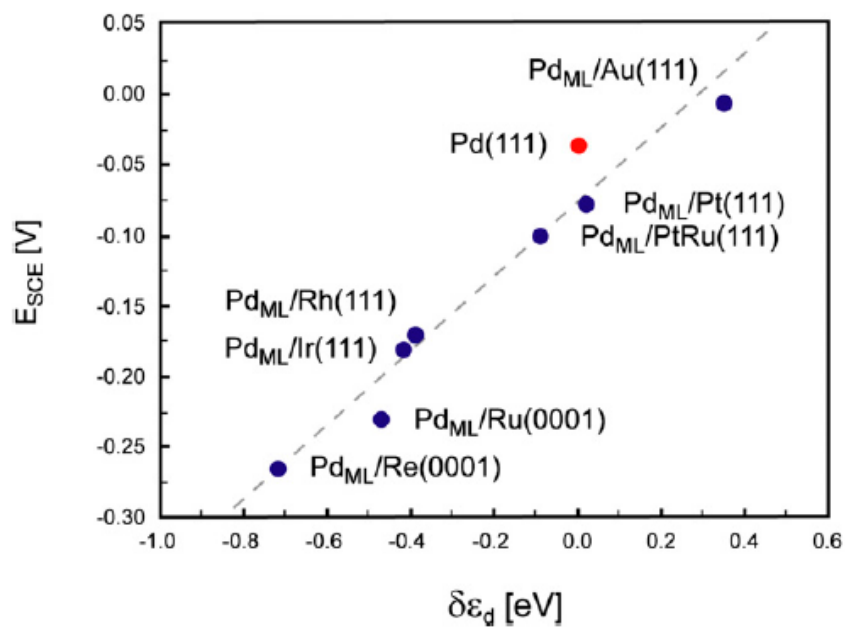
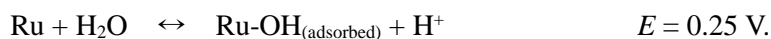


Fig. 1-6. Illustration of the use of the  $d$ -band model. Electrochemically measured changes in the hydrogen adsorption energy ( $E_{SCE}$ ) for Pd overlayers on various metals. It scales well with the calculated shift of the  $d$ -band center ( $\delta\epsilon_d$ ). From reference [8].

### 1.3. Modification of Catalytic Activity

Considering the chemisorption phenomena, orbital of reactant molecules and electronic structure of catalyst surface interact each other, and form a chemical bonding on catalyst surface. Chemical adsorption is favored when lattice of catalyst and atomic distance of reactant molecule are matched, which is called geometric effect. As mentioned above, suitable electron transfer between orbital of reactant molecules and electronic density of catalyst surface leads to chemical adsorption and catalytic activity, which is called electronic effect. In addition, the combination of two different catalysts where one is an active catalyst and another is a co-catalyst produces synergetic effects, so-called bifunctional effect. Generally, electronic effect is considered to be more weighty factor than others affecting the nature of catalytic phenomena. Therefore, employing bifunctional effect is regarded as a useful and powerful way for the catalyst design.

Methanol is oxidized on Pt with detaching hydrogen from CH<sub>3</sub>OH and producing CO<sub>2</sub> gas, as the anodic reaction of DMFC. However, when an intermediate state, the CO chemisorbed on Pt, is stabilized, methanol oxidation reaction does not proceed further [13]. This phenomenon is called CO poisoning, and blocks the active sites of Pt surface for methanol oxidation reaction. Pt catalyst can be modified by alloying with Ru. In this alloy catalyst, Pt sites are active for methanol but remain intermediate species (Pt-CO), and the Ru sites are active for water, forming a hydroxyl group on Ru (Ru-OH) [14]. The surface hydroxyl formation prefers to occur on Ru sites in the potential range of DMFC (0.3 V – 0.5 V vs. RHE) as follows [15]:



Then, the OH species on Ru interacts with CO on Pt leaving an oxygen atom, accelerating oxidation of CO to CO<sub>2</sub>. This mechanism is based on bifunctional effect as mentioned above. Electronic factor also contributes to cleavage of C-O bond, since the adjacent Ru atoms affect in Pt electronic structure as a ligand effect [16]. The geometric factor may also enhance the rate of reaction or not.

Along with the alloying, fabrication of composite catalysts by mixing the transition metal catalysts with metal oxides or phosphates is also effective way of catalyst design. Au catalysts are enhanced for oxygen reduction through combination of several oxide materials, such as defective MgO [17] and non-stoichiometric SnO<sub>x</sub> [11]. In this field of research, adjacent anodic defects of oxide material affect Au catalyst with concurrent transfer of electron density, as shown in Fig. 1-7. The movement of electron density represents the modification in the electronic structure of Au, and thereby catalytic activity of Au is modified, which is an example of electronic effect on catalyst.

Generally, fuel cells operate in the severe acidic or alkaline condition for a ion conductivity through the electrolyte or membrane. Since the acidic or alkaline stability is mandatory for the applicable materials in fuel cells, selection of materials is quite limited. Electrochemical performance of fuel cells is susceptible to humidity, thus hydrophilic nature of the combined materials is favored. The nano-sized catalytic designs provide a high active surface area and large current density, so the combination of catalytic materials

and porous materials are favorable to obtain the high active surface area.

Metal phosphate nearly satisfies the above demands as the support material for controlling the catalytic activity. It has a stability in the acidic and alkaline solutions, hydrous formation property [18], open framework structure [19,20], as shown in Fig. 1-8. Also, hydrous phosphates show high proton conductivity by hydrophilic domains in the presence of adsorbed water. Open framework structure of metal phosphate allows the access and release of reactant and product, forming a channel for proton, hydroxyl ions, and fuels.

Catalytic property of Pt is modified using the nanocomposite geometry with the defective iron phosphate, and correlated with electronic structure of Pt surface in the Chap. 2. In similar way, enhancement of Au activity is investigated using the cerium phosphate, as can be seen in the Appendix 1. Minimizing the limiting factors stated above, large interfacial area and a significant amount of electronic interactions between the Au and the defective cerium phosphate are achieved. Moreover, the own activity of cerium phosphate for hydrogen peroxide is identified, accomplishing synergetic effect with Au.

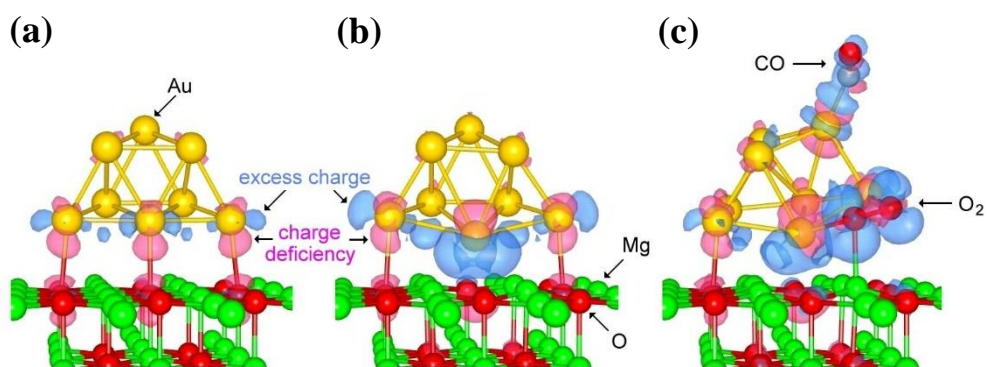


Fig. 1-7. (Color) Charge difference for (a) a gold cluster on a perfect MgO surface, (b) a gold cluster on an oxygen deficient MgO surface, and (c) with adsorbed reactants. From reference [17].

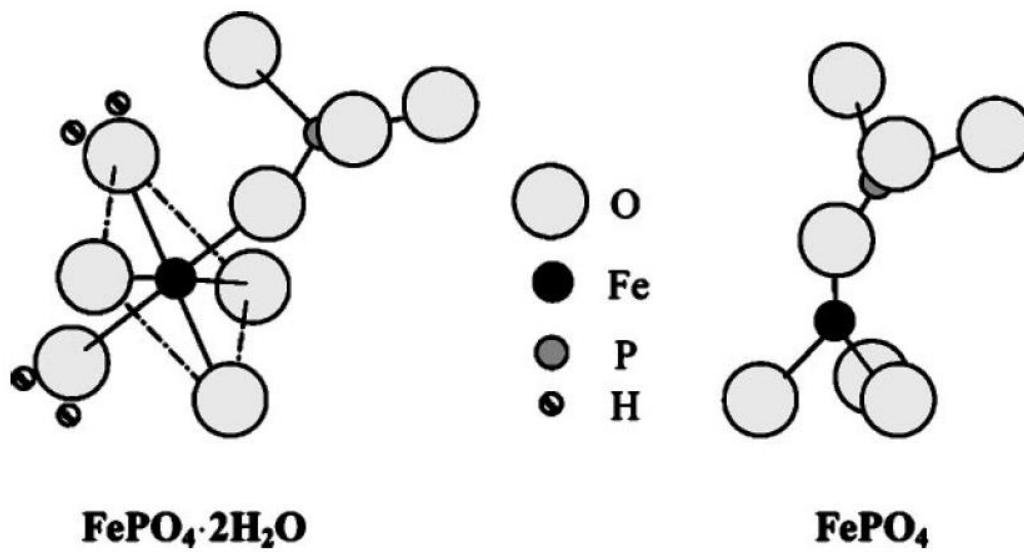


Fig. 1-8. Scheme of the formation of hydrous iron phosphates with respect to anhydrous phase: the variscite orthorhombic (*Pbca*) FePO<sub>4</sub>·2H<sub>2</sub>O and tridymite triclinic (*P1*) FePO<sub>4</sub>. From reference [18].

#### 1.4. Introduction to Li-Air Batteries

Recently, there is huge demand for energy storage technologies, and CO<sub>2</sub> emissions by fossil fuels are leading to the greenhouse effect and global warming which will be enormous threat for human survival in near future. Therefore, the acquisition of eco-friendly energy storage system will be more important in the future. On this circumstance, electric vehicles (EVs) or hybrid electric vehicles (HEVs) powered by rechargeable batteries are of tremendous interest. Among the viable technologies, lithium ion batteries has successfully played an important role in replacing the internal combustion engines, and their contribution will still be significant in years to come.

However, specific energy of Li-ion batteries (~200 Wh kg<sup>-1</sup> considering current collectors, cell packaging and system overheads) is limiting the driving range of electric vehicles below 500 km, which can be significantly increased by higher-energy density systems such as Li-S or Li-air batteries [21]. Li-air batteries are based on the reaction between Li ions and oxygen derived from air, and has theoretical specific energy of 3,500 Wh kg<sup>-1</sup>. Although its practical energy storage are not defined yet, the values are estimated to be in the range 500 to 1,000 Wh kg<sup>-1</sup>, which is enough to achieve the driving range of 500 km by electric vehicles [22].

The progress of Li-air batteries have been made in different systems, depending on the electrolytes employed, and are classified by type of electrolytes such as aqueous, non-aqueous, hybrid, and solid state electrolytes. Among them, non-aqueous (aprotic) Li-air batteries are relatively similar to Li-ion batteries and simple, thus have extensively been studied than any other systems [23]. Therefore, in this chapter, I intend to focus on aprotic Li-air batteries of which schematic structure and reaction mechanisms are represented in Fig. 1-9.

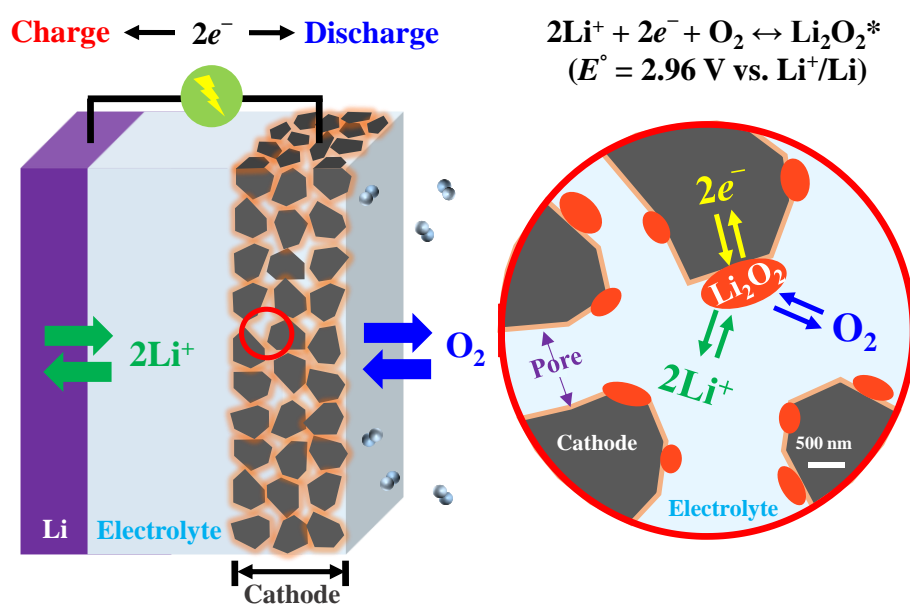


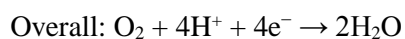
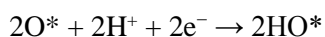
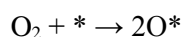
Fig. 1-9. (Color) Schematic representation of non-aqueous Li-air battery system.

## 1.5. Heterogeneous Catalysis in Li-Air Batteries

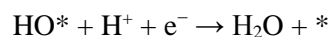
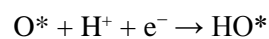
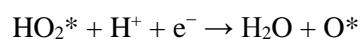
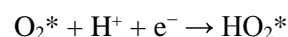
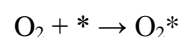
In Li-air batteries, considerable efforts have been made to control the heterogeneous electrocatalysts (similar to those of fuel cells) and to reduce overpotentials of both the oxygen reduction on discharge and oxygen evolution reaction on charge. However, the ORR mechanisms in aprotic Li-air batteries are far different from fuel cells in terms of reaction kinetics and products, and hence the role of the electrocatalyst is quite different. The reactions in aprotic Li-air batteries and fuel cells occurs with different steps and path, as follows [24,25]:

### ORR in aqueous electrolyte of fuel cells

Dissociation Mechanism:



Association mechanism:



### ORR in aprotic Li-air batteries



The ORR in fuel cells are described for the acidic environment and \* refers the adsorption site of catalysts or electrodes. As shown in the equations, ORR in aqueous electrolyte includes the breaking of oxygen double bond, leading to large overpotentials to complete the whole reactions. In contrast, ORR in aprotic Li-air batteries does not have the steps for breaking the oxygen bond, and occurs by direct route to form superoxide anion or lithium superoxide ( $\text{LiO}_2$ ), with subsequent production of lithium peroxide ( $\text{Li}_2\text{O}_2$ ) in solid phase. Different from the liquid water produced from ORR in fuel cells, this insulating solid  $\text{Li}_2\text{O}_2$  is deposited on the electrode surface, and has a significant influence on electrochemical properties.

When  $\text{Li}_2\text{O}_2$  forms in a film on the electrode surface, the influence of a solid electrocatalyst on the electrode would be less significant once the first monolayer is formed at the surface. Viswanathan *et al.* showed that electrochemical formation and decomposition of  $\text{Li}_2\text{O}_2$  films in initial stage are not that sluggish as in ORR/OER in fuel cells [26]. They used cyclic voltammetry and Tafel plots to define the kinetic overpotentials for discharge/charge reactions, and compared with first-principles theoretical prediction. From these results, the fundamental kinetic overpotentials were measured as being smaller than 0.2 V for both ORR/OER, and this value are nearly 1/3 of that for ORR/OER in aqueous media.

Furthermore, when using efficient electrocatalysts for aqueous ORR, parasitic electrolyte decomposition has been observed as opposed to the desired catalytic reactions. For instance, Pt, the most prominent catalyst for aqueous ORR, was observed to severely accelerate these side reactions, promoting electrolyte decomposition at relatively low

voltage ( $\sim 3.5$  V vs. Li/Li<sup>+</sup>) [27]. Therefore, in Li-air batteries, reducing overall cell impedance is more important to minimize overpotentials than enhancing catalytic activity of electrocatalyst for ORR and OER.

### 1.6. Issues in Air-cathodes for Li-Air Batteries

To bring the Li-air technology to the market, comprehensive study including Li metal anode, electrolyte, and cathode should be conducted, and the individual component of a Li-air battery still has many issues to be resolved. Therefore, in this thesis, the current progress and problems of air-cathodes are briefly introduced with suggestion of appropriate solutions.

Carbon-based materials have been ubiquitously employed as basic matrix for discharge/charge reactions to realize the high theoretical energy density of Li-air batteries. However, prolonged studies revealed that carbon is unstable in contact with the discharge products under high voltage, and is likely to decompose into lithium carbonate (Li<sub>2</sub>CO<sub>3</sub>).

McCloskey *et al.* observed that discharge product, Li<sub>2</sub>O<sub>2</sub> reacts chemically with a carbonaceous cathode during discharge forming a thin Li<sub>2</sub>CO<sub>3</sub> film, using isotopically labeled differential electrochemical mass spectrometry (DEMS) and XPS. Also, they confirmed that approximately the same amount of carbonate is formed by reaction of Li<sub>2</sub>O<sub>2</sub> with the ether electrolyte during charge [28]. Based on the theoretical charge-transfer model, they suggested that the carbonate layer at the carbon electrode/Li<sub>2</sub>O<sub>2</sub> interface causes a 10-100 fold decrease in current density.

Thotiyl *et al.* also investigated the stability of carbon electrodes and electrolyte in

Li-air batteries using in situ DEMS and FTIR [29]. They demonstrated that some decomposition of hydrophilic carbon, and no decomposition of hydrophobic carbon occurs during discharge. From their results, the main side reactions on discharge is electrolyte decomposition that forms mainly  $\text{Li}_2\text{CO}_3$ . Charging up to  $\sim 4$  V gives rise to decomposition of  $\text{Li}_2\text{CO}_3$  to  $\text{CO}_2$ , and interestingly, more  $\text{Li}_2\text{CO}_3$  is formed by electrolyte decomposition. The carbon electrode also decomposes into  $\text{Li}_2\text{CO}_3$  on charge under high voltage. As a results, the rate of  $\text{Li}_2\text{CO}_3$  formation from electrolyte and electrode exceeds the rate of  $\text{Li}_2\text{CO}_3$  decomposition, which lead to electrode passivation and large polarization. They concluded that interplay between the electrode and the electrolyte aggravate the cell stability than each in isolation. Schematic figure for this mechanism is represented in Fig. 1-10. Binder degradation was also reported by several reports, where the decomposition of electrolyte leads to degradation of binders, forming insulating LiF layers [30,31]. All of these produce insulating layers on the surface of air-cathodes during discharge/charge reactions, which results in poor cyclability of Li-air batteries. Also, the apparently-large overpotential during charge process is attributed to the side products formed on interface between  $\text{Li}_2\text{O}_2$  film and electrode surface rather than to the  $\text{Li}_2\text{O}_2$  oxidation kinetics.

Electrode clogging is also a crucial problem. Since  $\text{Li}_2\text{O}_2$  particles are continuously accumulated on the pores of an air electrode during discharge, it can potentially clog the electrode, preventing further reactions. Side products, e.g.  $\text{Li}_2\text{CO}_3$  which is hardly removable on charge, can also clog the pores in electrode, resulting in poor cyclability. Lim *et al.* observed the pore clogging in randomly aligned CNT powders by

SEM after discharge (Fig. 1-11), and that electrode operated only few cycles [32]. Therefore, electrode should be designed in a way that minimizes side reactions and electrode clogging.

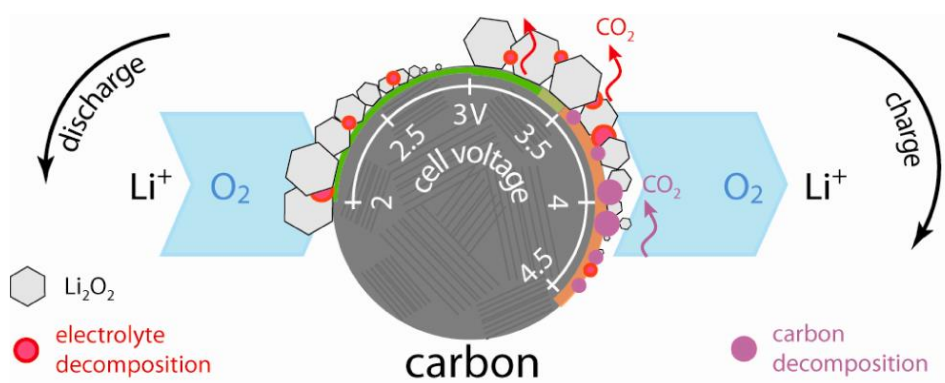


Fig. 1-10. (Color) Schematic representation of degradation mechanism in carbon electrodes. Carbon is relatively stable below 3.5 V (vs.  $\text{Li}/\text{Li}^+$ ), but is unstable on charging above 3.5 V (in the presence of  $\text{Li}_2\text{O}_2$ ). Electrolyte decomposition occurs during discharge/charge and is promoted on carbon. From reference [29].

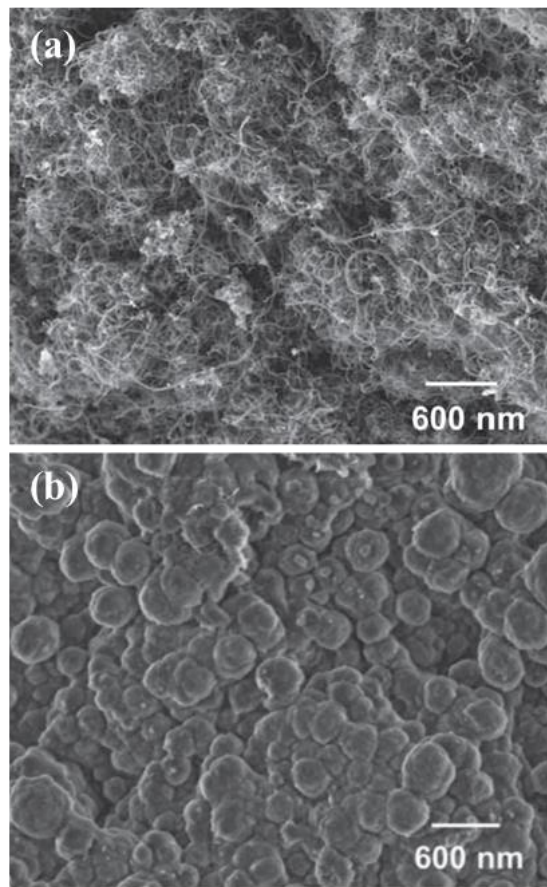


Fig. 1-11. SEM images of CNT powders of: (a) as-prepared, and (b) after the first discharge. From reference [32].

### 1.7. Design Strategy for High-Performance Air-Cathodes

As mentioned earlier, the side reactions between discharge product ( $\text{Li}_2\text{O}_2$ ) and electrolyte are quite notable on carbon electrodes. Therefore, there have been a lot of attempts to design a stable electrode by minimizing the surface area of carbon electrode. Although coating a semiconductor or metal on carbon can be a solution to suppress the surface exposure of carbon to discharge products or electrolytes, uniform and thin coating requires advanced technique and high cost. Instead, applying a conductive material not incorporating carbon additives is much easier as long as proper material is identified, and the possibility of carbon exposure is also restricted. For the carbon-free electrodes, high-weight materials must be excluded since it will destroy a key advantage of Li-air batteries, high specific energy. Also, the electrode should have large surface area or space for the discharge/charge reactions. Therefore, designing a suitable material with ideal architecture is very important to achieve high theoretical energy density of Li-air batteries.

Zhou's group used indium tin oxide (ITO) [33] and Sb-doped tin oxide (STO) [34] as conductive substrate for Ru nano-catalysts and showed good cyclability. Also, Li *et al.* synthesized hollow ruthenium dioxide ( $\text{RuO}_2$ ) and applied to Li-air battery as a carbon-free cathode [35]. Along with catalytic activity and the metallic conductivity of  $\text{RuO}_2$ , hierarchically porous hollow spheres can provide large surface area, leading to superior electrochemical performance. Above studies used Ru or  $\text{RuO}_2$  since they are known as a good catalyst for oxygen-evolution reaction (OER) for charge.

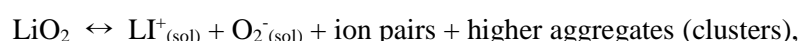
Titanium-based materials also have been studied due to their advantages, such as gravimetric energy density, cost, environmental benignity, and so forth, although they are

not known as efficient catalysts. Firstly, Bruce's group introduced titanium carbide (TiC) as a carbon-free cathode for Li-air batteries [36]. They showed that TiC-based cathode reduces remarkably side reactions compared with carbon, and exhibits reversible formation/decomposition of  $\text{Li}_2\text{O}_2$  during 100 cycles. They suggested that the combination of the electronic conductivity of TiC with the stability of the  $\text{TiO}_2$ -rich surface layer on TiC particles can be a reason for the stable and reversible discharge/charge.

Nazar's group also explored the titanium-based materials. They applied the Magneli phase ( $\text{Ti}_4\text{O}_7$ ) with a crystallite size between 10-20 nm to an air-cathode, and showed that this material significantly reduces the overpotential during charge compared to carbon [37]. Interestingly, they observed self-passivating substoichiometric  $\text{TiO}_{2-x}$  layers on  $\text{Ti}_4\text{O}_7$  surface, that sustain during discharge/charge by X-ray photoelectron spectroscopy (XPS). This surface  $\text{TiO}_{2-x}$  is also conductive, and can act as a substrate for electrochemical reactions. Suggested reaction mechanism is represented in Fig. 1-12 with galvanostatic discharge and charge profile. Therefore, they also studied the surface of titanium carbide to identify the role of surface chemistry on the electrochemical properties of titanium-based materials. Also, by using two different type of TiC (one with thin  $\text{TiO}_2$  layer below 2 nm and the other with thicker layer above 2 nm), they showed that insulating  $\text{TiO}_2$  surface layers on TiC, even as thin as 3 nm can completely inhibit the charge reaction ( $\text{Li}_2\text{O}_2$  oxidation) [38]. These series of studies highlight the role of passivation layer with proper thickness on the stability of Ti-based electrodes.

Along with the material investigations, electrode architecture is also important for the efficient accommodation/decomposition of discharge products. Recently, solvent

mediated growth of large  $\text{Li}_2\text{O}_2$  toroid has been reported by several papers, where the solubility of  $\text{LiO}_2$  plays a key role in its nucleation and growth stage (solution pathway/electrode pathway). The size of  $\text{Li}_2\text{O}_2$  particles, by the way, also significantly affected the discharge capacity and other electrochemical properties [39-41]. This  $\text{LiO}_2$  solubility is determined by change of gibbs free energy for the reaction [39]:



where the donor number of electrolyte significantly affects the stability of solvated form. The scheme representing two different reaction pathways and SEM image of large  $\text{Li}_2\text{O}_2$  toroid discharged in solution (DMSO electrolyte) are shown in Fig. 1-13.

To decompose the large  $\text{Li}_2\text{O}_2$  particles, redox mediator (RM) has emerged as an alternatives to the conventional solid catalyst. A redox mediator couple with suitable redox potential, denoted as  $\text{RM}^+/\text{RM}$ , dissolves in an aprotic electrolyte, and acts as a solution-phase catalyst. This soluble catalyst chemically decomposes the discharge product  $\text{Li}_2\text{O}_2$  at the interface between solid  $\text{Li}_2\text{O}_2$  and the liquid electrolyte (wet contact). This strategy is proven more effective than conventional solid catalysis with which the active site for the electrochemical interface is limited. The reaction mechanism of the soluble catalyst (redox mediator) is represented in Fig. 1-14.

Catalytic mechanism of the redox couple  $\text{RM}^+/\text{RM}$  is composed of two steps. Firstly, RM is electrochemically oxidized to  $\text{RM}^+$  on the cathode surface. Secondly,  $\text{RM}^+$  diffuses to the  $\text{Li}_2\text{O}_2$  surface, and chemically oxidizes  $\text{Li}_2\text{O}_2$ , releasing  $\text{Li}^+$ ,  $\text{O}_2$ , and reduced RM. Therefore, the charging voltage is reduced to the redox potential of  $\text{RM}^+/\text{RM}$ , which is usually lower than the voltage obtained from solid catalysts. This results in an

improvement in the round-trip efficiency as well as the cycle life. Therefore, combination of ideal architecture and soluble catalysts seems to be a most promising way to enhance the energy density and stability of air-cathode.

In this thesis, I would like to identify the electrode material having proper characteristics for air-cathode, and then design the architecture to be favorable for the diffusion of reaction molecules and redox mediator without clogging. Based on the understanding of catalytic reactions in Chap. 2 and Appendix 1, oxygen deficient  $\text{TiO}_{2-x}$  with ordered-porous architecture is suggested as a cathode for Li-air batteries in Chap. 3. By incorporating a soluble catalyst in this air-cathode, high energy density and stability of Li-air batteries are suitably achieved.

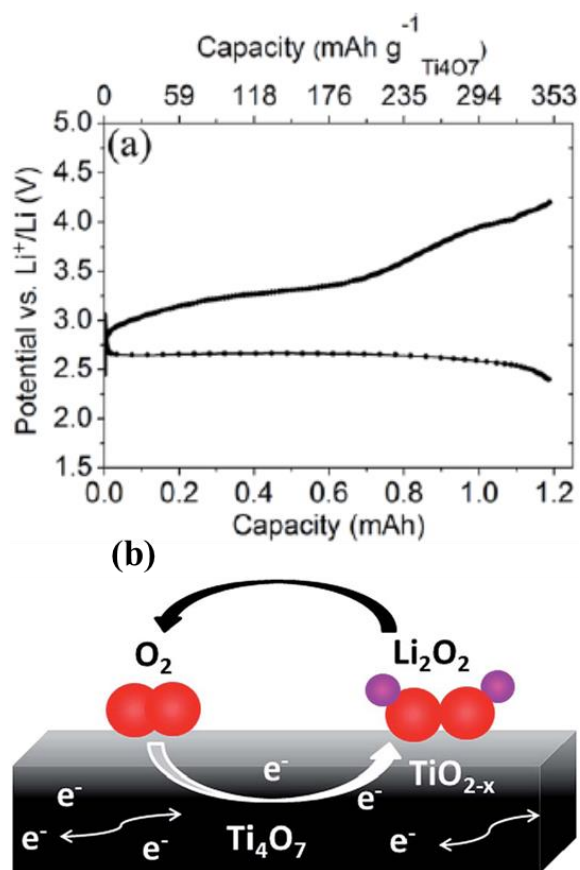


Fig. 1-12. (Color) (a) Galvanostatic discharge and charge profile of a Li-O<sub>2</sub> cell employing Ti<sub>4</sub>O<sub>7</sub> nanomaterial as cathode. (b) Scheme showing the gradual gradient of sub-stoichiometric TiO<sub>2-x</sub> formed at the surface of the Magneli Ti<sub>4</sub>O<sub>7</sub> cathode host in the Li-air cell that acts as a thin passivating interphase. From reference [37].

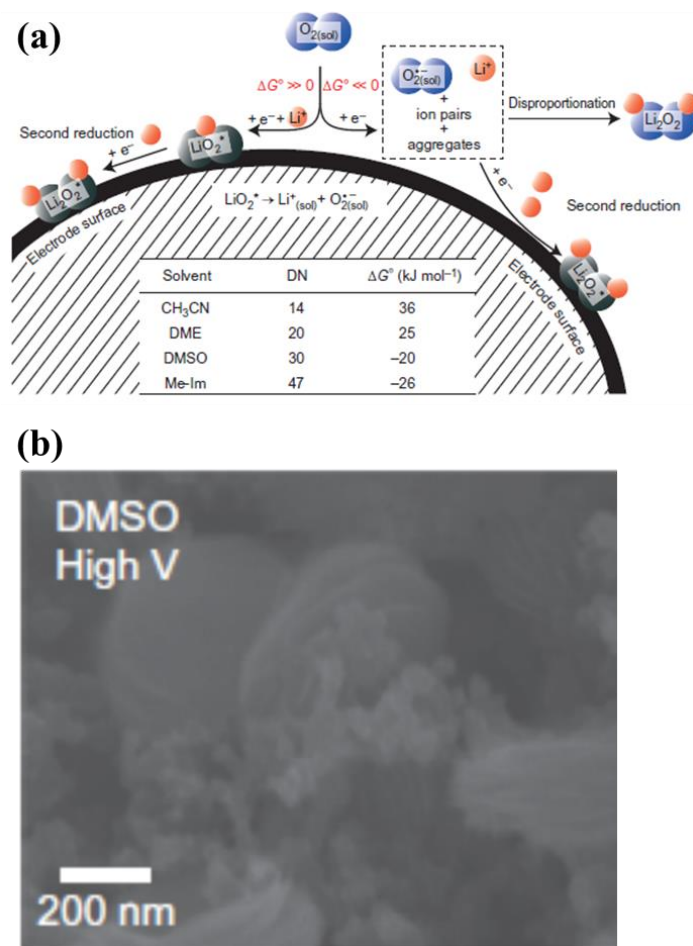


Fig. 1-13. (Color) (a) Schematic of the  $O_2$  reduction mechanism in an aprotic solvent containing  $Li^+$  showing the surface pathway and solution pathway. The table shows the donor number of various solvents. (b) SEM image showing the  $Li_2O_2$  morphology obtained in DMSO electrolyte. From reference [39].

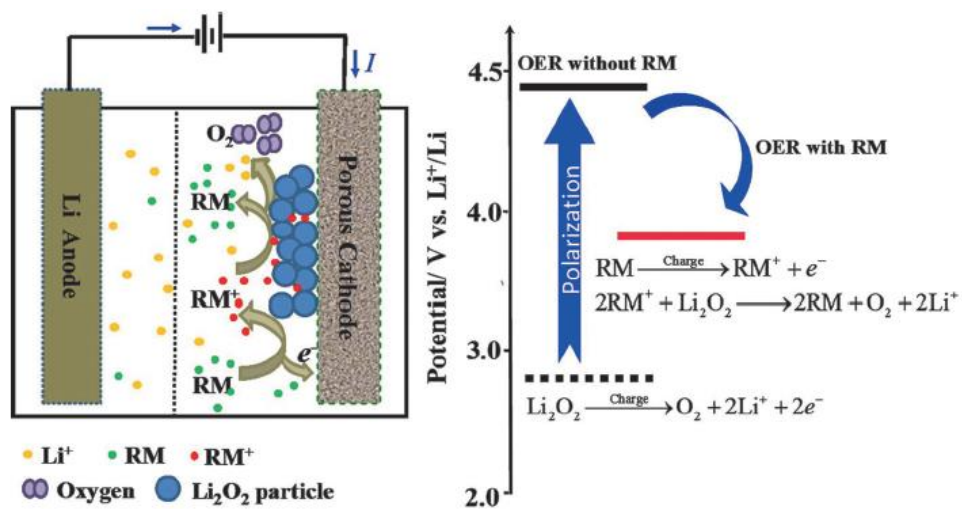


Fig. 1-14. (Color) Catalytic mechanism of the OER with a redox mediator as the soluble catalyst in an aprotic Li-O<sub>2</sub> battery. From reference [42].

## 1.8. References

1. R. V. Moorden, "Sulphur back in vogue for batteries," *Nature* **498**, 416 (2013).
2. J. M. J. Blomen and M. N. Mugerwa, *Fuel Cell Systems*, Plenum Press, 1993.
3. J. Larminie and A. Dicks, *Fuel Cell Systems Explained*, John Wiley & Sons, 2000.
4. A. Vaskelis, R. Tarozaitė, A. Jagminiene, L. T. Tamasiunaite, R. Juskenas, and M. Kurtinaitiene, "Gold Nanoparticles Obtained by Au(III) Reduction with Sn(II): Preparation and Electrocatalytic Properties in Oxidation of Reducing Agents," *Electrochimica Acta* **53**, 407 (2007).
5. L. Carrette, K. A. Friedrich, and U. Stimming, "Fuel Cells - Fundamentals and Applications," *Fuel Cells* **1**, 5 (2001).
6. W. Vielstich, A. Lamm, and H. A. Gasteiger, *Handbook of Fuel Cells - Fundamentals Technology and Applications*, John Wiley & Sons, 2003.
7. J. K. Norskov, T. Bligaard, A. Logadottir, J. R. Kitchin, J. G. Chen, S. Pandelov, and U. Stimming, "Trends in the Exchange Current for Hydrogen Evolution," *J. Electrochem. Soc.* **152**, J23 (2005).
8. J. K. Norskov, F. Abild-Pedersen, F. Studt, and T. Bligaard, "Density Functional Theory in Surface Chemistry and Catalysis," *P. Natl. Acad. Sci.* **108**, 937 (2011).
9. A. V. Walker, B. Klotzer, and D. A. King, "Dynamics and Kinetics of Oxygen Dissociative Adsorption on Pt{110}(1×2)," *J. Chem. Phys.* **109**, 6879 (1998).
10. S. Yotsuhashi, Y. Yamada, T. Kishi, W. A. Diño, H. Nakanishi and H. Kasai, "Dissociative Adsorption of O<sub>2</sub> on Pt and Au Surfaces: Potential-Energy Surfaces and Electronic States," *Phys. Rev. B* **77**, 115413 (2008).
11. W. S. Baker, J. J. Pietron, M. E. Teliska, P. J. Bouwman, D. E. Ramaker, and K. E. Swider-Lyons, "Enhanced Oxygen Reduction Activity in Acid by Tin-Oxide Supported Au Nanoparticle Catalysts," *J. Electrochem. Soc.* **153**, A1702 (2006).
12. S. Strbac and R. R. Adzic, "The Influence of OH<sup>-</sup> Chemisorption on the Catalytic Properties of Gold Single Crystal Surfaces for Oxygen Reduction in Alkaline

- Solutions,” *J. Electroanal. Chem.* **403**, 169 (1996).
13. J. Jiang and A. Kucernak, “Electrooxidation of Small Organic Molecules on Mesoporous on Precious Metal Catalysts I: CO and Methanol on Platinum,” *J. Electroanal. Chem.* **533**, 153 (2002).
  14. E. S. Steigerwalt, G. A. Deluga, D. E. Cliffel, and C. M. Lukehart, “A Pt-Ru/Graphitic Carbon Nanofiber Nanocomposite Exhibiting High Relative Performance as a Direct-Methanol Fuel Cell Anode Catalyst,” *J. Phys. Chem.* **105**, 8097 (2001).
  15. W. L. Holstein and H. D. Rosenfeld, “In-Situ X-ray Absorption Spectroscopy Study of Pt and Ru Chemistry during Methanol Electrooxidation,” *J. Phys. Chem. B* **109**, 2176 (2005).
  16. P. Liu and J.K.Nürskov, “Kinetics of the Anode Processes in PEM Fuel Cells - The Promoting Effect of Ru in PtRu Anodes,” *Fuel Cells* **1**, 192 (2001).
  17. B. Yoon, H. Häkkinen, U. Landman, A. S. Wörz, J.-M. Antonietti, S. Abbet, K. Judai, and U. Heiz, “Charging Effects on Bonding and Catalyzed Oxidation of CO on Au<sub>8</sub> Clusters on MgO,” *Science* **307**, 403 (2005).
  18. D. Son, E. Kim, T.-G. Kim, M. G. Kim, J. Cho, and B. Park, “Nanoparticle Iron-Phosphate Anode Material for Li-Ion Battery,” *Appl. Phys. Lett.* **85**, 5875 (2004).
  19. A. K. Cheetham, G. Férey, and T. Loiseau, “Open-Framework Inorganic Materials,” *Angew. Chem. Int. Ed.* **38**, 3268 (1999).
  20. W. Y. Ching and P. Rulis, “Large Differences in the Electronic Structure and Spectroscopic Properties of Three Phases of AlPO<sub>4</sub> from *Ab Initio* Calculations,” *Phys. Rev. B* **77**, 125116 (2008).
  21. P. G. Bruce, S. A. Freunberger, L. J. Hardwick, and J.-M. Tarascon, “Li-O<sub>2</sub> and Li-S Batteries with High Energy Storage.” *Nat. Energy.* **1**, 1 (2016).
  22. D. Aurbach, B. D. McCloskey, L. F. Nazar, and P. G. Bruce, “Advances in Understanding Mechanisms Underpinning Lithium-Air Batteries.” *Nat. Energy* **11**,

- 19 (2012).
23. F. Li, T. Zhang, and H. Zhou, "Challenges of Non-Aqueous Li-O<sub>2</sub> Batteries: Electrolytes, Catalysts, and Anodes." *Energy Environ. Sci.* **6**, 1125 (2013).
  24. J. K. Nørskov, J. Rossmeisl, A. Logadottir, and L. Lindqvist, "Origin of the Overpotential for Oxygen Reduction at a Fuel-Cell Cathode." *J. Phys. Chem. B* **108**, 17886 (2004).
  25. B. D. McCloskey, R. Scheffler, A. Speidel, G. Girishkumar, and A. C. Luntz, "On the Mechanism of Nonaqueous Li-O<sub>2</sub> Electrochemistry on C and Its Kinetic Overpotentials: Some Implications for Li-Air Batteries." *J. Phys. Chem. C* **116**, 23897 (2012).
  26. V. Viswanathan, J. K. Nørskov, A. Speidel, R. Scheffler, S. Gowda, and A. C. Luntz, "Li-O<sub>2</sub> Kinetic Overpotentials: Tafel Plots from Experiment and First-Principles Theory." *J. Phys. Chem. Lett.* **4**, 556 (2013).
  27. B. D. McCloskey, R. Scheffler, A. Speidel, D. S. Bethune, R. M. Shelby, and A. C. Luntz, "On the Efficacy of Electrocatalysis in Nonaqueous Li-O<sub>2</sub> Batteries." *J. Am. Chem. Soc.* **133**, 18038 (2011).
  28. B. D. McCloskey, A. Speidel, R. Scheffler, D. C. Miller, V. Viswanathan, J. S. Hummelshøj, J. K. Nørskov, and A. C. Luntz, "Twin Problems of Interfacial Carbonate Formation in Nonaqueous Li-O<sub>2</sub> Batteries." *J. Phys. Chem. Lett.* **3**, 997 (2012).
  29. M. M. O. Thotiyl, S. A. Freunberger, Z. Peng, and P. G. Bruce, "The Carbon Electrode in Nonaqueous Li-O<sub>2</sub> Cells." *J. Am. Chem. Soc.* **135**, 494 (2012).
  30. R. Black, S. H. Oh, J.-H. Lee, T. Yim, B. Adams, and L. F. Nazar, "Screening for Superoxide Reactivity in Li-O<sub>2</sub> Batteries: Effect on Li<sub>2</sub>O<sub>2</sub>/LiOH Crystallization." *J. Am. Chem. Soc.* **134**, 2902 (2012).
  31. R. Younesi, M. Hahlin, F. Björefors, P. Johansson, and K. Edström, "Li-O<sub>2</sub> Battery Degradation by Lithium Peroxide (Li<sub>2</sub>O<sub>2</sub>): A Model Study." *Chem. Mater.* **25**, 77 (2012).

32. H.-D. Lim, K.-Y. Park, H. Song, E. Y. Jang, H. Gwon, J. Kim, Y. H. Kim, M. D. Lima, R. O. Robles, X. Lepro, R. H. Baughman, and K. Kang, "Enhanced Power and Rechargeability of a Li-O<sub>2</sub> Battery Based on a Hierarchical-Fibril CNT Electrode." *Adv. Mater.* **25**, 1348 (2013).
33. F. Li, D.-M. Tang, Y. Chen, D. Golberg, H. Kitaura, T. Zhang, A. Yamada, H. Zhou, "Ru/ITO: A Carbon-Free Cathode for Nonaqueous Li-O<sub>2</sub> Battery." *Nano Lett.* **13**, 4702 (2013).
34. F. Li, D.-M. Tang, Z. Jian, D. Liu, D. Golberg, A. Yamada, and H. Zhou, "Li-O<sub>2</sub> Battery Based on Highly Efficient Sb-Doped Tin Oxide Supported Ru Nanoparticles." *Adv. Mater.* **26**, 4659 (2014).
35. F. Li, D.-M. Tang, T. Zhang, K. Liao, P. He, D. Golberg, A. Yamada, and H. Zhou, "Superior Performance of a Li-O<sub>2</sub> Battery with Metallic RuO<sub>2</sub> Hollow Spheres as the Carbon-Free Cathode." *Adv. Energy Mater.* **5**, 1500294 (2015).
36. M. M. O. Thotiyl, S. A. Freunberger, Z. Peng, Y. Chen, Z. Liu, and P. G. Bruce, "A Stable Cathode for the Aprotic Li-O<sub>2</sub> Battery." *Nat. Mater.* **12**, 1050 (2013).
37. D. Kundu, R. Black, E. J. Berg, and L. F. Nazar, "A Highly Active Nanostructured Metallic Oxide Cathode for Aprotic Li-O<sub>2</sub> Batteries." *Energy Environ. Sci.* **8**, 1292 (2015).
38. B. D. Adams, R. Black, C. Radtke, Z. Williams, B. L. Mehdi, N. D. Browning, and L. F. Nazar, "The Importance of Nanometric Passivating Films on Cathodes for Li-Air Batteries." *ACS Nano.* **8**, 12 (2014).
39. L. Johnson, C. Li, Z. Liu, Y. Chen, S. A. Freunberger, P. C. Ashok, B. B. Praveen, K. Dholakia, J.-M. Tarascon, and P. G. Bruce, "The Role of LiO<sub>2</sub> Solubility in O<sub>2</sub> Reduction in Aprotic Solvents and Its Consequences for Li-O<sub>2</sub> Batteries." *Nat. Chem.* **6**, 1091 (2014).
40. N. B. Aetukuri, B. D. McCloskey, J. M. Garcia, L. E. Krupp, V. Viswanathan, and A. C. Luntz, "Solvating Additives Drive Solution-Mediated Electrochemistry and Enhance Toroid Growth in Non-Aqueous Li-O<sub>2</sub> Batteries." *Nat. Chem.* **7**, 50 (2014).

41. X. Gao, Y. Chen, L. Johnson, and P. G. Bruce, "Promoting Solution Phase Discharge in Li-O<sub>2</sub> Batteries Containing Weakly Solvating Electrolyte Solutions." *Nat. Mater.* **15**, 882 (2016).
42. N. Feng, P. He, and H. Zhou, "Enabling Catalytic Oxidation of Li<sub>2</sub>O<sub>2</sub> at the Liquid-Solid Interface: The Evolution of an Aprotic Li-O<sub>2</sub> Battery." *ChemSusChem* **8**, 600 (2015).

## Chapter 2.

# Electronic Effect in Methanol Dehydrogenation on Pt Surface: Potential Control during Methanol Electrooxidation

### 2.1. Introduction

Fuel cells are promising alternative power-generation sources to conventional combustion-based ones, capable of environmentally-friendly energy conversion. Polymer electrolyte membrane fuel cells (PEMFCs) and direct-methanol fuel cells (DMFCs) are the key technologies of low-temperature cells for various applications such as electric vehicles, portable electronic devices, etc. [1-7].

Unfortunately, current state-of-the-art catalysts are mainly platinum-based, often too expensive for large-scale commercialization [8-13]. To overcome this barrier, researchers have tried to establish the fundamental rule governing the activity of catalysts. With progresses in density-functional theory (DFT) calculations, Nørskov and several co-workers proposed the *d*-band center relative to the Fermi-level, as a descriptor for the reactivity of a transition-metal surface [14-20]. According to this model, the bond strength is characterized by the filling of the antibonding states formed between adsorbate

---

\*The work presented in Chap. 2 was published in *J. Phys. Chem. Lett.* **4**, 2931 (2013) entitled, "Electronic Effect in Methanol Dehydrogenation on Pt Surface: Potential Control during Methanol Electrooxidation"

**Joonhyeon Kang**, Seunghoon Nam, Yuhong Oh, Hongsik Choi, Sungun Wi, Byungho Lee, Taehyun Hwang, Saeromi Hong, and Byungwoo Park\*

states and metal  $d$  states. Since this filling is given by the energy of the antibonding states relative to the Fermi-level, the position of the  $d$ -band center relative to Fermi-level is directly related to the adsorption energies and activation barriers in catalytic reactions. The higher the position of the  $d$ -band center relative to the Fermi-level, the more vacant the antibonding states, which leads to a stronger bond between the adsorbate and the metal surface [14,15,17,20]. Actually, this model has successfully represented various catalytic reactions, and based on experimentally measured values, many approaches have directly linked catalytic activity with the electronic structures of transition-metal surfaces [21-29].

However, in the case of methanol-oxidation reaction (MOR), the access to the pure electronic effect has been blocked due to many limitations such as the disturbance of the bifunctional mechanism [30-33], complex reaction paths [34-39], ensemble-site requirements [31,40-42], etc. These limitations originate from the intrinsic complexity of methanol-oxidation mechanisms. By conventional approaches, it is impossible to observe the electronic effect on the catalytic activity in methanol oxidation.

In this research, we introduce a new strategy for understanding catalytic reactions in terms of electronic structures. Generally, methanol-oxidation reaction on Pt can be described by three steps [30,34,38,43] when passing through the  $\text{CO}_{\text{ad}}$  intermediate:



Since the CO-oxidation processes (Eqs. (2) and (3)) are mainly governed by bifunctional effects, and not by the electronic structure when a second component is used

with Pt [44,45], these processes were separated by sensitive potential control. To focus on the methanol-dehydrogenation reaction (Eq. (1)), the voltage was held at 0.3 V (vs. reversible hydrogen electrode (RHE)) where methanol is decomposed to CO without any other reactions. Further reaction does not occur because Pt is unable to activate water (Eq. (2)), and CO<sub>2</sub> cannot be formed until ~0.45 V [41,46-48]. Also, in the potential range below 0.35 V, the reaction path can be simplified as a sole reaction pathway forming CO<sub>ad</sub> on the Pt surface without other possible routes that lead to the formation of soluble product species [34]. Therefore, we can successfully obtain the adsorbed CO as the final product, not as the reaction intermediate, in this case.

We also excluded the ensemble-site effect that hinders the investigation of electronic effect in an alloy system like PtRu, by using amorphous metal phosphate (FePO<sub>4</sub>) as the support material in the modification of the electronic structure according to the Fermi-energy difference [49]. In our previous researches, we have observed that core-level binding energies of Pt or Au nanoparticles vary with the nearby amorphous metal phosphate, and this material is also known as a suitable transfer medium for proton, hydroxyl ion, water, methanol, and oxygen [50-56].

Although Ru or other components are alloyed with Pt to enhance the CO-oxidation process [1,3,9,30-33,41], the methanol-dehydrogenation rate is still insufficient for the practical application of DMFCs. Therefore, optimum catalysts should be designed by optimizing each aspect: methanol dehydrogenation and CO oxidation. In this paper, our approach focuses on the methanol-dehydrogenation reaction that leads to the formation of CO<sub>ad</sub>, and the results are discussed in terms of *d*-band center model [14-17]. Other

reactive intermediates ( $\text{HCOO}^*$  or  $\text{HCHO}^*$ ) or soluble species are not significant in the potential range of interest [34]. This is the first experimental report on the direct correlation between dehydrogenation activity and the  $d$ -band center of a transition metal during methanol-oxidation reaction. Our novel finding for the electronic effect in CO production from methanol can furnish a valuable insight into the development of new catalyst for DMFC.

## 2.2. Experimental Section

Pt/FePO<sub>4</sub> nanocomposite electrodes were fabricated by rf magnetron co-sputtering on indium-tin oxide (ITO) glass using Pt and FePO<sub>4</sub> targets at room temperature (RT) by varying the sputtering rate of FePO<sub>4</sub> at a fixed power of Pt. Thin films were annealed at 300°C for 30 min to enhance their adhesion onto the ITO surface as well as to synthesize well-connected Pt nanocrystals in the amorphous FePO<sub>4</sub> matrix.

X-ray diffraction (XRD, New D8 Advance: Bruker) was used to characterize the crystal structures of Pt, Pt/FePO<sub>4</sub> and FePO<sub>4</sub>, and to determine the grain size of Pt in the nanocomposite. The electronic structure of the Pt valence-band was analyzed by x-ray photoelectron spectroscopy (XPS, AXIS-HSI: KRATOS) with 1253.84-eV incident photon. The Shirley background was subtracted from each measured spectrum, and the position of the *d*-band center was obtained from  $\int N(\varepsilon)\varepsilon d\varepsilon / \int N(\varepsilon) d\varepsilon$ , where  $N(\varepsilon)$  is the density of states or the XPS intensity after background correction [1-6].

The Pt/FePO<sub>4</sub> nanocomposite, Pt wire, and Hg/Hg<sub>2</sub>Cl<sub>2</sub> (SCE) as the working, counter, and reference electrodes, respectively, were used with a computer-controlled potentiostat (CHI 604A: CH Instrumental Inc.). All of the potentials in this article were converted to RHE. The cyclic voltammetry (CV) was carried out in a 0.1 M HClO<sub>4</sub> solution at a scan rate of 50 mV/s, to determine the available Pt sites by integrating the hydrogen adsorption/desorption curves and to confirm the surface orientation of Pt. For the CO-coverage measurement, a set of programmed potential steps, chronoamperometry, and fast-scan CV (Fig. 2-3) were performed in a 0.1 M CH<sub>3</sub>OH + 0.1 M HClO<sub>4</sub> solution. The potential steps for cleaning the Pt surfaces were attained by several 1.0 V (oxidation)

- 0.01 V (reduction) steps with 1-s holding time for each step. Time for chronoamperometry (methanol dehydrogenation) was varied in the range of 0.1 - 150 s to measure the amount of adsorbed CO at different reaction times. Fast CV was performed at a scan rate of 3 V/s to strip the CO<sub>ad</sub>. Each electrochemical measurement was carried out in a N<sub>2</sub>-purged solution at RT.

### 2.3. Results and Discussion

Pt nanoparticles having different positions of *d*-band center were prepared by varying the sputtering rate of FePO<sub>4</sub> with the sputtering rate of Pt fixed (co-sputtering). Before measuring the methanol-dehydrogenation activity, we first identified the crystal structure, grain size, and surface orientation of each sample. X-ray diffraction (Fig. 2-1) confirmed polycrystalline Pt phases embedded in the amorphous FePO<sub>4</sub>. From the Scherrer equation of  $\Delta k$  vs.  $k$  (the scattering vector  $k = (4\pi/\lambda)\sin\theta$ ), the grain size of Pt was in the range of 6.8 - 12.7 nm for the pure Pt and Pt/FePO<sub>4</sub> nanocomposites (Table 2-1). The size decreased with the increased sputtering power of FePO<sub>4</sub>. However, these are beyond the range where the catalytic activity is strongly sensitive to the Pt-nanoparticle size [57-64].

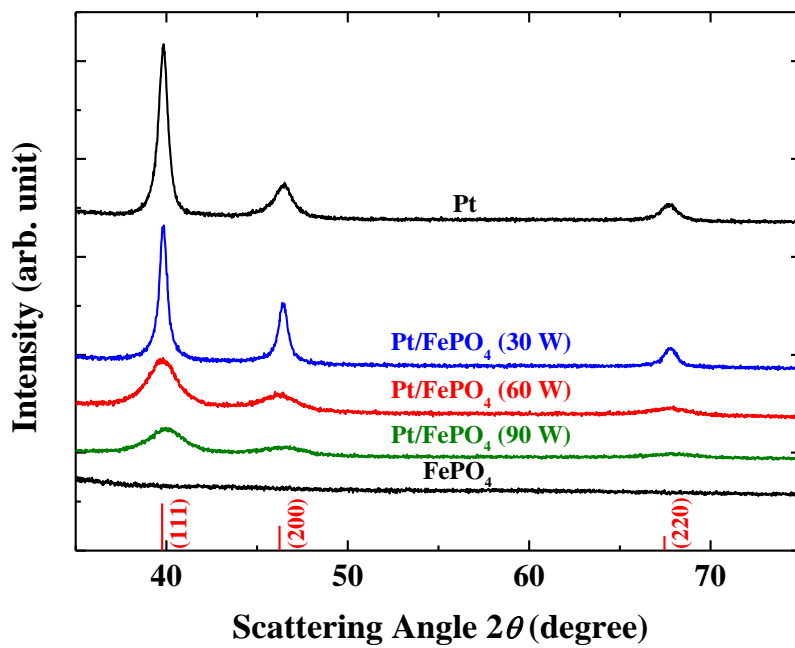


Fig. 2-1. (Color) X-ray diffraction of Pt and Pt/FePO<sub>4</sub> nanocomposites to determine the grain size of Pt nanocrystals from the  $\Delta k$  vs.  $k$  plot.

| Sample                      | Grain Size    |
|-----------------------------|---------------|
| Pt                          | 12.3 ± 1.7 nm |
| Pt/FePO <sub>4</sub> (30 W) | 12.7 ± 1.2 nm |
| Pt/FePO <sub>4</sub> (60 W) | 7.6 ± 0.4 nm  |
| Pt/FePO <sub>4</sub> (90 W) | 6.8 ± 0.4 nm  |

Table 2-1. (Color) Grain size of crystalline Pt at various sputtering powers of FePO<sub>4</sub>, obtained from the  $\Delta k$  vs.  $k$  plot of Fig. 2-1.

From the adsorption and desorption of hydrogen, we measured the active surface areas of Pt, and also confirmed no significant change in Pt orientation (Fig. 2-2). Furthermore, it was observed that the amorphous FePO<sub>4</sub> does not participate in the methanol-oxidation reaction (Fig. 2-3), only acting as an electronic-tuning component for Pt by the Fermi-energy difference.

To investigate the methanol-dehydrogenation activity, the coverage of adsorbed CO on Pt was measured from the methanol-dehydrogenation reaction (Eq. (1)). Wieckowski's group showed that the amount of CO<sub>ad</sub> formed from methanol decomposition can be measured without changing the electrolyte solution by combining chronoamperometry and fast-scan CV [34,46,65] under potential control (Fig. 2-4). This technique consists of three steps: cleaning, methanol dehydrogenation, and CO stripping. During the chronoamperometry step, methanol is decomposed into CO, which is strongly adsorbed on Pt until stripped through the fast-scan CV. This is possible because at a fast scan rate, Pt is insensitive to the presence of methanol in the solution, and only the adsorbed CO is stripped during the fast CV (Fig. 2-5).

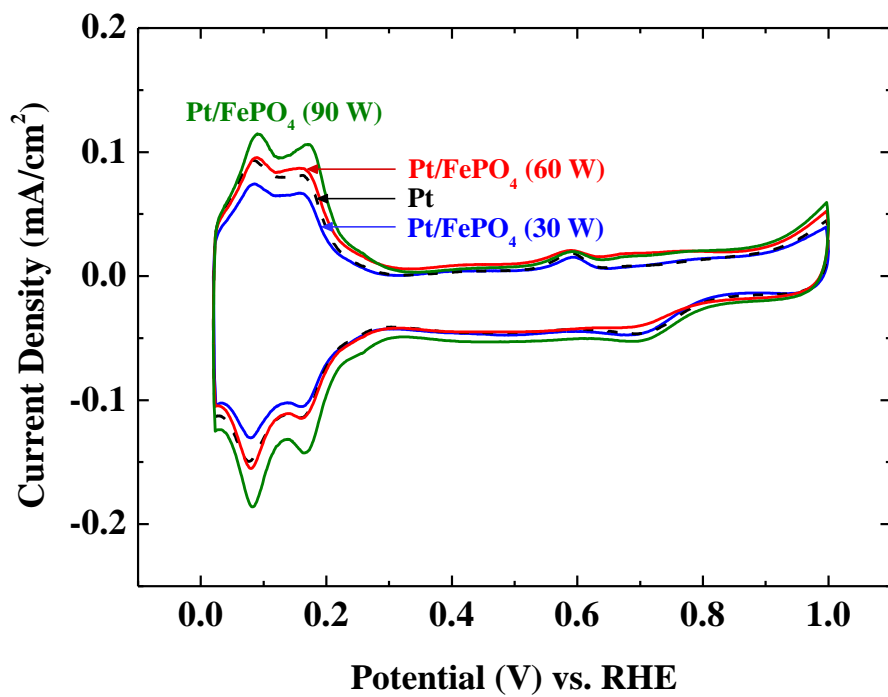


Fig. 2-2. (Color) Cyclic voltammograms of the Pt and Pt/FePO<sub>4</sub>-nanocomposite electrodes with various sputtering powers of FePO<sub>4</sub> in 0.1 M HClO<sub>4</sub>.

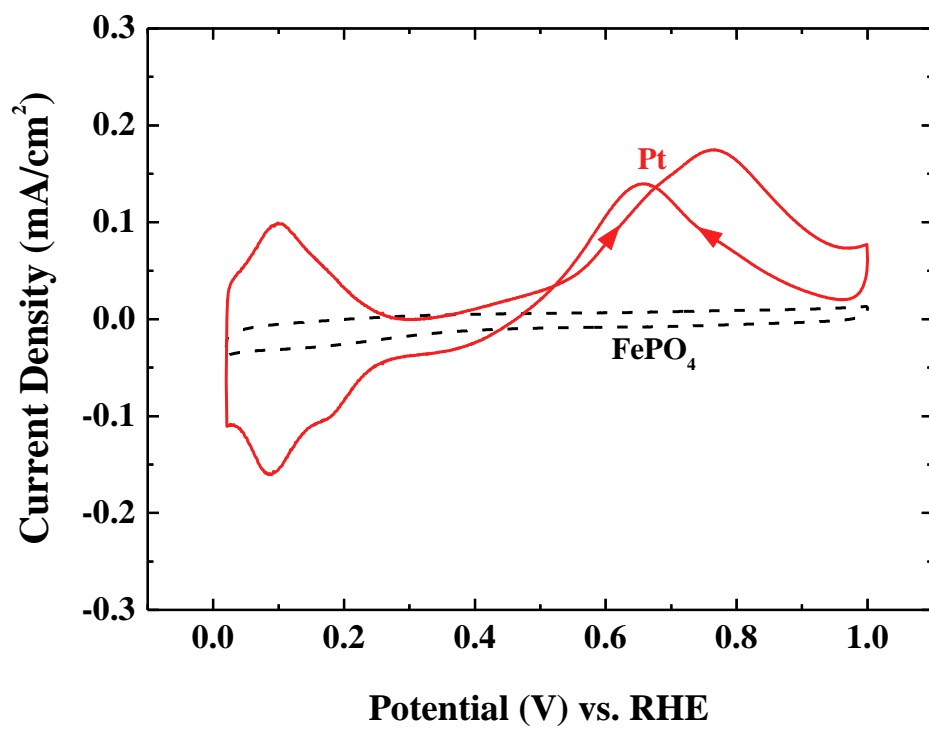


Fig. 2-3. (Color) Cyclic voltammograms of Pt and FePO<sub>4</sub> in 0.1 M HClO<sub>4</sub> + 0.1 M CH<sub>3</sub>OH at a scan rate of 50 mV/s.

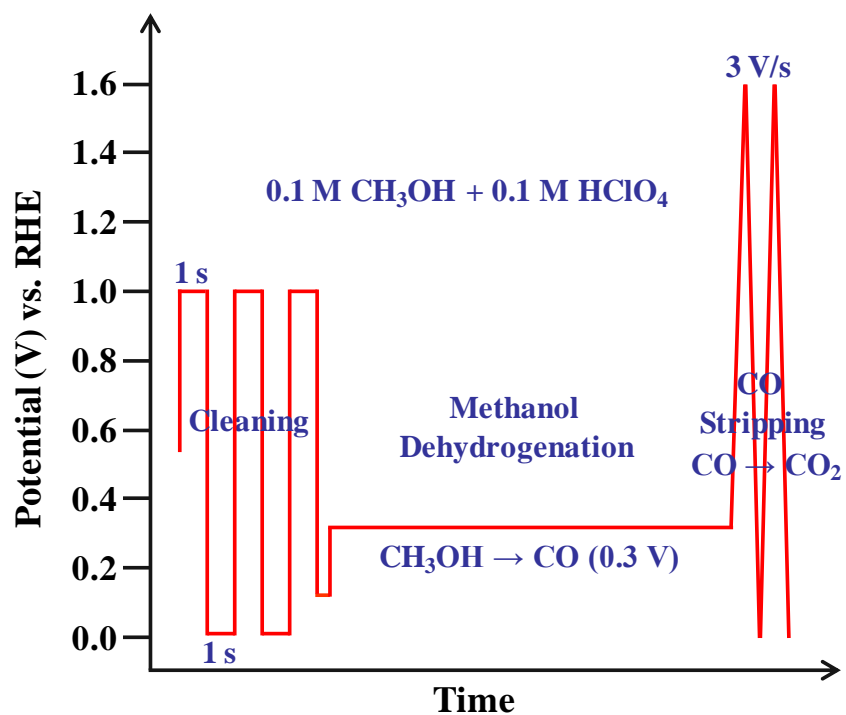


Fig. 2-4. (Color) Cyclic voltammograms including the available potential region of the Au-O chemisorption/desorption reaction. The Au and Au/AlPO<sub>4</sub> nanocomposite electrodes were examined in an oxygen-free (nitrogen-purged) 0.5 M H<sub>2</sub>SO<sub>4</sub> solution at a scan rate of 50 mV/s.

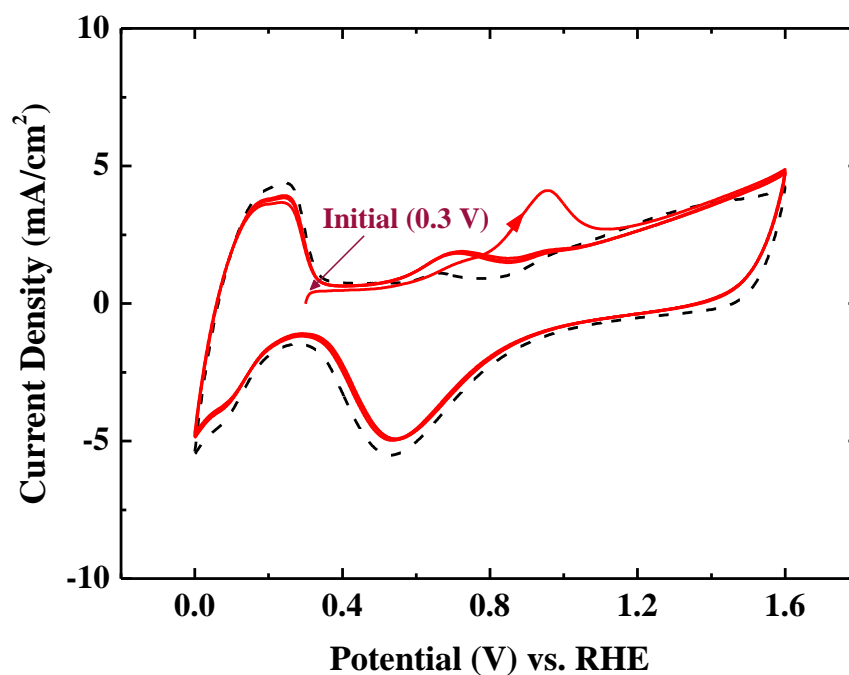


Fig. 2-5. (Color) Fast scan (3 V/s) cyclic voltammogram of Pt showing the  $\text{CO}_{\text{ad}}$  stripping peak (1st cycle) and subsequent 3 cycles (total 4 cycles), measured from potential control (Fig. 1) in 0.1 M  $\text{HClO}_4$  + 0.1 M  $\text{CH}_3\text{OH}$  (red solid line). The second and subsequent scans are almost identical, and also similar to the CV curve in 0.1 M  $\text{HClO}_4$  (dotted line) except for slight current around 0.7 V from methanol-decomposition process forming soluble species [46]. Thus, the second scan of CV was used as background to obtain the charge corresponding to the oxidation of  $\text{CO}_{\text{ad}}$ .

The coverage of CO was measured by varying the chronoamperometry time (0.1 to 150 s). Previous researches have shown that the rate of CO<sub>ad</sub> formation from methanol on a Pt surface can be modeled by Elovich equation (Eq. (4)), which assumes a linear dependence of the activation barrier for methanol dehydrogenation on CO coverage [66-69]. Figure 2-6 shows the CO-coverage behavior as a function of reaction time, and is fitted by:

$$\frac{d\theta_{\text{CO}}}{dt} = k_a C_m \exp(-\alpha\theta_{\text{CO}}), \quad (4)$$

where  $k_a$  is the rate constant for methanol dehydrogenation,  $C_m$  is the methanol concentration (0.1 M in this experiment), and  $\alpha$  reflects the effect of repulsive CO interactions on the rate of methanol dehydrogenation. The CO coverage was measured from the charges corresponding to the oxidation of the adsorbed CO which can be obtained by integrating the CO stripping peak of Fig. 2-5 after background subtraction. With the initial condition of  $\theta_{\text{CO}} = 0$  at  $t = 0$ , we obtained the rate constant for methanol dehydrogenation of each sample. Before this process, we obtained  $\alpha$  from each sample, and the average value of  $\alpha$  was used to acquire a more reliable rate constant  $k_a$  for methanol dehydrogenation (Fig. 2-7).

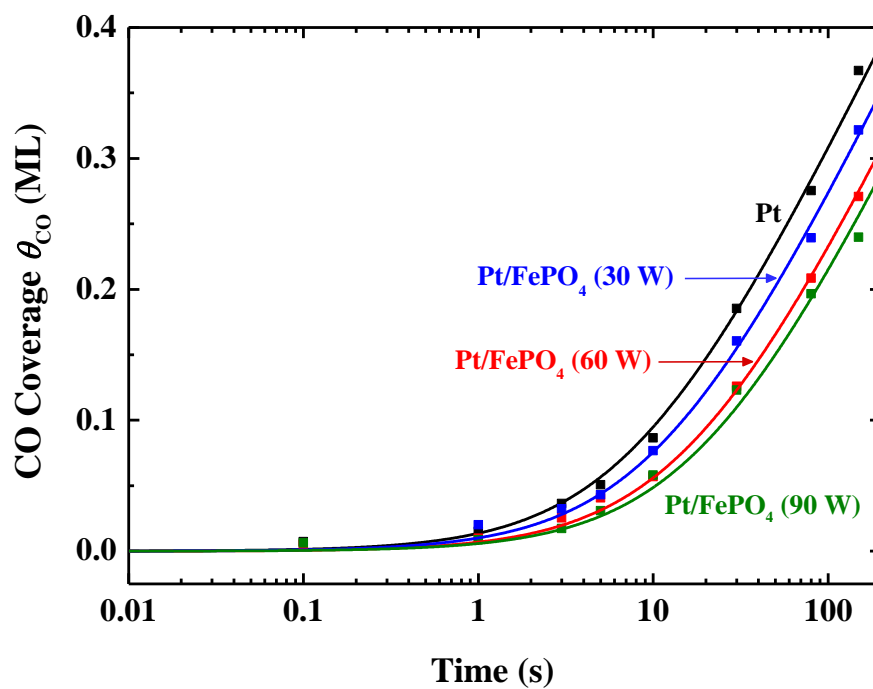


Fig. 2-6. (Color) CO coverage vs. time for each Pt surface prepared by different sputtering powers of FePO<sub>4</sub>. The CO<sub>ad</sub> coverage was obtained from CV scan at the rate of 3 V/s in 0.1 M HClO<sub>4</sub> + 0.1 M CH<sub>3</sub>OH (Fig. 2), and fitted from Eq. (4).

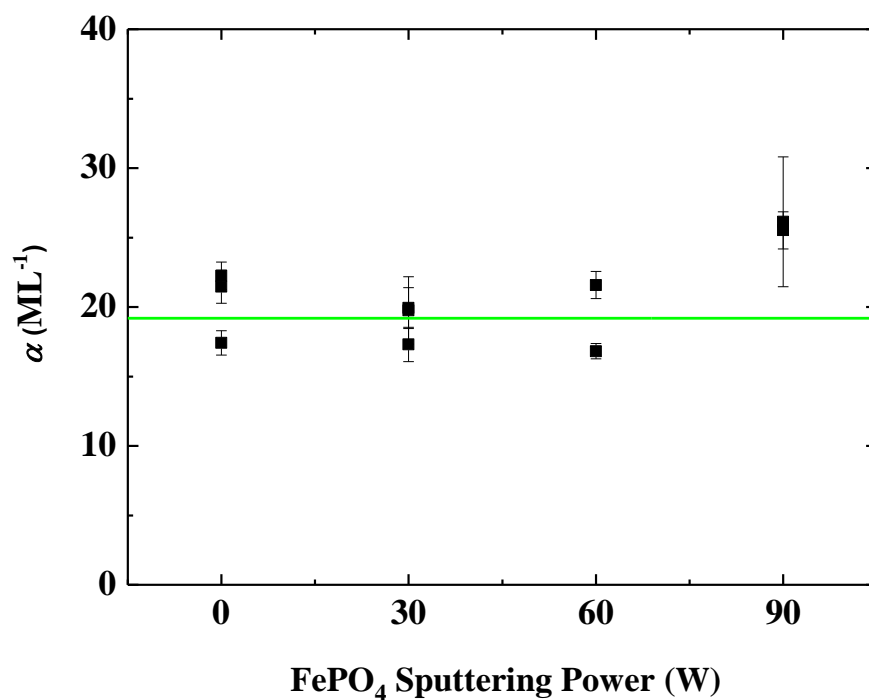


Fig. 2-7. (Color) Plot of  $\alpha$  as a function of FePO<sub>4</sub> sputtering power. In Eq. (4),  $\alpha$  reflects the effect of repulsive CO interactions on the rate of methanol dehydrogenation; we did not find any considerable variations or tendency in  $\alpha$  for different samples. So,  $\alpha$  was obtained from each data, and the average value of  $\alpha$  ( $19.2 \pm 0.9 \text{ ML}^{-1}$ ) was used to obtain the rate constant  $k_a$  for methanol dehydrogenation with the fitting from Fig. 2-6.

Figure 2-8 clearly exhibits the trend that methanol-dehydrogenation activity  $k_a$  decreases with the downshift of the  $d$ -band center (from the valence-band spectra of Fig. S5). On the Pt surface, the dissociative adsorption of methanol involving first-hydrogen extraction by O-H or C-H bond scission is regarded as the rate-determining step of methanol dehydrogenation [16,70,71]. Since the methanol-desorption barrier is less than that for the O-H or C-H scission [70,72], methanol desorption is often observed on Pt surfaces in ultra-high vacuum [73-75]. From this point of view, a stronger adsorption of methanol on Pt may induce a higher methanol-dehydrogenation rate by increasing the likelihood of O-H or C-H scission, and finally lead to very stable  $\text{CO}_{\text{ad}}$  through subsequent exothermic reactions. Therefore, the decrease in the rate constant can originate from direct methanol desorption without bond scission and following catalytic reactions, since the downshift of the  $d$ -band center implies a weaker adsorption of reactant molecules on the Pt. It should be noted that these kinds of arguments can be more systematically described when the changes of the activation barrier and adsorption energy of each reaction step are calculated according to the  $d$ -band shift of Pt by considering the scaling properties in the adsorption energies of adsorbed reaction intermediates or by considering the Brønsted-Evans-Polanyi relationships, which have been established between activation barriers and reaction energies for surface reactions [18,20,76-80].

In addition, the higher position of the  $d$ -band center relative to the Fermi-level not only results in the strong binding of a reactant on Pt, but also the strong binding of spectator species in the electrolyte, such as specifically-adsorbed anions, underpotentially-deposited hydrogen ( $\text{H}_{\text{upd}}$ ),  $\text{OH}_{\text{ad}}$  and other non-reactive molecular species which block the available

Pt sites for methanol adsorption [24,41,81]. Therefore, optimum point of reaction rate would exist at a suitable position of the  $d$ -band center, and the so-called volcano-type relation should appear [24]. However, in this experiment, since we covered only the downshift of the  $d$ -band center, further study is needed on the region of higher  $d$ -band center relative to pure Pt by opposite metal-phosphate selection to establish the overall trend of methanol dehydrogenation.

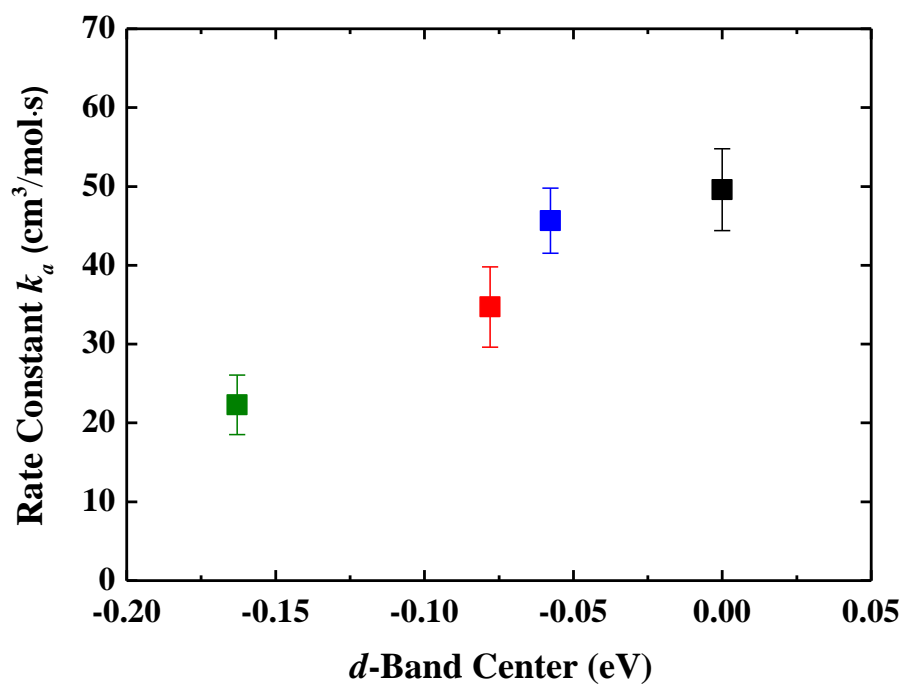


Fig. 2-8. (Color) Rate constant for methanol dehydrogenation on Pt surfaces as a function of the  $d$ -band center, as measured from the valence-band spectra in Fig. 2-9 (relative to pure Pt).

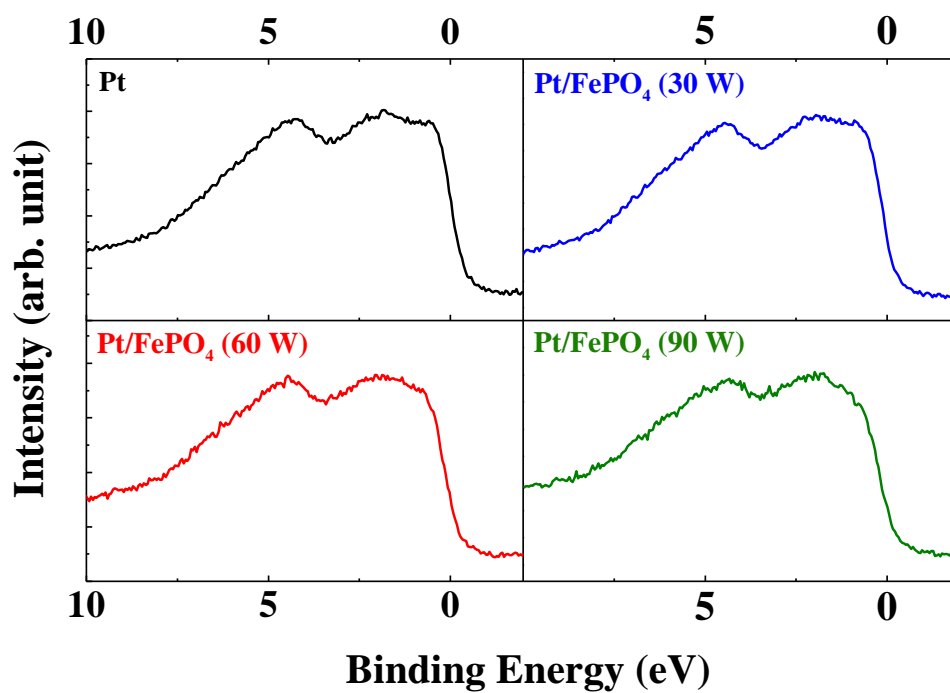


Fig. 2-9. (Color) The valence-band spectra for Pt and Pt/FePO<sub>4</sub> composites with various sputtering powers of FePO<sub>4</sub>.

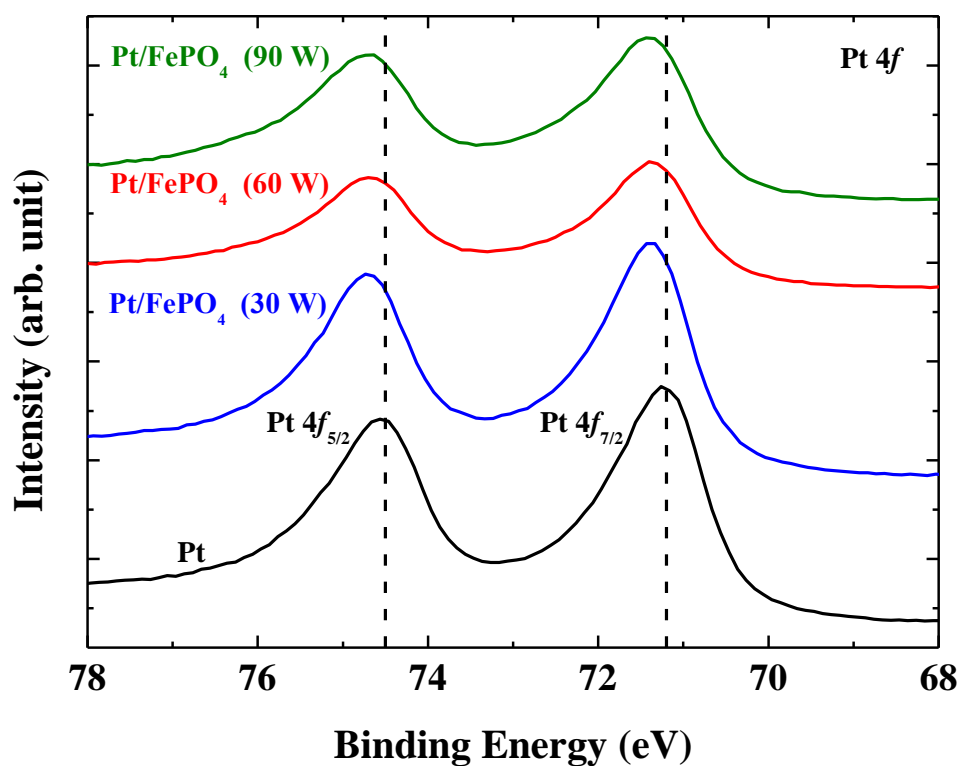


Fig. 2-10. (Color) Rate constant for methanol dehydrogenation on Pt surfaces as a function of the *d*-band center, as measured from the valence-band spectra in Fig. S5 (relative to pure Pt).

## 2.4. Conclusions

To identify the electronic effect during a methanol-oxidation reaction, we separated the CO-oxidation process by introducing an elaborate potential control. With this approach, we could systematically study the electronic effect on methanol dehydrogenation without concern for any unfavorable effects. We confirmed that the dehydrogenation activity of the Pt surface decreases with the downshift of the *d*-band center. Through further incorporation of CO-oxidation properties or the bifunctional effect, advanced designs of methanol-oxidation catalysts can be achieved. Also, this kind of potential-control strategy can be applied to other catalytic reactions, such as ethanol oxidation or formic acid oxidation to resolve otherwise-complicated catalytic reactions with the proper tuning of the electronic structure.

## 2.5. References

1. Winter, M.; Brodd, R. J. What Are Batteries, Fuel Cells, and Supercapacitors? *Chem. Rev.* **2004**, *104*, 4245-4269.
2. Steele, B. C. H.; Heinzel, A. Materials for Fuel-Cell Technologies. *Nature* **2001**, *414*, 345-352.
3. Antolini, E. Catalysts for Direct Ethanol Fuel Cells. *J. Power Sources* **2007**, *170*, 1-12.
4. Carrette, L.; Friedrich, K. A.; Stimming, U. Fuel Cells-Fundamentals and Applications. *Fuel Cells* **2001**, *1*, 5-39.
5. Spendelow, J. S.; Wieckowski, A. Electrocatalysis of Oxygen Reduction and Small Alcohol Oxidation in Alkaline Media. *Phys. Chem. Chem. Phys.* **2007**, *9*, 2654-2675.
6. Wang, C.-Y. Fundamental Models for Fuel Cell Engineering. *Chem. Rev.* **2004**, *104*, 4727-4766.
7. Swider-Lyons, K. E.; Campbell, S. A. Physical Chemistry Research Toward Proton Exchange Membrane Fuel Cell Advancement. *J. Phys. Chem. Lett.* **2013**, *4*, 393-401.
8. Gasteiger, H. A.; Kocha, S. S.; Sompalli, B.; Wagner, F. T. Activity Benchmarks and Requirements for Pt, Pt-Alloy, and Non-Pt Oxygen Reduction Catalysts for PEMFCs. *Appl. Catal. B-Environ.* **2005**, *56*, 9-35.
9. Liu, H.; Song, C.; Zhang, L.; Zhang, J.; Wang, H.; Wilkinson, D. P. A Review of Anode Catalysis in the Direct Methanol Fuel Cell. *J. Power Sources* **2006**, *155*, 95-110.
10. Wang, B. Recent Development of Non-Platinum Catalysts for Oxygen Reduction Reaction. *J. Power Sources* **2005**, *152*, 1-15.
11. Kang, S.; Lee, J.; Lee, J. K.; Chung, S.-Y.; Tak, Y. Influence of Bi Modification of Pt Anode Catalyst in Direct Formic Acid Fuel Cells. *J. Phys. Chem. B* **2006**, *110*, 7270-7274.

12. He, T.; Kreidler, E.; Xiong, L.; Ding, E. Combinatorial Screening and Nano-Synthesis of Platinum Binary Alloys for Oxygen Electroreduction. *J. Power Sources* **2007**, *165*, 87-91.
13. Suntivich, J.; Xu, Z.; Carlton, C. E.; Kim, J.; Han, B.; Lee, S. W.; Bonnet, N.; Marzari, N.; Allard, L. F.; Gasteiger, H. A.; et al. Surface Composition Tuning of Au-Pt Bimetallic Nanoparticles for Enhanced Carbon Monoxide and Methanol Electro-Oxidation. *J. Am. Chem. Soc.* **2013**, *135*, 7985-7991.
14. Hammer, B.; Nørskov, J. K. Electronic Factors Determining the Reactivity of Metal Surfaces. *Surf. Sci.* **1995**, *343*, 211-220.
15. Pallassana, V.; Neurock, M.; Hansen, L. B.; Hammer, B.; Nørskov, J. K. Theoretical Analysis of Hydrogen Chemisorption on Pd(111), Re(0001) and Pd<sub>ML</sub>/Re(0001), Re<sub>ML</sub>/Pd(111) Pseudomorphic Overlayers. *Phys. Rev. B* **1999**, *60*, 6146-6154.
16. Greeley, J.; Nørskov, J. K.; Mavrikakis, M. Electronic Structure and Catalysis on Metal Surfaces. *Annu. Rev. Phys. Chem.* **2002**, *53*, 319-348.
17. Nilsson, A.; Pettersson, L. G. M.; Hammer, B.; Bligaard, T.; Christensen, C. H.; Nørskov, J. K. The Electronic Structure Effect in Heterogeneous Catalysis. *Catal. Lett.* **2005**, *100*, 111-114.
18. Nørskov, J. K.; Bligaard, T.; Rossmeisl, J.; Christensen, C. H. Toward the Computational Design of Solid Catalysts. *Nat. Chem.* **2009**, *1*, 37-46.
19. Jiang, T.; Mowbray, D. J.; Dobrin, S.; Falsig, H.; Hvolbaek, B.; Bligaard, T.; Nørskov, J. K. Trends in CO Oxidation Rates for Metal Nanoparticles and Close-Packed, Stepped, and Kinked Surfaces. *J. Phys. Chem. C* **2009**, *113*, 10548-10553.
20. Nørskov, J. K.; Abild-Pedersen, F.; Studt, F.; Bligaard, T. Density Functional Theory in Surface Chemistry. *Proc. Natl. Acad. Sci.* **2011**, *108*, 937-943.
21. Kibler, L. A.; El-Aziz, A. M.; Hoyer, R.; Kolb, D. M. Tuning Reaction Rates by Lateral Strain in a Palladium Monolayer. *Angew. Chem., Int. Ed.* **2005**, *44*, 2080-2084.

22. Lima, F. H. B.; Zhang, J.; Shao, M. H.; Sasaki, K.; Vukmirovic, M. B.; Ticianelli, E. A.; Adzic, R. R. Catalytic Activity-d-Band Center Correlation for the O<sub>2</sub> Reduction Reaction on Platinum in Alkaline Solutions. *J. Phys. Chem. C* **2007**, *111*, 404-410.
23. Stamenkovic, V.; Mun, B. S.; Mayrhofer, K. J. J.; Ross, P. N.; Markovic, N. M.; Rossmeisl, J.; Greeley, J.; Nørskov, J. K. Changing the Activity of Electrocatalysts for Oxygen Reduction by Tuning the Surface Electronic Structure. *Angew. Chem., Int. Ed.* **2006**, *45*, 2897-2901.
24. Stamenkovic, V. R.; Mun, B. S.; Arenz, M.; Mayrhofer, K. J. J.; Lucas, C. A.; Wang, G.; Ross, P. N.; Markovic, N. M. Trends in Electrocatalysis on Extended and Nanoscale Pt-Bimetallic Alloy Surfaces. *Nat. Mater.* **2007**, *6*, 241-247.
25. Stamenkovic, V. R.; Fowler, B.; Mun, B. S.; Wang, G.; Ross, P. N.; Lucas, C. A.; Markovic, N. M. Improved Oxygen Reduction Activity on Pt<sub>3</sub>Ni(111) via Increased Surface Site Availability. *Science* **2007**, *315*, 493-497.
26. Toyoda, E.; Jinnouchi, R.; Hatanaka, T.; Morimoto, Y.; Mitsuhara, K.; Visikovskiy, A.; Kido, Y. The d-Band Structure of Pt Nanoclusters Correlated with the Catalytic Activity for Oxygen Reduction Reaction. *J. Phys. Chem. C* **2011**, *115*, 21236-21240.
27. Yoo, S.; Kim, S.-K.; Jeon, T.-Y.; Hwang, S.; Lee, J.-G.; Lee, S.-C.; Lee, K.-S.; Cho, Y.-H.; Sung, Y.-E.; Lim, T.-H. Enhanced Stability and Activity of Pt-Y Alloy Catalysts for Electrocatalytic Oxygen Reduction. *Chem. Comm.* **2011**, *47*, 11414-11416.
28. Yoo, S.; Hwang, S.; Lee, J.-G.; Lee, S.-C.; Lim, T.-H.; Sung, Y.-E.; Wieckowski, A.; Kim, S.-K. Promoting Effects of La for Improved Oxygen Reduction Activity and High Stability of Pt on Pt-La Alloy Electrodes. *Energy Environ. Sci.* **2012**, *5*, 7521-7525.
29. Hwang, S.; Kim, S.-K.; Lee, J.-G.; Lee, S.-C.; Jang, J.; Kim, P.; Lim, T.-H.; Sung, Y.-E.; Yoo, S. Role of Electronic Perturbation in Stability and Activity of Pt-Based Alloy Nanocatalysts for Oxygen Reduction. *J. Am. Chem. Soc.* **2012**, *134*, 19508-19511.

30. Iwasita, T. Electrocatalysis of Methanol Oxidation. *Electrochim. Acta* **2002**, *47*, 3663-3674.
31. Gasteiger, H. A.; Markovic, N.; Ross, P. N.; Cairns, E. J. Methanol Electrooxidation on Well-Characterized Pt-Ru Alloys. *J. Phys. Chem.* **1993**, *97*, 12020-12029.
32. Watanabe, M.; Motoo, S. Electrocatalysis by Ad-Atoms: Part III. Enhancement of the Oxidation of Carbon Monoxide on Platinum by Ruthenium Ad-Atoms. *J. Electroanal. Chem.* **1975**, *60*, 275-283.
33. Swathirajan, S.; Mikhail, Y. M. Electrochemical Oxidation of Methanol at Chemically Prepared Platinum-Ruthenium Alloy Electrodes. *J. Electrochem. Soc.* **1991**, *138*, 1321-1326.
34. Cao, D.; Lu, G.-Q.; Wieckowski, A.; Wasileski, S. A.; Neurock, M. Mechanisms of Methanol Decomposition on Platinum: A Combined Experimental and ab Initio Approach. *J. Phys. Chem. B* **2005**, *109*, 11622-11633.
35. Parsons, R.; Vandernoot, T. The Oxidation of Small Organic Molecules: A Survey of Recent Fuel Cell Related Research. *J. Electroanal. Chem.* **1988**, *257*, 9-45.
36. Capon, A.; Parsons, R. The Oxidation of Formic Acid at Noble Metal Electrodes: Part III. Intermediates and Mechanism on Platinum Electrodes. *J. Electroanal. Chem.* **1973**, *45*, 205-231.
37. Batista, E. A.; Malpass, G. R. P.; Motheo, A. J.; Iwasita, T. New Insight into the Pathways of Methanol Oxidation. *Electrochem. Commun.* **2003**, *5*, 843-846.
38. Herrero, E.; Chrzanowski, W.; Wieckowski, A. Dual Path Mechanism in Methanol Electrooxidation on a Platinum Electrode. *J. Phys. Chem.* **1995**, *99*, 10423-10424.
39. Sriramulu, S.; Jarvi, T. D.; Stuve, E. M. Reaction Mechanism and Dynamics of Methanol Electrooxidation on Platinum(111). *J. Electroanal. Chem.* **1999**, *467*, 132-142.

40. Cuesta, A. At Least Three Contiguous Atoms Are Necessary for CO Formation during Methanol Electrooxidation on Platinum. *J. Am. Chem. Soc.* **2006**, *128*, 13332-13333.
41. Markovic, N. M.; Ross, P. N. Surface Science Studies of Model Fuel Cell Electrocatalysts. *Surf. Sci. Rep.* **2002**, *45*, 117-229.
42. Evarts, S. E.; Kendrick, I.; Wallstrom, B. L.; Mion, T.; Abedi, M.; Dimakis, N.; Smotkin, E. S. Ensemble Site Requirements for Oxidative Adsorption of Methanol and Ethanol on Pt Membrane Electrode Assemblies. *ACS Catal.* **2012**, *2*, 701-707.
43. Tritsaris, G. A.; Rossmeisl, J. Methanol Oxidation on Model Elemental and Bimetallic Transition Metal Surfaces. *J. Phys. Chem. C* **2012**, *116*, 11980-11986.
44. Lu, C.; Rice, C.; Masel, R. I.; Babu, P. K.; Waszczuk, P.; Kim, H. S.; Oldfield, E.; Wieckowski, A. UHV, Electrochemical NMR, and Electrochemical Studies of Platinum/Ruthenium Fuel Cell Catalysts. *J. Phys. Chem. B* **2002**, *106*, 9581-9589.
45. Spendelow, J. S.; Babu, P. K.; Wieckowski, A. Electrocatalytic Oxidation of Carbon Monoxide and Methanol on Platinum Surfaces Decorated with Ruthenium. *Curr. Opin. Solid St. M.* **2005**, *9*, 37-48.
46. Lu, G.-Q.; Chrzanowski, W.; Wieckowski, A. Catalytic Methanol Decomposition Pathways on a Platinum Electrode. *J. Phys. Chem. B* **2000**, *104*, 5566-5572.
47. Iwasita, T.; Xia, X. H.; Liess, H.-D.; Vielstich, W. Electrocatalysis of Organic Oxidations: Influence of Water Adsorption on the Rate of Reaction. *J. Phys. Chem. B* **1997**, *101*, 7542-7547.
48. Markovic, N. M.; Gasteiger, H. A.; Ross, P. N.; Jiang, X.; Villegas, I.; Weaver, M. J. Electro-Oxidation Mechanisms of Methanol and Formic Acid on Pt-Ru Alloy Surfaces. *Electrochim. Acta* **1995**, *40*, 91-98.
49. Vielstich, W.; Lamm, A.; Gasteiger, H. A. Handbook of Fuel Cells; John Wiley & Sons Ltd.: New York, 2003; Vol. 2: Electrocatalysis.

50. Cheetham, A. K.; Ferey, G.; Loiseau, T. Open-Framework Inorganic Materials. *Angew. Chem., Int. Ed.* **1999**, *38*, 3268-3292.
51. Lee, B.; Kim, C.; Park, Y.; Kim, T.-G.; Park, B. Nanostructured Platinum/Iron-Phosphate Thin-Film Electrodes for Methanol Oxidation. *Electrochem. Solid-State Lett.* **2006**, *9*, E27-E30.
52. Kim, C.; Lee, B.; Park, Y.; Park, B.; Lee, J.; Kim, H. Iron-Phosphate/Platinum/Carbon Nanocomposites for Enhanced Electrocatalytic Stability. *Appl. Phys. Lett.* **2007**, *91*, 113101.
53. Park, Y.; Lee, B.; Kim, C.; Kim, J.; Nam, S.; Oh, Y.; Park, B. Modification of Gold Catalysis with Aluminum Phosphate for Oxygen-Reduction Reaction. *J. Phys. Chem. C* **2010**, *114*, 3688-3692.
54. Cho, J.; Kim, Y.-W.; Kim, B.; Lee, J.-G.; Park, B. A Breakthrough in the Safety of Lithium Secondary Batteries by Coating the Cathode Material with AlPO<sub>4</sub> Nanoparticles. *Angew. Chem., Int. Ed.* **2003**, *42*, 1618-1621.
55. Park, Y.; Nam, S.; Oh, Y.; Choi, H.; Park, J.; Park, B. Electrochemical Promotion of Oxygen Reduction on Gold with Aluminum-Phosphate Overlayer. *J. Phys. Chem. C* **2011**, *115*, 7092-7096.
56. Bouwman, P. J.; Dmowski, W.; Stanley, J.; Cotten, G. B.; Swider-Lyons, K. E. Platinum-Iron Phosphate Electrocatalysts for Oxygen Reduction in PEMFCs. *J. Electrochem. Soc.* **2004**, *151*, A1989-A1998.
57. Shao, M.; Peles, A.; Shoemaker, K. Electrocatalysis on Platinum Nanoparticles: Particle Size Effect on Oxygen Reduction Reaction Activity. *Nano Lett.* **2011**, *11*, 3714-3719.
58. Watanabe, M.; Saegusa, S.; Stonehart, P. High Platinum Electrocatalyst Utilizations for Direct Methanol Oxidation. *J. Electroanal. Chem.* **1989**, *271*, 213-220.
59. Frelink, T.; Visscher, W.; Veen, J. A. R. V. Particle Size Effect of Carbon-Supported Platinum Catalysts for the Electrooxidation of Methanol. *J. Electroanal. Chem.* **1995**, *382*, 65-72.

60. Giordano, N.; Passalacqua, E.; Pino, L.; Arico, A. S.; Antonucci, V.; Vivaldi, M.; Kinoshita, K. Analysis of Platinum Particle Size and Oxygen Reduction in Phosphoric Acid. *Electrochim. Acta* **1991**, *36*, 1979-1984.
61. Sattler, M. L.; Ross, P. N. The Surface Structure of Pt Crystallites Supported on Carbon Black. *Ultramicroscopy* **1986**, *20*, 21-28.
62. Peuckert, M.; Yoneda, T.; Betta, R. A. D.; Boudart, M. Oxygen Reduction on Small Supported Platinum Particles. *J. Electrochem. Soc.* **1986**, *133*, 944-947.
63. Kinoshita, K. Particle Size Effects for Oxygen Reduction on Highly Dispersed Platinum in Acid Electrolytes. *J. Electrochem. Soc.* **1990**, *137*, 845-848.
64. Sheng, W.; Chen, S.; Vescovo, E.; Shao-Horn, Y. Size Influence on the Oxygen Reduction Reaction Activity and Instability of Supported Pt Nanoparticles. *J. Electrochem. Soc.* **2012**, *159*, B96-B103.
65. Lu, G.-Q.; Crown, A.; Wieckowski, A. Formic Acid Decomposition on Polycrystalline Platinum and Palladized Platinum Electrodes. *J. Phys. Chem. B* **1999**, *103*, 9700-9711.
66. Spendelow, J. S.; Goodpaster, J. D.; Kenis, P. J. A.; Wieckowski, A. Methanol Dehydrogenation and Oxidation on Pt(111) in Alkaline Solutions. *Langmuir* **2006**, *22*, 10457-10464.
67. Bagotzky, V. S.; Vassiliev, Y. B. Adsorption of Organic Substances on Platinum Electrodes. *Electrochim. Acta* **1966**, *11*, 1439-1461.
68. Seiler, T.; Savinova, E. R.; Friedrich, K. A.; Stimming, U. Poisoning of PtRu/C Catalysts in the Anode of a Direct Methanol Fuel Cell: A DEMS Study. *Electrochim. Acta* **2004**, *49*, 3927-3936.
69. Khazova, O. A.; Mikhailova, A. A.; Skundin, A. M.; Tuseeva, E. K.; Havranek, A.; Wippermann, K. Kinetics of Methanol Oxidation on Supported and Unsupported Pt/Ru Catalysts Bonded to PEM. *Fuel Cells* **2002**, *2*, 99-108.

70. Greeley, J.; Mavrikakis, M. A First-Principles Study of Methanol Decomposition on Pt(111). *J. Am. Chem. Soc.* **2002**, *124*, 7193-7201.
71. Ferrin, P.; Mavrikakis, M. Structure Sensitivity of Methanol Electrooxidation on Transition Metals. *J. Am. Chem. Soc.* **2009**, *131*, 14381-14389.
72. Desai, S. K.; Neurock, M.; Kourtakis, K. A Periodic Density Functional Theory Study of the Dehydrogenation of Methanol over Pt(111). *J. Phys. Chem. B* **2002**, *106*, 2559-2568.
73. Gibson, K. D.; Dubois, L. H. Step Effects in the Thermal Decomposition on Methanol on Pt(111). *Surf. Sci.* **1990**, *233*, 59-64.
74. Sexton, B. A. Methanol Decomposition on Platinum (111). *Surf. Sci.* **1981**, *102*, 271-281.
75. Ehlers, D. H.; Spitzer, A.; Lüth, H. The Adsorption of Methanol on Pt(111), An IR Reflection and UV Photoemission Study. *Surf. Sci.* **1985**, *160*, 57-69.
76. Abild-Pedersen, F.; Greeley, J.; Studt, F.; Rossmeisl, J.; Munter, T. R.; Moses, P. G.; Skúlason, E.; Bligaard, T.; Nørskov, J. K. Scaling Properties of Adsorption Energies for Hydrogen-Containing Molecules on Transition-Metal Surfaces. *Phys. Rev. Lett.* **2007**, *99*, 016105.
77. Wang, S.; Petzold, V.; Tripkovic, V.; Kleis, J.; Howalt, J. G.; Skúlason, E.; Fernández, E. M.; Hvolbaek, B.; Jones, G.; Toftelund, A.; et al. Universal Transition State Scaling Relations for (De)hydrogenation over Transition Metals. *Phys. Chem. Chem. Phys.* **2011**, *13*, 20760-20765.
78. Sutton, J. E.; Vlachos, D. G. A Theoretical and Computational Analysis of Linear Free Energy Relations for the Estimation of Activation Energies. *ACS Catal.* **2012**, *2*, 1624-1634.
79. Michaelides, A.; Liu, Z.-P.; Zhang, C. J.; Alavi, A.; King, D. A.; Hu, P. Identification of General Linear Relationships between Activation Energies and Enthalpy Changes for Dissociation Reactions at Surfaces. *J. Am. Chem. Soc.* **2003**, *125*, 3704-3705.

80. Mehmood, F.; Rankin, R. B.; Greeley, J.; Curtiss, L. A. Trends in Methanol Decomposition on Transition Metal Alloy Clusters from Scaling and Brønsted-Evans-Polanyi relationships. *Phys. Chem. Chem. Phys.* **2012**, *14*, 8644-8652.
81. Kita, H.; Gao, Y.; Nakato, T.; Hattori, H. Effect of Hydrogen Sulphate Ion on the Hydrogen Ionization and Methanol Oxidation Reactions on Platinum Single-Crystal Electrodes. *J. Electroanal. Chem.* **1994**, *373*, 177-183.

## **Chapter 3.**

# **Breathable Carbon-Free Electrode: Black TiO<sub>2</sub> with Hierarchically-Ordered Porous Structure for Stable Li-O<sub>2</sub> Batteries**

### **3.1. Introduction**

With increase in our society's demands for energy storage, conventional Li-ion batteries (LIBs) are now reaching the limit in terms of energy density and price [1-3]. In particular, rapid development and commercialization of electric vehicles (EVs) and energy storage systems (ESS) need more cost-effective, higher energy-density power sources, which cannot be fully satisfied by current progress of Li-ion batteries [4-8]. As an alternative, Li-O<sub>2</sub> batteries are now attracting tremendous interest due to their extremely high theoretical energy density (~3500 Wh kg<sup>-1</sup>), which is far higher than that of conventional Li-ion batteries (~400 Wh kg<sup>-1</sup>) [6-9]. Unlike Li-ion batteries, which often contain heavy transition metals as redox-active elements in the crystal structure of cathodes, the Li-O<sub>2</sub> system takes only adequate substrates for the discharge/charge reactions ( $2\text{Li}^+ + 2\text{e}^- + \text{O}_2 \leftrightarrow \text{Li}_2\text{O}_2$ ), since oxygen can be supplied from air.

As an aforementioned substrate, carbon has been ubiquitously used with various forms (carbon black, CNT, graphene, and etc.), due to such advantages as light weight, large surface area, and high electronic conductivity with relatively low cost from which high energy density can be drawn [10-15].

However, parasitic reactions originating from complex interactions with battery components such as carbon additives, discharge products, electrolyte, and binder are especially aggravated on carbon, which leads to the premature cell death constraining it from being used for air cathodes [16-18]. In the meantime, Bruce's group suggested titanium carbide (TiC) as an alternative for such carbon cathodes [19]. Compared with carbon, they showed that the TiC greatly reduced side reactions with the electrolyte and electrode degradation, and exhibited reversible formation/decomposition of  $\text{Li}_2\text{O}_2$ , along with their previous work of nanoporous Au [20]. In the circumstances, several researchers continued to work on titanium-based materials (TiSi<sub>2</sub> [21], TiO<sub>2</sub> [22-24], TiN [25], and Ti<sub>4</sub>O<sub>7</sub> [26,27]) to prove that such materials can be promising substrates in terms of gravimetric energy density, cost, environmental benignity, or so.

A notable feature of TiC is surface-present TiO<sub>2</sub>, which is expected to protect the bulk side of TiC against further oxidation and side reactions, sustaining sufficient activity for discharge/charge reactions [20,28]. Considering that the surface reaction of Li-O<sub>2</sub> batteries relies on the surface chemistry of electrode, this observation implies that TiO<sub>2</sub> can solely operate as a stable cathode for Li-O<sub>2</sub> system, only provided that proper electrical conductivity is guaranteed. In case of magnéli Ti<sub>4</sub>O<sub>7</sub> cathode, studied by Nazar's group, the surface of Ti<sub>4</sub>O<sub>7</sub> was revealed to be oxygen-deficient TiO<sub>2-x</sub>, and the substoichiometry was maintained after exposure to oxygen-rich environment on discharge/charge [26].

This oxygen deficient TiO<sub>2-x</sub> or so-called black TiO<sub>2</sub> can be synthesized by a simple H<sub>2</sub>-thermal treatment on pure TiO<sub>2</sub>, which requires more-available synthetic condition than that of TiC or Ti<sub>4</sub>O<sub>7</sub> in terms of reductive atmosphere and temperature. The Ti<sup>3+</sup> ions and

oxygen vacancies generated in this process are known to furnish various novel properties, including high electronic conductivity [29-31] and catalytic activity [32,33]. Therefore, studies on the air cathode with bulk  $\text{TiO}_{2-x}$  seem to be necessary to account for the potential application of titanium-based materials.

Along with the investigation of material itself, tailoring the electrode architecture is another crucial part of developing an efficient and stable cathode. Even though recent studies demonstrated that discharge capacity could be dramatically increased up by solvent-mediated growth of  $\text{Li}_2\text{O}_2$  [34-36], efficient architectures for the utilization of such solution-growth mechanism are still in question. One might think of introducing macropores to the electrode as one of the strategies, where such large particles can be efficiently incorporated in the electrode structure without being clogged.

Furthermore, since the emergence of soluble catalysts as alternatives to conventional solid catalysts (Pt, Au,  $\text{RuO}_2$ , and etc.) [37-39], air-permeable architectures containing sufficient and sustainable diffusion paths has been considered an effective way of enhancing the transport kinetics of soluble catalysts as well as oxygen and other reaction species [40]. Therefore, an air cathode for high-performance Li- $\text{O}_2$  batteries necessarily features the combined characteristics of proper electrical conductivity and advantageous architecture, available for the use of a soluble catalyst.

In this work, oxygen-deficient black  $\text{TiO}_2$  with the ordered macro-/mesoporous structure is fabricated by a simple hydrogen thermal treatment, and applied in Li- $\text{O}_2$  battery as a carbon- and binder-free electrode. A soluble catalyst, LiI, was also introduced as an enhancer for the operation of the  $\text{TiO}_2$  electrode. Together with the proper electronic

conductivity derived from oxygen vacancies or  $\text{Ti}^{3+}$  ions, this hierarchical electrode has large surface area for the oxygen-reduction reaction (ORR), as well as the interconnected micron-sized empty spaces to accommodate discharge products and to facilitate diffusion of the reaction molecules and soluble catalyst without clogging of electrode. We observed, in this ordered architecture, that toroidal  $\text{Li}_2\text{O}_2$  particles were organized in a regular size and separation, sustaining large interface with electrolyte and facilitating the soluble catalyst to act upon the decomposition of  $\text{Li}_2\text{O}_2$ . Our designed electrode, namely, ‘breathable’ carbon-free electrode exhibited an enhanced polarization, hence, excellent round-trip efficiency over 300 cycles, especially with the use of LiI as a soluble catalyst.

## **3.2. Experimental Section**

### **3.2.1. Material Preparation**

Ni mesh was ultrasonically cleaned for 30 minutes in anhydrous ethanol (EtOH) and for 3 minutes in a 0.5 M hydrochloric acid (HCl) to remove any contaminants and amorphous surface oxides, then dried in vacuum chamber for overnight. After dried, Ni mesh was vertically immersed into 30 ml of 0.3 wt. % polystyrene-microbead solution, which was prepared by diluting polystyrene-microbead (PS) solution (2.5 wt. % in water, Alfa Aesar) with anhydrous ethanol. By keeping the Ni mesh in the PS solution at 60°C for overnight, PS microbeads were uniformly coated on the Ni mesh. As a titanium source, 1 ml of titanium chloride (TiCl<sub>4</sub>, Sigma-Aldrich) was slowly added into 50 ml of anhydrous ethanol, and stirred at ambient condition for 1 h. After stirring, 3 μl of TiCl<sub>4</sub> solution was dropped on PS/Ni mesh (0.79 cm<sup>2</sup>) by micropipette and infiltrated into the crevices between beads using vacuum-filtration method. After dried, this TiCl<sub>4</sub> treated PS/Ni mesh was transferred to box furnace and annealed at 400°C for 3 hours (ramping rate of 5°C/min) in air, to remove the PS template and form TiO<sub>2</sub>. For the synthesis of oxygen-deficient TiO<sub>2</sub>, as-prepared TiO<sub>2</sub>/Ni mesh was further annealed at 700°C for 10 h under a flow of mixed gas of 40% hydrogen (H<sub>2</sub>) and 60% argon (Ar) at a rate of 100 sccm.

### **3.2.2. Material Preparation**

X-ray diffraction (XRD, D8 Advance: Bruker) was used to characterize the crystal structure of TiO<sub>2</sub>/Ni mesh and black TiO<sub>2-x</sub>/Ni mesh, and therefore, to observe the change of TiO<sub>2</sub> phase during hydrogen thermal-treatment. The morphology of TiO<sub>2</sub> before

hydrogenation, hierarchically-ordered porous black TiO<sub>2</sub> (HOP-*b*TiO<sub>2</sub>), and discharged/charged HOP-*b*TiO<sub>2</sub> electrodes were analyzed using field-emission scanning electron microscopy (FE-SEM, Merlin Compact: Zeiss). Surface structure of TiO<sub>2</sub>, HOP-*b*TiO<sub>2</sub> with hydrogenation time of 10 h and 40 h, and discharged electrode (with Li<sub>2</sub>O<sub>2</sub>) were analyzed by high-resolution transmission electron microscopy (HRTEM, JEM-2100F: JEOL, Japan). To identify the effect of hydrogen thermal treatment on the chemical structure of TiO<sub>2</sub>, as synthesized TiO<sub>2</sub>/Ni sample was annealed in different atmosphere: the one was in the mixed gas of H<sub>2</sub> and Ar (same condition for HOP-*b*TiO<sub>2</sub> as a cathode), and the other was in air for 10 h as a control sample. The electronic structure of black TiO<sub>2</sub> and air-annealed TiO<sub>2</sub> were analyzed by x-ray photoelectron spectroscopy (XPS, AXIS-HIS: KRATOS) with incident photon of 1254 eV. The Raman spectra for the black TiO<sub>2</sub> and air-annealed TiO<sub>2</sub> were obtained by Raman spectroscopy (LabRAM HV Evolution: HORIBA), to compare the crystallinity and chemical structure of two samples. Nitrogen adsorption-desorption analysis were performed at 77 K up to 1 bar, using a Micromeritics ASAP 2020 static volumetric gas adsorption instrument.

### **3.2.3. Electrochemistry**

The electrochemical performance of the electrodes was examined using a modified Swagelok cell consisting of an air electrode, a metallic Li anode, a Whatman glass filter separator, and an electrolyte. The basic electrolyte was 1 M lithium bis(trifluoromethane)sulfonamide (LiTFSI) in tetraethylene glycol dimethylether (TEGDME), and 0.05 M of LiI was added as the soluble catalyst. The cells were

assembled in an Ar-filled glovebox and the electrochemical properties were measured by galvanostatic cycling using a WonATech battery cycler (WBCs 3000). The capacity was determined based on the weight of TiO<sub>2</sub> (~0.1 mg cm<sup>-2</sup>), which was obtained by subtracting the initial mass of Ni mesh from total mass of electrode after annealing process. For the cycling test, the capacity was limited to 1000 mAh g<sup>-1</sup> in order to prevent a large depth of discharge. All experiments were conducted under an O<sub>2</sub> pressure of 1 atm at 25°C.

### **3.3. Results and Discussion**

#### **3.3.1. Synthesis and characterization of hierarchically-ordered porous black TiO<sub>2</sub> electrode**

Figure 3-1 presents the synthetic procedure for preparing hierarchically-ordered porous black TiO<sub>2</sub> (HOP-*b*TiO<sub>2</sub>) on a Ni mesh. Monodisperse polystyrene (PS) latex microsphere with a size of ~1.5 μm were compactly loaded on/between each strand of Ni mesh and this PS/Ni was used as a template (Fig. 3-2) for the fabrication of ordered macroporous structure (see experimental section for the details). Titanium precursor solution was then impregnated into the interspaces between PS spheres, and ordered macroporous TiO<sub>2</sub> (OP-TiO<sub>2</sub>) crystals on the Ni mesh are obtained after calcination. During the subsequent hydrogen thermal treatment, anatase TiO<sub>2</sub> phase are converted to rutile, generating mesoporous surface, and finally HOP-*b*TiO<sub>2</sub> was fabricated on the Ni mesh (Fig. 3-3).

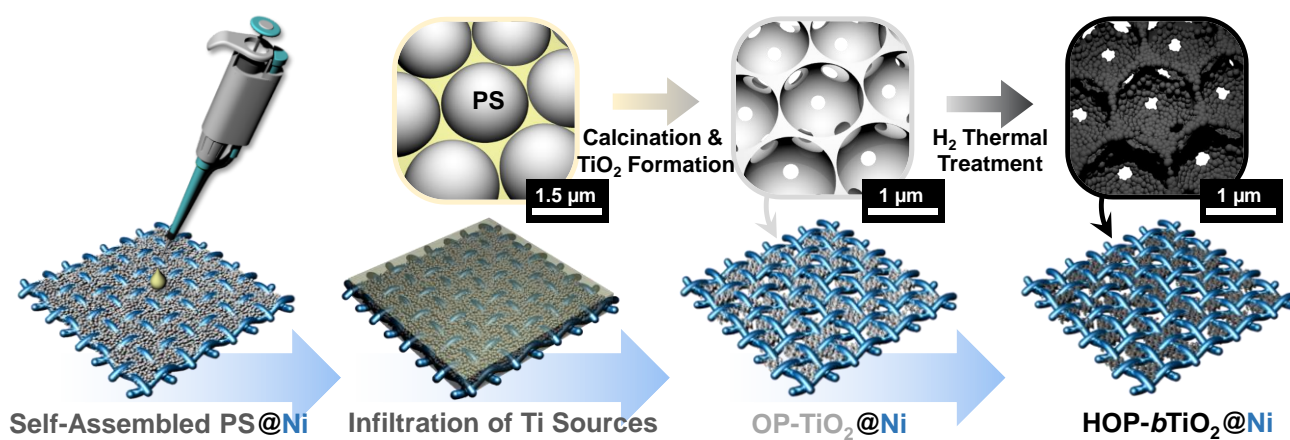


Fig. 3-1. (Color) Schematic illustration on the preparation for carbon-free electrode, composed of hierarchically-ordered porous black TiO<sub>2</sub> (HOP-*b*TiO<sub>2</sub>) on a Ni mesh. PS and OP-TiO<sub>2</sub> denote the polystyrene bead and ordered-porous TiO<sub>2</sub> before H<sub>2</sub> thermal treatment, respectively.

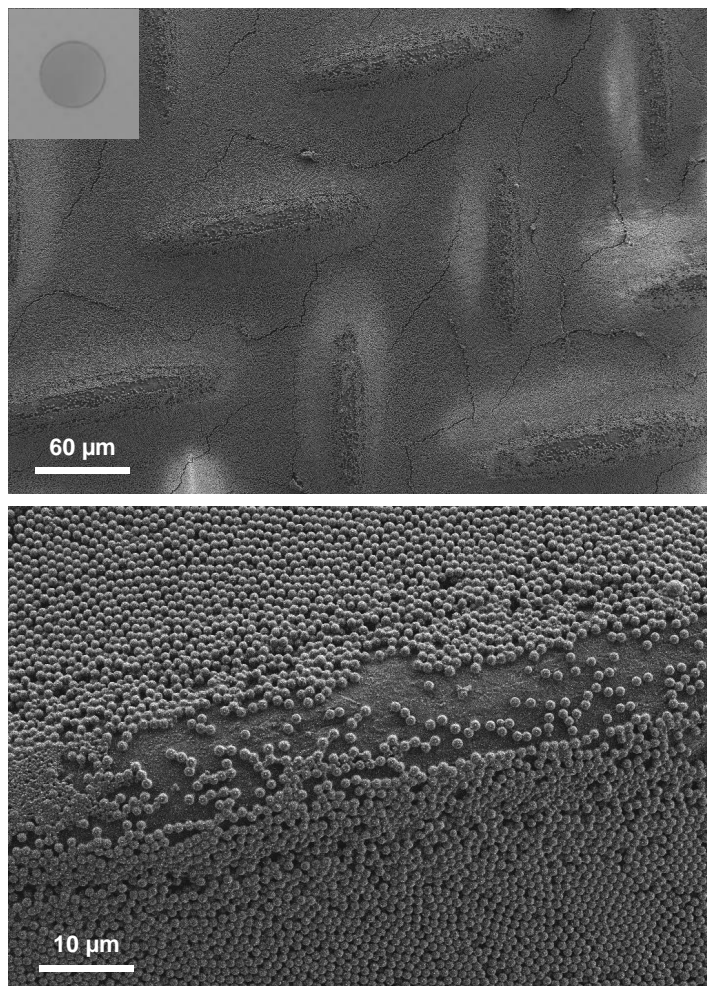


Fig. 3-2. SEM images of polystyrene filled Ni mesh (PS/Ni mesh) used as a template for the fabrication of ordered porous TiO<sub>2</sub>.

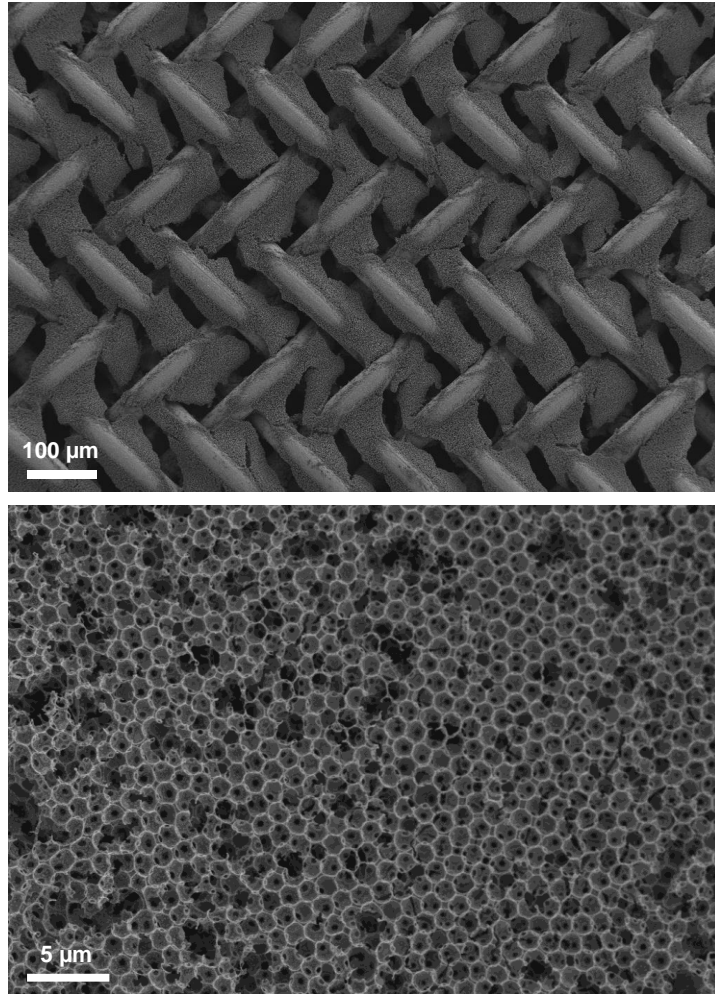


Fig. 3-3. SEM images of the HOP-*b*TiO<sub>2</sub> in various magnifications.

X-ray diffraction and photographs of the electrodes before and after H<sub>2</sub> thermal treatment in Figs. 3-4(a) and (b) clearly show the transformation of TiO<sub>2</sub> from anatase to the rutile phase. The color change from white to black is indicative of the modified optical and electronic properties by the partial reduction of Ti<sup>4+</sup> to Ti<sup>3+</sup>. The change of electronic structure in black TiO<sub>2</sub> is corroborated by x-ray photoelectron spectroscopy (XPS) in Fig. 3-4(c), where the control TiO<sub>2</sub> (rutile phase) is synthesized by post heat-treatment in air rather than in H<sub>2</sub> atmosphere after the formation of anatase TiO<sub>2</sub>. The binding energy of Ti 2*p* is slightly lower in black TiO<sub>2</sub> with respect to the stoichiometric TiO<sub>2</sub>, indicating that Ti ion in black TiO<sub>2</sub> surface has lower oxidation state than that of the control TiO<sub>2</sub>. Previous studies on oxygen deficient TiO<sub>2</sub> also observed red shift of the Ti-2*p* binding energy [41-43]. The oxygen vacancies (*V*<sub>o</sub>) created during hydrogenation lead to the formation of two electrons to keep the charge neutrality in the crystal structure. Such excess charges will be transferred to *t*<sub>2*g*</sub> orbitals of Ti, possibly reducing Ti<sup>4+</sup> to Ti<sup>3+</sup>. Ti *L*-edge soft x-ray absorption spectroscopy (sXAS) further supports the presence of Ti<sup>3+</sup> ion in the black TiO<sub>2</sub> (Fig. 3-5), where the peak-intensity (x-ray absorption by electron transition from 2*p* to 3*d* orbitals) ratio of *e*<sub>g</sub>/*t*<sub>2*g*</sub> is higher in black TiO<sub>2</sub> than that of the control TiO<sub>2</sub>. In filling *t*<sub>2*g*</sub> band by an electron, there is higher possibility in excitation of electrons to *e*<sub>g</sub> band level by absorption of the incident x-rays, and this could be the evidence of reduced status of TiO<sub>2</sub>. In addition, similar absorption features from PEY and TEY indicate that such reduction of Ti<sup>4+</sup> occurs in the bulk as well as the surface of TiO<sub>2</sub>, given that the detection depth in a TEY mode extends to a few tens of nanometers, and the size of TiO<sub>2</sub> particles is ~12 nm. The different surface characteristics of black TiO<sub>2</sub> and control

TiO<sub>2</sub> are also present in O 1s core-level XPS spectra in Fig. 3-6. Broad shoulder peak near main TiO<sub>2</sub> peak indicates the functionalized black TiO<sub>2</sub> surface with hydroxyl (OH) group during the hydrogenation process [41,42].

The scanning electron microscopic (SEM) images of Figs. 3-4(d) and (e) exhibit that the electrode consists of mesoporous frameworks or layers which provide large surface area for ORR/OER reactions. The close-packed anatase TiO<sub>2</sub> grains becomes loosely aggregated with the concurrent volume contraction by ~8% [44] during the H<sub>2</sub> reduction, which gives rise to mesoporous surface in HOP-*b*TiO<sub>2</sub>. As a result, HOP-*b*TiO<sub>2</sub> is an aggregates of regularly-arranged TiO<sub>2</sub> nanoparticles with the size of 12.3 ± 4.1 nm (Fig. 3-7). Meanwhile, the micron-sized regular empty spaces, surrounded by the mesoporous walls, are interconnected by the voids where the removed PS spheres resided, and came into contact each other. The interconnected voids could act as diffusion channels, and hence, reduce the tortuosity of the electrode [45,46]. This ordered-macroporous architecture, so-called inverse-opal structure, was already proven beneficial for fuel cell systems in which the enhanced mass-transfer or effective diffusivity of reaction molecules (methanol and oxygen) were demonstrated by increased current density in the mass-transfer controlled regions [47,48].

Raman spectroscopy (Fig. 3-4(f)) also confirms the defective structure of TiO<sub>2-x</sub> compared to the control TiO<sub>2</sub>. Compared to the relatively sharp *E<sub>g</sub>* and *A<sub>1g</sub>* mode peaks from the control rutile TiO<sub>2</sub>, defective black TiO<sub>2</sub> shows both broader peaks with the shift of *E<sub>g</sub>* peaks to the lower wavenumber. Such red shift and broadening of the *E<sub>g</sub>* peak in oxygen deficient TiO<sub>2</sub> were already reported in many literatures, and the phonon

confinement by bulk point defects or grain boundaries are known to be responsible for those behaviors [49,51]. Along with the surface  $\text{Ti}^{3+}$  ions observed by the XPS results, bulk oxygen defects in the  $\text{TiO}_2$  were also confirmed by Raman spectra, contributing to the enhanced electronic conductivity, as measured by the 4-point probe in pelletized forms (Fig. 3-8). The DC conductivity of black  $\text{TiO}_2$  is measured to be  $\sim 10^{-1} \text{ S cm}^{-1}$ , which is 7 orders of magnitude higher than that of  $\text{TiO}_2$  without reduction process ( $\sim 10^{-8} \text{ S cm}^{-1}$ ), which may originate from  $\text{Ti}^{3+}$  ions that generate shallow donor levels just below the conduction band minimum, giving rise to *n*-type conductivity [29]. By a simple  $\text{H}_2$  thermal treatment, suitable electronic conductivity and an advantageous architecture of  $\text{TiO}_2$  cathode was successfully obtained.

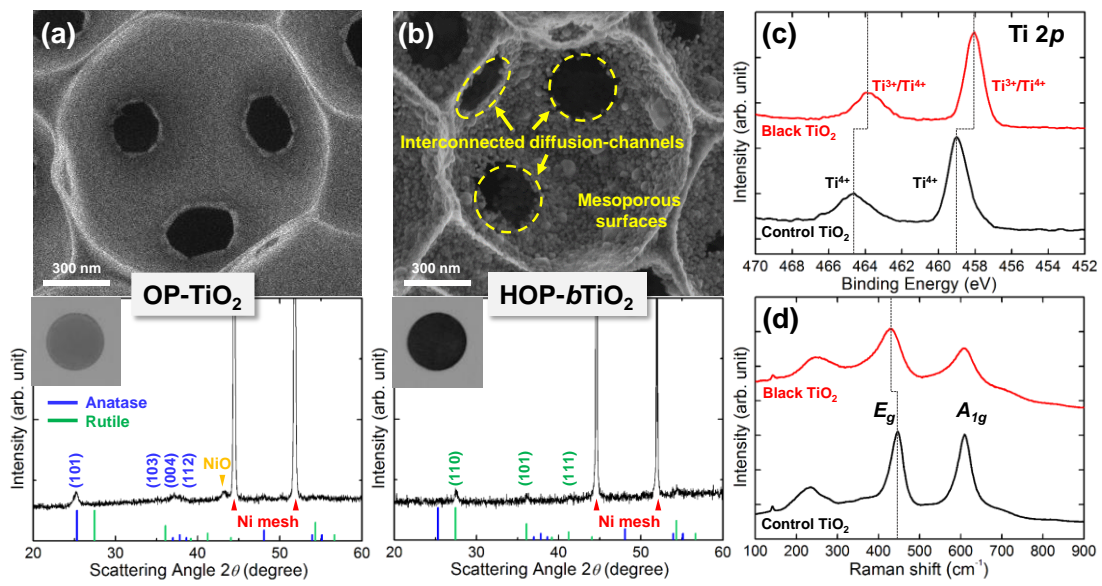


Fig. 3-4. (Color) SEM images and X-ray diffraction patterns of (a) the OP-TiO<sub>2</sub> (before H<sub>2</sub> thermal reduction) and (b) the HOP-bTiO<sub>2</sub> (after H<sub>2</sub> thermal reduction). (c) XPS spectra in the Ti 2p region for the black TiO<sub>2</sub> and control TiO<sub>2</sub> (rutile phase). (d) Raman spectra for the black TiO<sub>2</sub> and control TiO<sub>2</sub>.

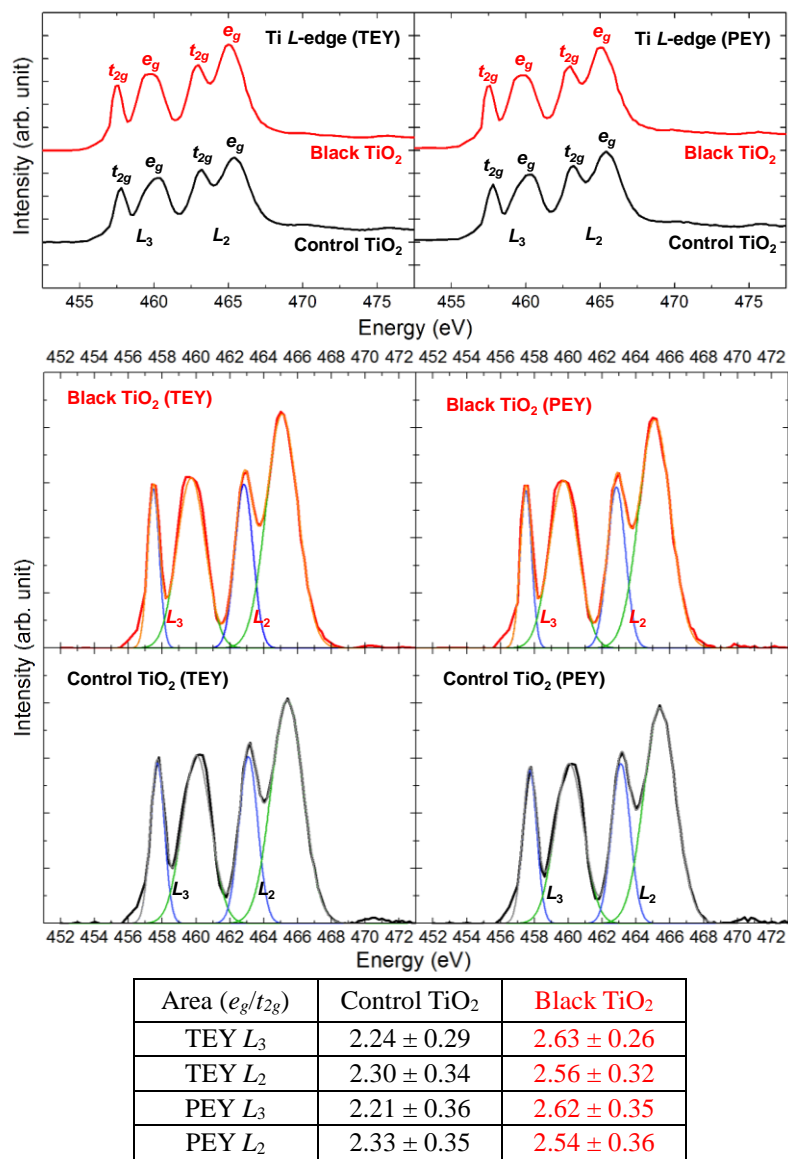


Fig. 3-5. (Color) Ti *L*-edge soft x-ray absorption spectroscopy (sXAS). Total electron yield (TEY) and partial electron yield (PEY) spectra of black TiO<sub>2</sub> and control TiO<sub>2</sub> are displayed with fitted lines. The area ratios of fitted peaks for *e<sub>g</sub>* to *t<sub>2g</sub>* are also present in the table.

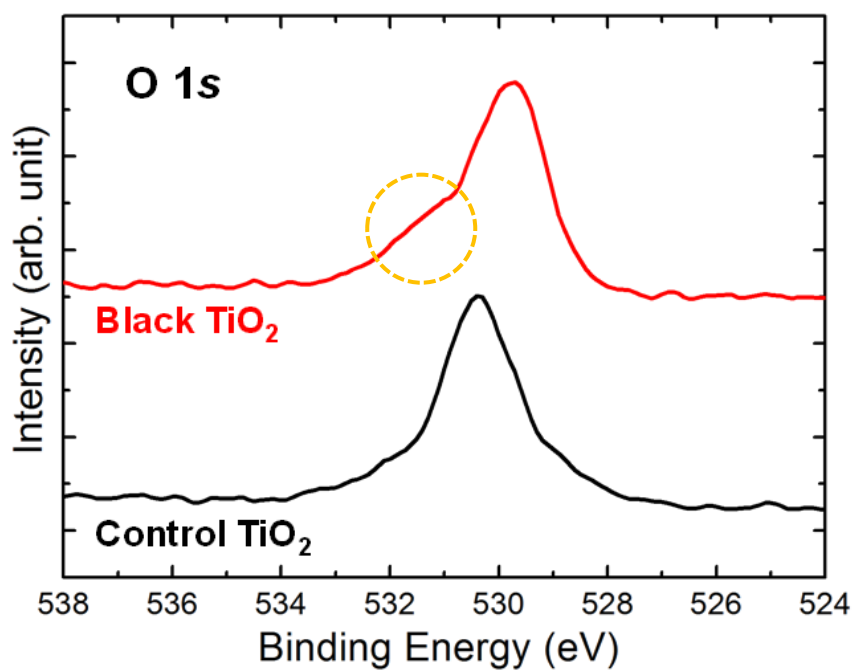


Fig. 3-6. (Color) XPS spectra in the O 1s region for the black TiO<sub>2</sub> and reference rutile TiO<sub>2</sub>. A shoulder peak of the black TiO<sub>2</sub> (marked by a circle) corresponds to the OH species, indicating that the relatively larger amount of OH species are incorporated to the black TiO<sub>2</sub> surface than that of control TiO<sub>2</sub>.

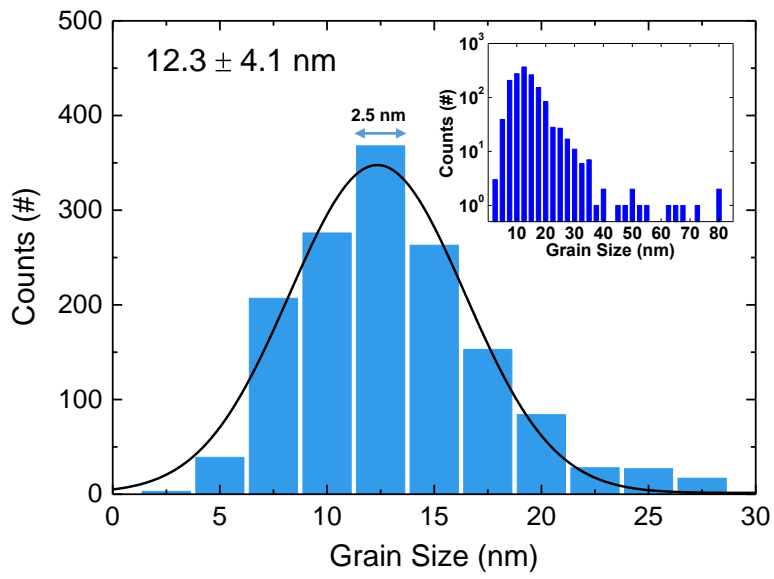
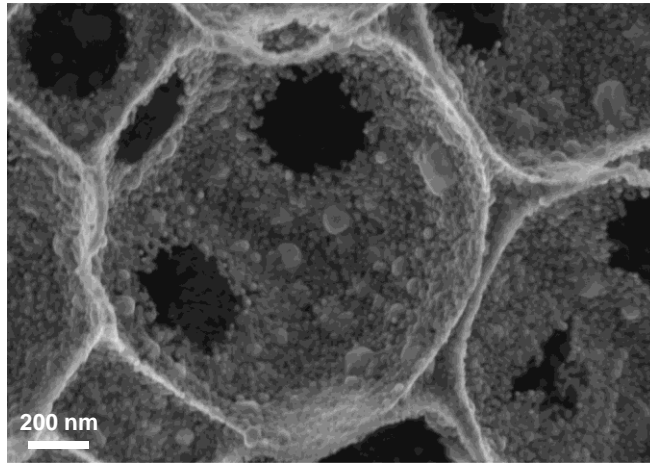


Fig. 3-7. (Color) Size distribution of  $\text{TiO}_2$  grains in HOP-*b*TiO<sub>2</sub>.



Fig. 3-8. (Color) Pellets of  $\text{TiO}_2$  and black  $\text{TiO}_2$  for the measurement of 4-point probe.

### 3.3.2. Electrochemical properties of HOP-*b*TiO<sub>2</sub> electrode

The electrochemical performances of hierarchically-ordered porous black TiO<sub>2</sub> (HOP-*b*TiO<sub>2</sub>) as a Li-O<sub>2</sub> cathode are assessed in Fig. 3-9. The first discharge curve (Fig. 3-9(a)) is observed within the range of 2.2 V - 4.5 V at 0.05 mA cm<sup>-2</sup>, and shows a high capacity of ~7500 mAh g<sup>-1</sup> by virtue of enhanced electronic conductivity as well as the low mass of TiO<sub>2</sub>. Compared to the relatively-small overpotential during discharge (with respect to the equilibrium potential of Li<sub>2</sub>O<sub>2</sub> formation/decomposition, 2.96 V vs. Li/Li<sup>+</sup>), large overpotential is observed during the charge process, indicative of the sluggish kinetics of Li<sub>2</sub>O<sub>2</sub> decomposition. Typical voltage profiles with the capacity limited to 1000 mAh g<sup>-1</sup> are presented in Fig. 3-9(b) (1st and 260th cycle). Decrease in terminal charging potentials (~4.0 V) are observed, compared to the fully-charged state in Fig. 3-9(a) (~4.5 V), which is attributed to the limited capacity by which electrolyte decomposition can be alleviated. The cyclability and terminal voltage of the HOP-*b*TiO<sub>2</sub> with the capacity limited to 1000 mAh g<sup>-1</sup> are summarized in Fig. 3-9(c). Despite the abrupt increase in cell polarization and decay of capacity from the last few cycles, the carbon-free HOP-*b*TiO<sub>2</sub> can operate for ~260 cycles without premature cell death. Such an abrupt increase in polarization and deterioration of cell performance may come from electrolyte decomposition or possibly from the degradation of the other cell components.

The origin of enhanced electrochemical properties of HOP-*b*TiO<sub>2</sub> electrode was identified with collected *ex-situ* SEM images. Figure 3-9(d) is taken after discharged to 1000 mAh g<sup>-1</sup>, and shows that the discharge product, Li<sub>2</sub>O<sub>2</sub>, is formed in toroidal shape with a diameter of ~300 nm. Therefore, it is highly likely that such toroidal Li<sub>2</sub>O<sub>2</sub> is a

result of solution-mediated growth, as opposed to the  $\text{Li}_2\text{O}_2$  film that, otherwise, is limited to only a few nanometers [7,35]. It is known that ether-based electrolytes lead to both solution/surface  $\text{Li}_2\text{O}_2$  growth, depending on the discharge potential (overpotential), electrode material, and additives.

Interestingly, the toroid-shaped  $\text{Li}_2\text{O}_2$  particles are suspended on the wall of mesoporous  $\text{TiO}_2$  framework. At fully discharged state (Fig. 3-9(e)), all of the  $\text{TiO}_2$  arrays are covered uniformly by the  $\text{Li}_2\text{O}_2$  particles, and the thickness of the ordered macro-walls increases to the size of individual toroid ( $\sim 300$  nm) as seen in Fig. 3-9(d), compared to the pristine electrode with wall size of several tens of nanometers (Fig. 3-4(b)). The morphologies of discharged electrode are also represented in SEM images of Fig. 3-10 and in TEM images of Fig. 3-11. As a result,  $\text{Li}_2\text{O}_2$  toroid are regularly stacked on the  $\text{TiO}_2$  particles guided by highly-ordered architecture, as the scheme of Fig. 3-9(g). The stacked toroidal  $\text{Li}_2\text{O}_2$  particles are also confirmed by a STEM image at the fully-discharged state, as seen in Fig. 3-9(h). The images of fully-charged state clearly exhibits that the electrode recovers its pristine morphology (Fig. 3-9(f)), and diffusion channels are maintained during cycling. It can be said that the  $\text{Li}_2\text{O}_2$  particles can efficiently be grown from solvent, and high specific capacity ( $\sim 7500$  mAh  $\text{g}^{-1}$ ) is the result of the efficient utilization of the electrode materials.

By virtue of regular empty space separated by 1  $\mu\text{m}$ , solvated lithium ions and oxygen molecules can be effectively transported into deep inside of electrode without it being clogged, rendering all the black  $\text{TiO}_2$  materials to be utilized during cell operation. We believe that these observations are distinguishable from those of conventional

nanoparticle-based electrodes where the  $\text{Li}_2\text{O}_2$  particles are formed at the interspace or surface of aggregated nanoparticles, in a disordered manner [34,35]. Since the spaces between nanoparticles are irregular, and insufficient for the accommodation of large toroid, full-utilization of the possible discharge capacity from solvent-mediated growth can hardly be achieved. However, our HOP- $b\text{TiO}_2$  electrode deliberately includes large and regular empty spaces so that large size of  $\text{Li}_2\text{O}_2$  particles can be afforded without being restricted from inter-particle spaces, and is reflected as high specific capacity of HOP- $b\text{TiO}_2$  electrode.

These morphological features, along with the carbon-free composition, also assure the high cyclability of HOP- $b\text{TiO}_2$  electrode. As confirmed from SEM images in Figs. 3-9(d) and (e), the diffusion channels and empty spaces are maintained after the formation of discharge products (~300 nm), and the electrode sustains the open structures even when the hardly removable side products, e.g.  $\text{Li}_2\text{CO}_3$  are formed from electrolyte decomposition [17-20]. SEM image and XPS spectra after cell decay (Fig. 3-12) demonstrate that the open structure are maintained even when side products cover all the electrode surface, and leads to electrode passivation. Although electrolyte decomposition occurring at interface between electrolyte and  $\text{Li}_2\text{O}_2$  are adequately alleviated on carbon-free electrode, it still degrades the electrode stability during repeated cycles, and therefore, the HOP- $b\text{TiO}_2$  with the unique architecture is superior to the conventional electrode. In other words, HOP- $b\text{TiO}_2$  not only has advantages in the diffusion kinetics and utilization of electrode, but also is less susceptible to the side reaction by the retention of breathable open structures during cycles.

Although the HOP-*b*TiO<sub>2</sub> is beneficial for the formation of discharge product (Li<sub>2</sub>O<sub>2</sub>), diffusion kinetics, and electrode stability, this architecture might be unfavorable for the decomposition of Li<sub>2</sub>O<sub>2</sub> due to its toroidal morphology. Namely, the Li<sub>2</sub>O<sub>2</sub> toroid that encloses the HOP-*b*TiO<sub>2</sub> electrode has limited interface only at the points of contact, the rest of which are exposed to the liquid electrolyte. While conventional nanoparticle-based electrodes include conductive additives (e. g. carbon black) in the vicinity of insulating Li<sub>2</sub>O<sub>2</sub> particles to accept electrons upon charging, electron extraction from the Li<sub>2</sub>O<sub>2</sub> to HOP-*b*TiO<sub>2</sub> is challenged by the limited interface between them. Relatively-large overpotential on charge (Fig. 3-9(a)), compared to previous literatures on Ti-based nanoparticles (TiC, Ti<sub>4</sub>O<sub>7</sub>) with TiO<sub>2</sub> surface that have similar discharge potentials, could originate from this different morphological features by which the electron path is confined to one direction. It should be noted that, however, vast majority of Li<sub>2</sub>O<sub>2</sub> toroid on HOP-*b*TiO<sub>2</sub> is directly exposed to the electrolyte, which provides a suitable environment for use of soluble catalysts.

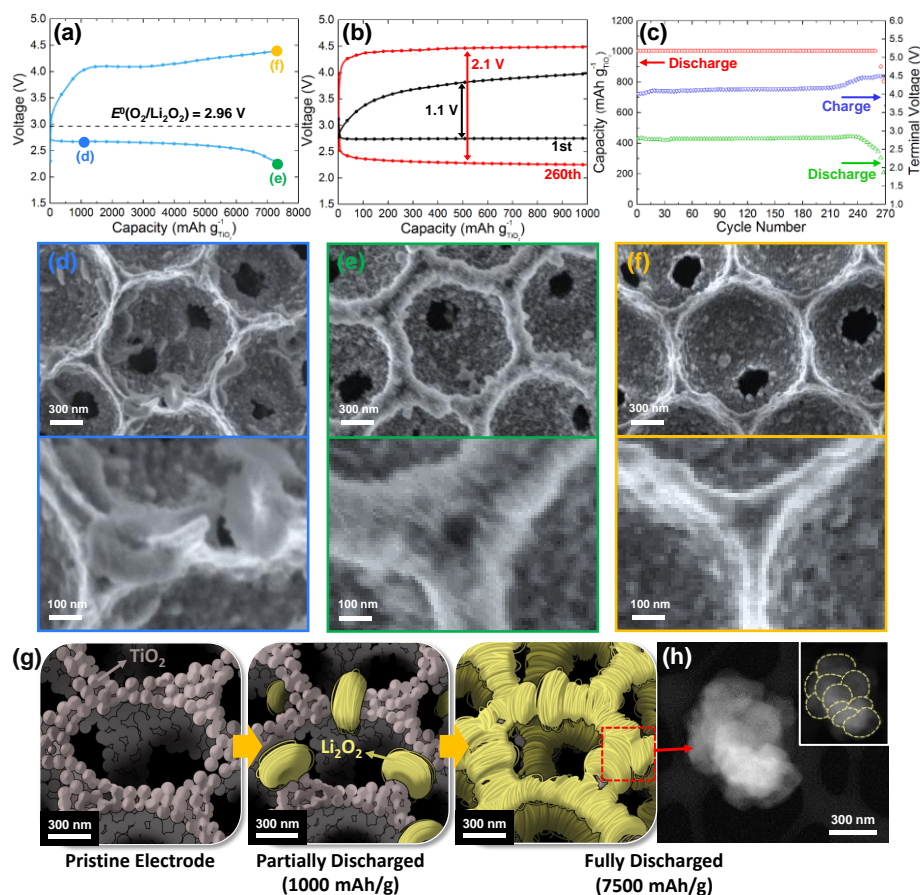


Fig. 3-9. (Color) (a) Discharge/charge profiles of the HOP-*b*TiO<sub>2</sub> electrode at a rate of 0.05 mA cm<sup>-2</sup>. (b) Discharge/charge profiles of HOP-*b*TiO<sub>2</sub> at a rate of 0.05 mA cm<sup>-2</sup>, with the specific capacity limited to 1000 mAh g<sup>-1</sup>. (c) Cyclability and terminal voltages of the HOP-*b*TiO<sub>2</sub>. (d) SEM images of the HOP-*b*TiO<sub>2</sub> electrode after first discharge to 1000 mAh g<sup>-1</sup>, (e) after fully discharged, and (f) after recharged. Marked by solid circles (d-e) are correspondent states in the voltage profiles in Fig. 3(a). (g) Schematic representations of growing tendency of Li<sub>2</sub>O<sub>2</sub> that is guided by the ordered electrode architecture. (h) STEM image of the stacked Li<sub>2</sub>O<sub>2</sub> toroids in a fully-discharged state.

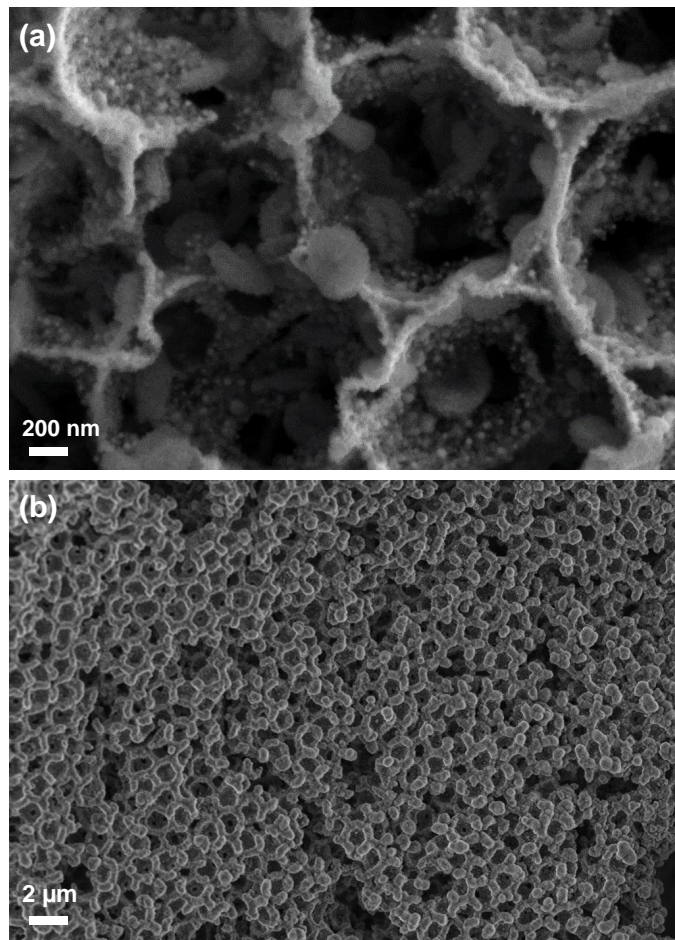


Fig. 3-10. SEM images of the HOP-*b*TiO<sub>2</sub> (a) at a discharged state to 1000 mAh g<sup>-1</sup> and (b) at fully discharged state.

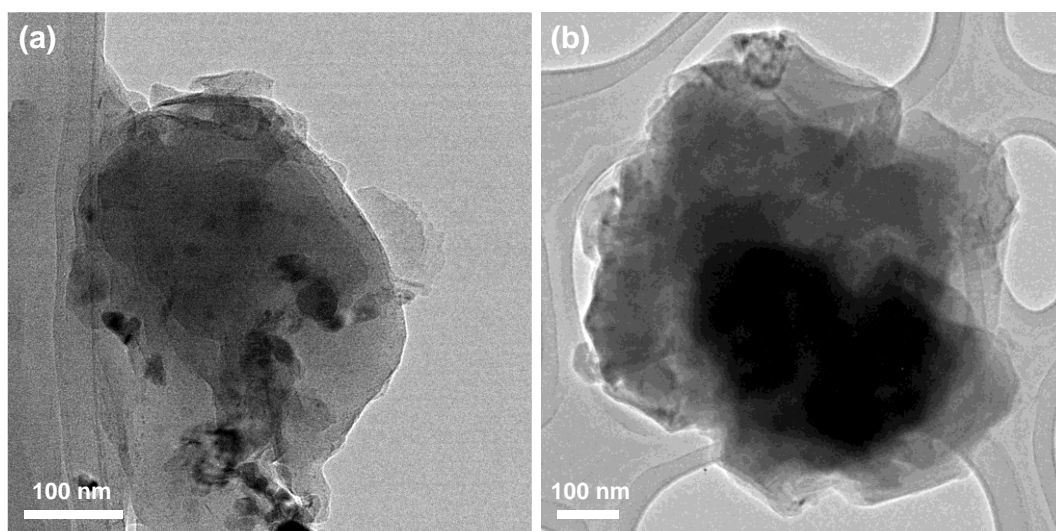


Fig. 3-11. TEM images for the HOP-*b*TiO<sub>2</sub> electrode with the discharge product (a) at a discharged state to 1000 mAh g<sup>-1</sup> and (b) at fully discharged state.

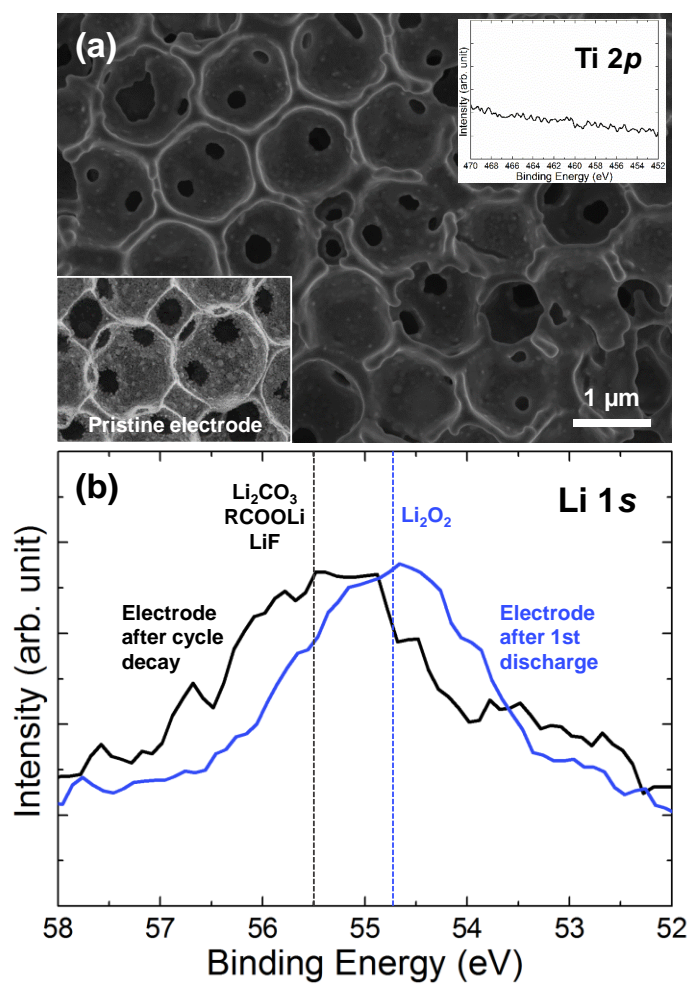


Fig. 3-12. (Color) (a) SEM image and (b) XPS spectra in the Li 1s region of HOP-*b*TiO<sub>2</sub> electrode after cell death.

### 3.3.3. Combination of electrode architecture and redox mediator

Since the architecture of HOP-*b*TiO<sub>2</sub> electrode provokes the use of soluble catalysts for the decomposition of Li<sub>2</sub>O<sub>2</sub>, lithium iodide (LiI), as a redox mediator (RM), is introduced to our electrolyte. LiI is known to have various oxidation voltages, depending on the type of electrolyte solvent and electrode surface/morphology [51]. As shown in voltage profiles in Fig. 3-13(a), charging potential is dramatically decreased by the incorporation of LiI, compared to the electrode without redox mediator, resulting in very small polarization of ~0.37 V. Also, this charge potential is relatively low, and kept constant to the capacity of 1000 mAh g<sup>-1</sup>. As shown in Fig. 3-13(b), the polarization increases from the 1st to 340th cycle (0.37 V to 0.95 V at 500 mAh g<sup>-1</sup>) during cycles with 0.05 mA cm<sup>-2</sup> applied to the cell. However, it should be noted that the polarization is still less than 1 V, and is even lower than that of the 1st cycle of HOP-*b*TiO<sub>2</sub> without LiI (1.1 V at 500 mAh g<sup>-1</sup>).

Though the application of the LiI catalyst to nanoporous black TiO<sub>2</sub> electrode also improves the charging potential (Fig. 3-14), the degree of enhancement in HOP-*b*TiO<sub>2</sub> is more notable. The unique architecture of HOP-*b*TiO<sub>2</sub> is clearly beneficial as to application of LiI for Li<sub>2</sub>O<sub>2</sub> decomposition, which may be attributed to the enhanced catalyst transport through the connected diffusion channels (Fig. 3-4(e)) and large interface between Li<sub>2</sub>O<sub>2</sub> and electrolyte. Since the breathable open structure is robust even at the full-discharged state (Fig. 3-9(e)), and still provides diffusion channels, LiI as a redox mediator can effectively be transported to deep inside of electrode during charge. A conceptual scheme is represented in Fig. 3-13(c) for better understanding. With decreased charging potential, the HOP-*b*TiO<sub>2</sub> electrode shows extremely-high stability up to ~350

cycles (Fig. 3-13(d)), indicative of a synergistic effect of electrode architecture and soluble catalysts. Since electrochemical decomposition of oxygen-dissolved TEGDME dramatically occurs from ~4.3 V [53], the extremely-high stability of HOP-*b*TiO<sub>2</sub> with LiI is resulted from this decreased charging potential (less than 4 V for 340 cycles), while the HOP-*b*TiO<sub>2</sub> without LiI rapidly decays after ~230th cycle with its charging potential reaching the voltage range of TEGDME decomposition (~4.3 V).

It is generally reported that charging process of Li-O<sub>2</sub> battery with a redox mediator proceeds through two steps [37,39,51]. In the first step, RM is electrochemically oxidized to RM<sup>+</sup> on the cathode, in our case, on mesoporous TiO<sub>2</sub> surface. In the following second step, oxidized RM<sup>+</sup> ions react chemically with Li<sub>2</sub>O<sub>2</sub> particles. As mentioned earlier, in our ordered electrode architecture, Li<sub>2</sub>O<sub>2</sub> toroid is guided to grow and enclose the regularly-separated TiO<sub>2</sub> nanoparticles, with a vast majority of Li<sub>2</sub>O<sub>2</sub> surface exposed to electrolyte without possible impediment from TiO<sub>2</sub> nanoparticle arrays or pore walls (Fig. 3-9(d)). Therefore, the unique morphology of HOP-*b*TiO<sub>2</sub> along with the growing aspect of Li<sub>2</sub>O<sub>2</sub> is featured by large reactive interface between Li<sub>2</sub>O<sub>2</sub> and RM<sup>+</sup> dissolved in electrolyte, as well as the effective transport of RM<sup>+</sup> molecules to the Li<sub>2</sub>O<sub>2</sub> surface, which contributes to small polarization over 300 cycles (Fig. 3-13(d)).

Despite intensive studies on generating huge Li<sub>2</sub>O<sub>2</sub> toroidal particles through solvent-mediated growth [34-36], decomposition of such large particles still has been challenging. As for reversible decomposition of such large Li<sub>2</sub>O<sub>2</sub>, our study combines soluble catalysts with the properly-designed architecture, as a result of which provides two types of interfaces for RM to function. First, the large mesoporous surface (interface 1) of HOP-*b*TiO<sub>2</sub> is associated with electrochemical reaction sites for the oxidation of redox

mediators ( $\text{RM} \rightarrow \text{RM}^+ + \text{e}^-$ ). Secondly, the  $\text{Li}_2\text{O}_2$  surface is structurally-induced to have large exposure to  $\text{RM}^+$ , and the interface between them (interface 2) is related to the chemical decomposition of  $\text{Li}_2\text{O}_2$  by  $\text{RM}^+$ . We believe that the enlargement of these two types of interfaces, as featured by our HOP-*b* $\text{TiO}_2$ , can be a key to the design of advanced air cathode, especially for electrodes utilizing solvent-mediated growth.

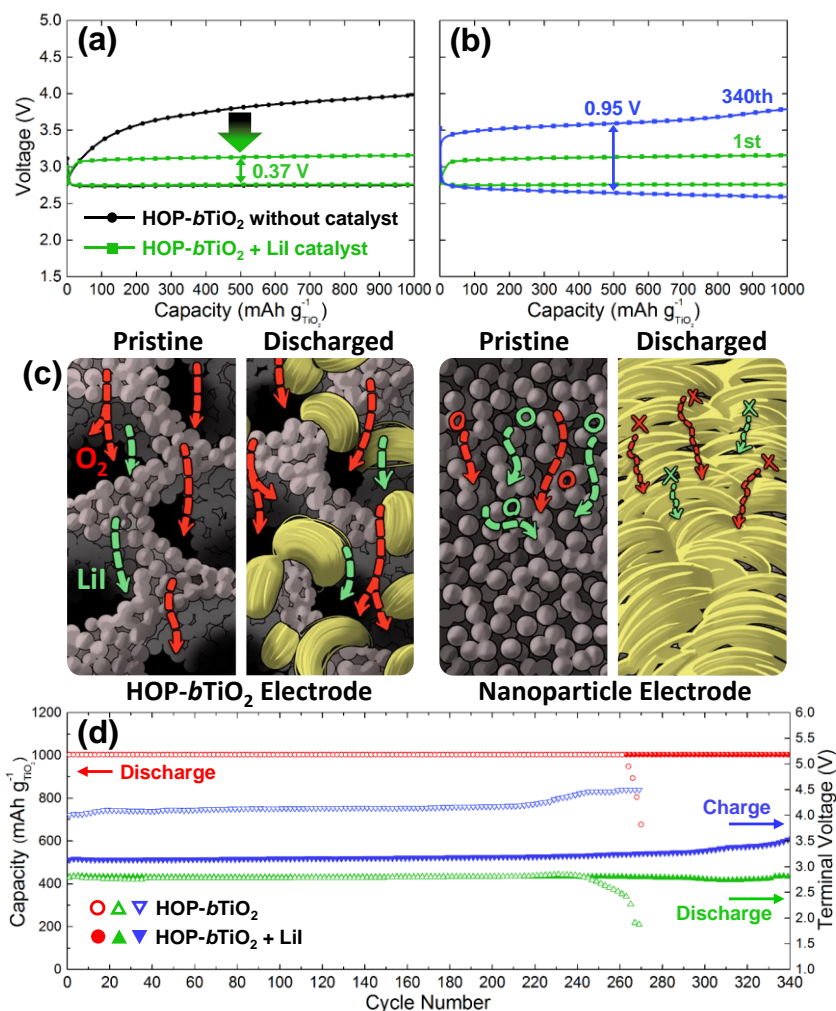


Fig. 3-13. (Color) (a) First discharge/charge profiles of the HOP-*b*TiO<sub>2</sub> with and without LiI catalyst. (b) Selected voltage profiles of the HOP-*b*TiO<sub>2</sub> with LiI catalyst (1st and 340th cycle). (c) Schemes representing the effect of electrode architecture (HOP-*b*TiO<sub>2</sub> and nanoparticle electrode) on the activity of a redox mediator. (d) Cyclability and terminal voltages of the HOP-*b*TiO<sub>2</sub> with and without LiI catalyst. All of the electrodes are discharged and charged at a rate of 0.05 mA cm<sup>-2</sup>, with the specific capacity limited to 1000 mAh g<sup>-1</sup>.

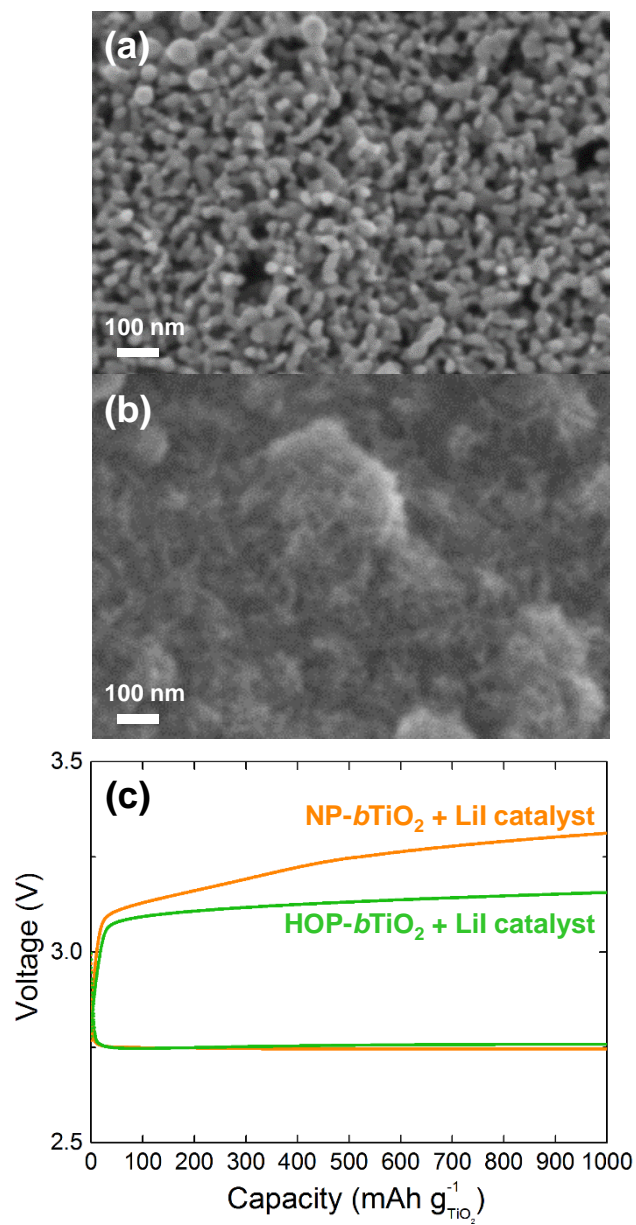


Fig. 3-14. (Color) SEM images of (a) the pristine nanoporous black TiO<sub>2</sub> (NP-*b*TiO<sub>2</sub>) and (b) after discharge to 1000 mAh g<sup>-1</sup>. (c) Voltage profiles showing the effect of electrode architecture on the activity of LiI catalyst (HOP-*b*TiO<sub>2</sub> and NP-*b*TiO<sub>2</sub>).

### 3.3.4. Origin of high stability of black TiO<sub>2</sub> electrodes

Although rapid increase of polarization was observed in HOP-*b*TiO<sub>2</sub> from the last few cycles, both terminal discharge and charge potentials (at 1000 mAh g<sup>-1</sup>) are not significantly changed up to ~230th cycle (Fig. 3-9(c)). Considering that the abrupt decay originates mainly from the electrolyte decomposition (Fig. 3-12), this relatively-constant polarization implies that electrode material itself is stable during battery operation. Photographs of the pristine HOP-*b*TiO<sub>2</sub> and cycled HOP-*b*TiO<sub>2</sub> (Fig. 3-15) reveal that the black color, indicative of modified electronic structure, is retained in both electrodes. Meanwhile, x-ray photoelectron spectroscopy (XPS) analysis of Ti 2*p* regions shows slight peak shift to higher binding energy after discharge (Fig. 3-16(a)), while that of Li 1*s* region clearly shows the formation of Li<sub>2</sub>O<sub>2</sub> (Fig. 3-16(b)). We believe that the Li<sub>2</sub>O<sub>2</sub>, in contact with the TiO<sub>2-x</sub> surface, might have induced the slight oxidation. Nonetheless, it is quite surprising that further shift or oxidation is not observed in Ti 2*p* region after subsequent charges, in spite of rather high potential (~4 V) at which the TiO<sub>2-x</sub> is prone to be oxidized to TiO<sub>2</sub>. The observed stability can be associated with the amorphous shell around crystalline core, as often reported in the case of black TiO<sub>2</sub> [52-54].

Likewise, the outermost layer of our HOP-*b*TiO<sub>2</sub> consists of disordered shell of ~1 nm, with crystalline phase present as the core (Fig. 3-16(c)). Such disordered shell is generated during the H<sub>2</sub> reduction, which is proved by extending the reduction time, as seen in Fig. 3-17. In the TEM images, TiO<sub>2</sub> nanocrystals displays relatively-clean surfaces before the hydrogenation, while that of hydrogenated TiO<sub>2</sub> becomes thicker with increasing reduction time. In the case of H<sub>2</sub>-reduction time for 40 h, the amorphous domains grow

to be ~5 nm in thickness.

As seen in the TEM images after discharge (Fig. 3-16(d)), a thick layer is observed around the crystalline core, where the layer consists of the discharge product  $\text{Li}_2\text{O}_2$  and the disordered shell that are quite undistinguishable. This disordered shell seems to react with the oxygen species created during discharge, and therefore, the outermost disordered shell in close proximity with  $\text{Li}_2\text{O}_2$  could have changed into stoichiometric  $\text{TiO}_2$ , as confirmed from the shift of XPS spectra. The surface  $\text{TiO}_2$  was also observed in TiC [19,27,28] and  $\text{Ti}_4\text{O}_7$  [26] after 1st discharge by XPS spectra in Ti region, and remained relatively constant after repeated cycles, without severe bulk oxidation. A. Naldoni *et al.* claimed that highly disordered and reactive phase of black  $\text{TiO}_2$  surface becomes nearly stoichiometric  $\text{TiO}_2$  upon exposed to air, and preserves bulk defect from further oxidation [52]. In a similar way, the slightly-oxidized shell could play an important role in our HOP-*b* $\text{TiO}_2$  retaining its black  $\text{TiO}_2$  characteristics. As a proof, the pristine HOP-*b* $\text{TiO}_2$  electrode shows no color changes when exposed to air for ~1 year (our empirical observation). Although slight oxidation occurs on the surface of HOP-*b* $\text{TiO}_2$  during discharge, this oxidized layer can prevent the remaining  $\text{Ti}^{3+}$  ions from oxidation, as reflected in high cyclability of HOP-*b* $\text{TiO}_2$  electrode. Meanwhile, the thick layer is taken away in the image of charged  $\text{TiO}_2$  (Fig. 3-16(e)), similar to the pristine  $\text{TiO}_2$  (Fig. 3-16(c)).

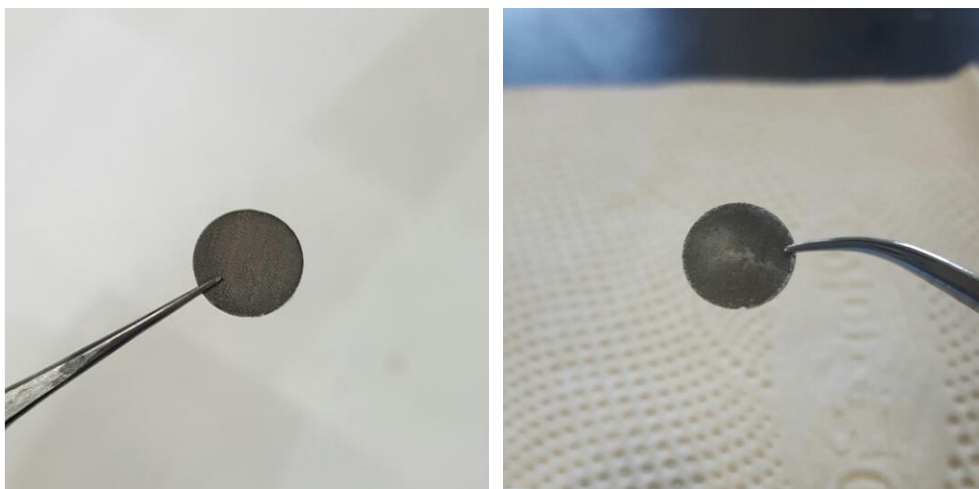


Fig. 3-15. (Color) Photographs of the pristine HOP- $b\text{TiO}_2$  electrode and cycled HOP- $b\text{TiO}_2$  electrode after cell death. The retained black color even after long cycles is indicative of the preserved  $\text{Ti}^{3+}$  ions and oxygen vacancies in the crystal structure.

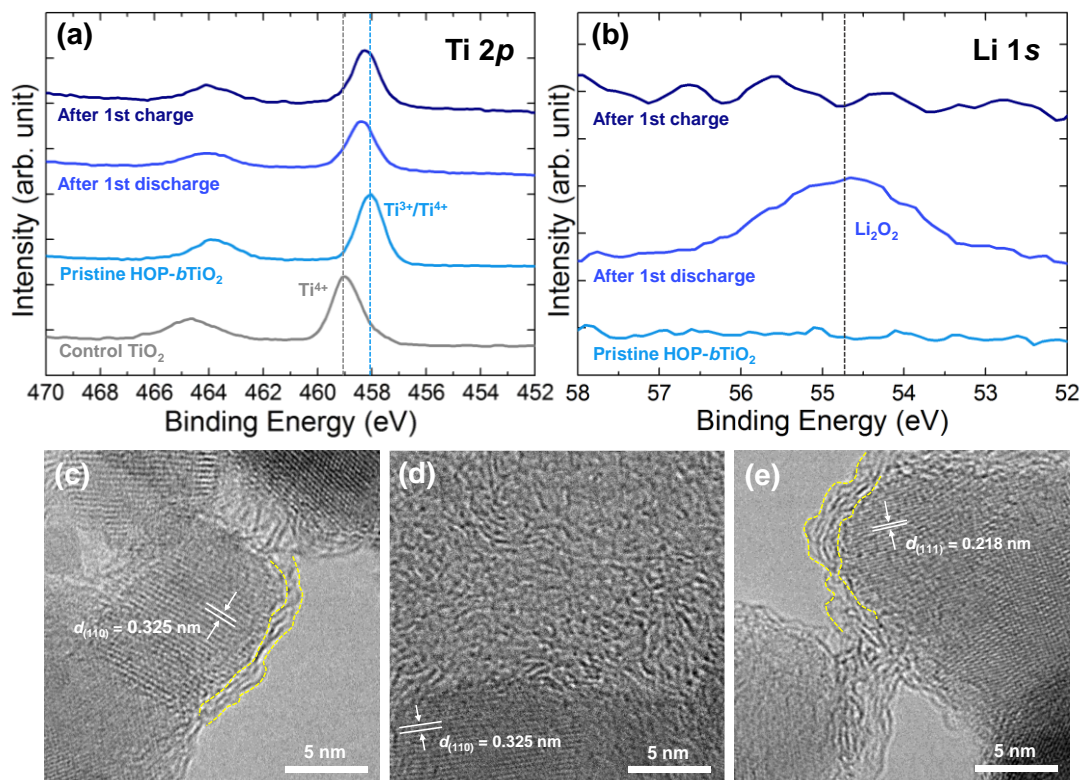


Fig. 3-16. (Color) XPS spectra in the (a) Ti 2*p* and (b) Li 1*s* region for the HOP-*b*TiO<sub>2</sub> at pristine, discharged (1000 mAh g<sup>-1</sup>), and recharged states. TEM images of the HOP-*b*TiO<sub>2</sub> electrode at different states that are correspondent with the XPS spectra: (c) pristine, (d) discharged, and (e) recharged state.

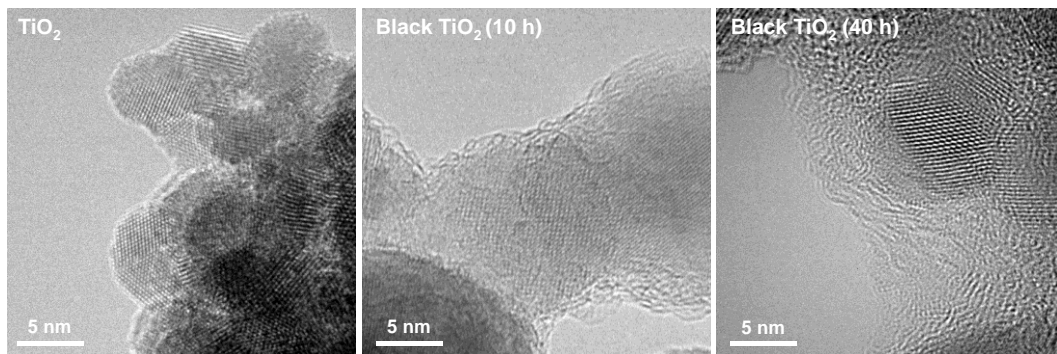


Fig. 3-17. TEM images of the black TiO<sub>2</sub> with various H<sub>2</sub>-treatment time of 0 h, 10 h, and 40 h. As H<sub>2</sub>-annealing time increases, amorphous surface layers become thicker.

In an earlier work of black TiO<sub>2</sub>, G. Duscher *et al.* identified chemical composition of the shell to be amorphous Ti<sub>2</sub>O<sub>3</sub> in which a typical TiO<sub>6</sub> octahedron is distorted with Ti interstitial diffusion [55]. However, the Ti 2*p*<sub>3/2</sub> binding energy of Ti<sub>2</sub>O<sub>3</sub> is ~458 eV, which is not well matched with our Ti 2*p* XPS results. Indeed, it is still controversial that how and why the oxygen-deficient TiO<sub>2</sub> is stable in either air-exposed or electrochemically-charged state, despite of various applications of black TiO<sub>2</sub> to photocatalysis, fuel cells, Li-ion batteries, etc. In our case, we conclude that amorphous layer oxidized during the first discharge guarantee the high stability of black TiO<sub>2</sub> during extended cycles.

The importance of protecting layers in titanium-based materials are already dealt with by a number of studies, including TiC and Ti<sub>4</sub>O<sub>7</sub>, as mentioned earlier. Anyhow, our results highlight again that the materials even vulnerable to the oxygen or high voltage can be used as air cathodes with presence of protective layers. The detailed mechanism of interplay between electrode surface and discharge products, and its role in the electrode stability needs to be further understood to develop an advanced Ti-based cathode for stable Li-O<sub>2</sub> batteries. A suggested mechanism regarding the high efficiency and stability of HOP-*b*TiO<sub>2</sub> is illustrated in Fig. 3-18.

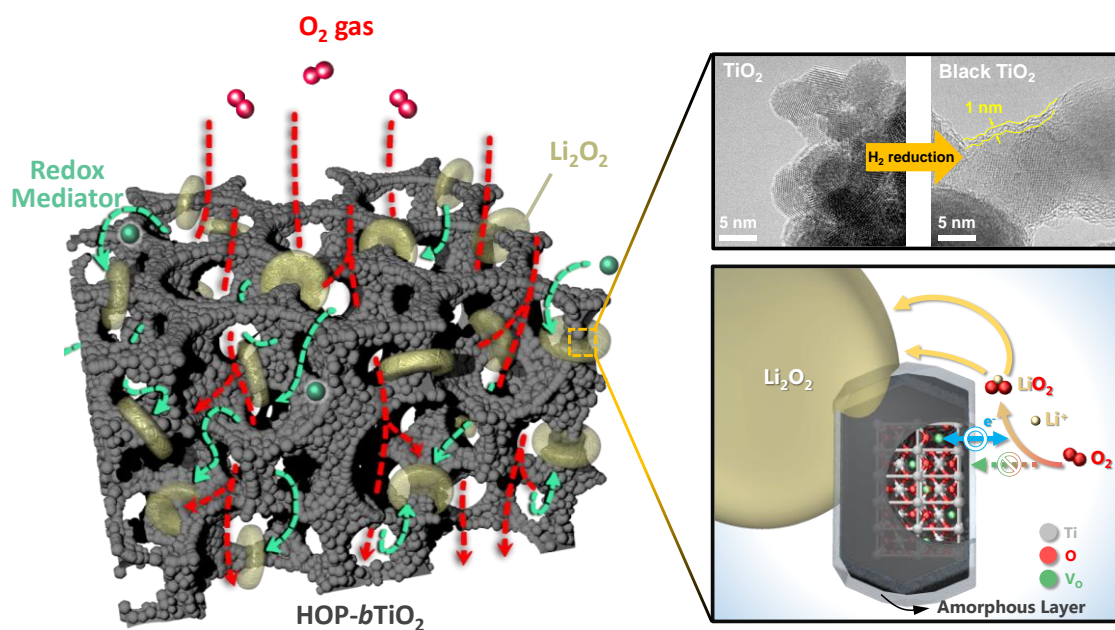


Fig. 3-18. (Color) A schematic representation with TEM images summarizing functions of the HOP-*b*TiO<sub>2</sub> electrode.

### 3.4. Conclusions

Our strategy to design a highly-stable and efficient air cathode for Li-O<sub>2</sub> batteries was to adopt oxygen-deficient TiO<sub>2</sub> loaded on Ni mesh, as a carbon- and binder-free electrode. Tailoring the off-stoichiometry of oxygen and inverse-opal structure from the PS templates helped enhance the electronic conductivity, and rendered the architecture of electrode to be favorable for reversible formation/decomposition of Li<sub>2</sub>O<sub>2</sub>, respectively. From the electrode architecture, the Li<sub>2</sub>O<sub>2</sub> grew in a toroidal shape, and was suspended on the HOP-*b*TiO<sub>2</sub> framework, being separated by the dimension of the macropores (~1 μm). The growing tendency of the Li<sub>2</sub>O<sub>2</sub> provoked the use of the soluble catalyst, and the HOP-*b*TiO<sub>2</sub> electrode with LiI showed extremely-high stability up to ~350th cycle at a current density of 0.05 mA cm<sup>-2</sup>. The high performance of HOP-*b*TiO<sub>2</sub> electrode is attributed to the large exposed surface of Li<sub>2</sub>O<sub>2</sub> to the electrolyte and enhanced mass transport of soluble catalyst to the Li<sub>2</sub>O<sub>2</sub> surfaces through diffusion channels of small tortuosity. The breathable carbon-free electrode with soluble catalysts was found to be effective for the reversible formation/decomposition of large toroidal Li<sub>2</sub>O<sub>2</sub> grown by solution mechanism. Disordered shell observed on the crystalline surfaces contributed to the stability of TiO<sub>2-x</sub> electrode even in an oxidative environment under high-charging potential, highlighting the importance of protection layer on the stability of titanium-based electrodes. Since TiO<sub>2</sub> materials have price competitiveness, low mass, and, above all, potentials for its materials properties to be varied with ease, we believe that the HOP-*b*TiO<sub>2</sub> electrode can be a promising alternative to carbon electrode in Li-O<sub>2</sub> batteries.

### 3.5. References

1. Tarascon, J.-M. Key challenges in future Li-battery research. *Phil. Trans. R. Soc. A* **2010**, *368*, 3227-3241.
2. Whittingham, M. S. Materials Challenges Facing Electrical Energy Storage. *MRS Bull.* **2008**, *33*, 411-419.
3. Goodenough, J. B.; Park, K.-S. The Li-Ion Rechargeable Battery: A Perspective. *J. Am. Chem. Soc.* **2013**, *135*, 1167-1176.
4. Feng, N.; He, P.; Zhou, H.; Critical Challenges in Rechargeable Aprotic Li-O<sub>2</sub> Batteries. *Adv. Energy Mater.* **2016**, *6*, 1502303 (1-24).
5. Shao, Y.; Ding, F.; Xiao, J.; Zhang, J.; Xu, W.; Park, S.; Zhang, J.-G.; Wang, Y.; Liu, J. Making Li-Air Batteries Rechargeable: Material Challenges. *Adv. Funct. Mater.* **2013**, *23*, 987-1004.
6. Girishkumar, G.; McCloskey, B.; Luntz, A. C.; Swanson, S.; Wilcke, W. Lithium-Air Battery: Promise and Challenges. *J. Phys. Chem. Lett.* **2010**, *1*, 2193-2203.
7. Aurbach, D.; McCloskey, B. D. Nazar, L. F.; Bruce, P. G. Advances in Understanding Mechanisms Underpinning Lithium–Air Batteries. *Nat. Energy* **2016**, *1*, 16128 (1-11).
8. Bruce, P. G.; Freunberger, S. A.; Hardwick, L. J.; Tarascon, J.-M. Li-O<sub>2</sub> and Li-S Batteries with High Energy Storage. *Nat. Mater.* **2012**, *11*, 19-29.
9. Lu, J.; Li, L.; Park, J.-B.; Sun, Y.-K.; Wu, F.; Amine, K. Aprotic and Aqueous Li-O<sub>2</sub> Batteries. *Chem. Rev.* **2014**, *114*, 5611-5640.
10. Li, Y.; Wang, J.; Li, X.; Liu, J.; Geng, D.; Yang, J.; Li, R.; Sun, X. Nitrogen-Doped Carbon Nanotubes as Cathode for Lithium-Air Batteries. *Electrochem. Commun.* **2011**, *13*, 668-672.
11. Xiao, J.; Mei, D.; Li, X.; Xu, W.; Wang, D.; Graff, G. L.; Bennett, W. D.; Nie, Z.; Saraf, L. V.; Aksay, I. A.; Liu, J.; Zhang, J.-G. Hierarchically Porous Graphene as a Lithium-Air Battery Electrode. *Nano Lett.* **2011**, *11*, 5071-5078.

12. Sun, B.; Huang, X.; Chen, S.; Munroe, P.; Wang, G. Porous Graphene Nanoarchitectures: An Efficient Catalyst for Low Charge-Overpotential, Long Life, and High Capacity Lithium-Oxygen Batteries. *Nano Lett.* **2014**, *14*, 3145-3152.
13. Guo, Z.; Zhou, D.; Dong, X. L.; Qiu, Z.; Wang, Y.; Xia, Y. Ordered Hierarchical Mesoporous/Macroporous Carbon: A High-Performance Catalyst for Rechargeable Li-O<sub>2</sub> Batteries. *Adv. Mater.* **2013**, *25*, 5668-5672.
14. Xie, J.; Yao, X.; Cheng, Q.; Madden, I. P.; Dornath, P.; Chang, C.-C.; Fan, W.; Wang, D.; Three Dimensionally Ordered Mesoporous Carbon as a Stable, High-Performance Li-O<sub>2</sub> Battery Cathode. *Angew. Chem., Int. Ed.* **2015**, *54*, 4299-4303.
15. Lim, H.-D.; Park, K.-Y.; Song, H.; Jang, E. Y.; Gwon, H.; Kim, J.; Kim, Y. H.; Lima, M. D.; Robles, R. O.; Lepró, X.; Baughman, R. H.; Kang, K. Enhanced Power and Rechargeability of a Li-O<sub>2</sub> Battery Based on a Hierarchical-Fibril CNT Electrode. *Adv. Mater.* **2013**, *25*, 1348-1352.
16. Thotiyl, M. M. O.; Freunberger, S. A.; Peng, Z.; Bruce, P. G. Recent Development of Non-Platinum Catalysts for Oxygen Reduction Reaction. *J. Am. Chem. Soc.* **2013**, *135*, 494-500.
17. McCloskey, B. D.; Speidel, A.; Scheffler, R.; Miller, D. C.; Viswanathan, V.; Hummelshøj, J. S.; Nørskov, J. K.; Luntz, A. C. Twin Problems of Interfacial Carbonate Formation in Nonaqueous Li-O<sub>2</sub> Batteries. *J. Phys. Chem. Lett.* **2012**, *3*, 997-1001.
18. Gallant, B. M.; Mitchell, R. R.; Kwabi, D. G.; Zhou, J.; Zuin, L.; Thompson, C. V.; Shao-Horn, Y. Chemical and Morphological Changes of Li-O<sub>2</sub> Battery Electrodes upon Cycling. *J. Phys. Chem. C* **2012**, *116*, 20800-20805.
19. Thotiyl, M. M. O.; Freunberger, S. A.; Peng, Z.; Chen, Y.; Liu, Z.; Bruce, P. G. A Stable Cathode for the Aprotic Li-O<sub>2</sub> Battery. *Nat. Mater.* **2013**, *12*, 1050-1056.
20. Peng, Z.; Freunberger, S. A.; Chen, Y.; Bruce, P. G. A Reversible and Higher-Rate Li-O<sub>2</sub> Battery. *Science* **2012**, *337*, 563-566.
21. Xie, J.; Yao, X.; Madden, I. P.; Jiang, D.-E.; Chou, L.-Y.; Tsung, C.-K.; Wang, D.

- Selective Deposition of Ru Nanoparticle on TiSi<sub>2</sub> Nanonet and Its Utilization for Li<sub>2</sub>O<sub>2</sub> Formation and Decomposition. *J. Am. Chem. Soc.* **2014**, *136*, 8903-8906.
22. Zhao, G.; Mo, R.; Wang, B.; Zhang, L.; Sun, K. Enhanced Cyclability of Li-O<sub>2</sub> Batteries Based on TiO<sub>2</sub> Supported Cathodes with No Carbon or Binder. *Chem. Mater.* **2014**, *26*, 2551-2556.
  23. Liu, Q.-C.; Xu, J.-J.; Xu, D.; Zhang, X.-B. Flexible Lithium-Oxygen Battery Based on a Recoverable Cathode. *Nat. Commun.* **2015**, *6*, 7892 (1-8).
  24. Lim, H.-D.; Seong, W. M.; Kim, J.; Lee, B.; Kim, D. H.; Kang, K. Nb-Doped TiO<sub>2</sub> Air-Electrode for Advanced Li-Air Batteries. *Journal of Asian Ceramic Societies* **2015**, *3*, 77-81.
  25. Chang, Y.; Dong, S.; Ju, Y.; Xiao, D.; Zhou, X.; Zhang, L.; Chen, X.; Shang, C.; Gu, L.; Peng, Z.; Cui, G. A Carbon- and Binder-Free Nanostructured Cathode for High-Performance Nonaqueous Li-O<sub>2</sub> Battery. *Adv. Sci.* **2015**, *2*, 1500092 (1-6).
  26. Kundu, D.; Black, R.; Berg, E. J.; Nazar, L. F. A Highly Active Nanostructured Metallic Oxide Cathode for Aprotic Li-O<sub>2</sub> Batteries. *Energy Environ. Sci.* **2015**, *8*, 1292-1298.
  27. Adams, B. D.; Black, R.; Radtke, C.; Williams, Z.; Mehdi, B. L.; Browning, N. D.; Nazar, L. F. The Importance of Nanometric Passivating Films on Cathodes for Li-Air Batteries. *ACS Nano* **2014**, *8*, 12483-12493.
  28. Kozmenkova, A. Y.; Kataev, E. Y.; Belova, A. I.; Amati, M.; Gregoratti, L.; Velasco-Vélez, J.; Knop-Gericke, A.; Senkovsky, B.; Vyalikh, D. V.; Itkis, D. M.; Shao-Horn, Y.; Yashina, L. V. Tuning Surface Chemistry of TiC Electrodes for Lithium-Air Batteries. *Chem. Mater.* **2016**, *28*, 8248-8255.
  29. Amano, F.; Nakata, M.; Yamamoto, A.; Tanaka, T. Effect of Ti<sup>3+</sup> Ions and Conduction Band Electrons on Photocatalytic and Photoelectrochemical Activity of Rutile Titania for Water Oxidation. *J Phys. Chem. C* **2016**, *120*, 6467-6474.
  30. Nowotny, M. K.; Bak, T.; Nowotny, J. Electrical Properties and Defect Chemistry of TiO<sub>2</sub> Single Crystal. I. Electrical Conductivity. *J. Phys. Chem. B* **2006**, *110*,

16270-16282.

31. Yagi, E.; Hasiguti, R. R.; Aono, M. Electronic Conduction above 4 K of Slightly Reduced Oxygen-Deficient Rutile  $\text{TiO}_{2-x}$  **1996**, *54*, 7945-7956.
32. Pei, D.-N.; Gong, L.; Zhang, A.-Y.; Zhang, X.; Chen, J.-J.; Mu, Y.; Yu, H.-Q. Defective Titanium Dioxide Single Crystals Exposed by High-Energy {001} Facets for Efficient Oxygen Reduction. *Nat. Commun.* **2015**, *6*, 8696.
33. Liu, L.; Liu, Q.; Zheng, Y.; Wang, Z.; Pan, C.; Xiao, W.  $\text{O}_2$  Adsorption and Dissociation on a Hydrogenated Anatase (101) Surface. *J. Phys. Chem. C* **2014**, *118*, 3471-3482.
34. Aetukuri, N. B.; McCloskey, B. D.; García, J. M.; Krupp, L. E.; Viswanathan, V.; Luntz, A. C. Solvating Additives Drive Solution-Mediated Electrochemistry and Enhance Toroid Growth in Non-Aqueous  $\text{Li-O}_2$  Batteries. *Nat. Chem.* **2014**, *7*, 50-56.
35. Johnson, L.; Li, C.; Liu, Z.; Chen, Y.; Freunberger, S. A.; Ashok, P. C.; Praveen, B. B.; Dholakia, K.; Tarascon, J.-M.; Bruce, P. G. The Role of  $\text{LiO}_2$  Solubility in  $\text{O}_2$  Reduction in Aprotic Solvents and Its Consequences for  $\text{Li-O}_2$  Batteries. *Nat. Chem.* **2014**, *6*, 1091-1099.
36. Gao, X.; Chen, Y.; Johnson, L.; Bruce, P. G. Promoting Solution Phase Discharge in  $\text{Li-O}_2$  Batteries Containing Weakly Solvating Electrolyte Solutions. *Nat. Mater.* **2016**, *15*, 882-889.
37. Chen, Y.; Freunberger, S. A.; Peng, Z.; Fontaine, O.; Bruce, P. G. Charging a  $\text{Li-O}_2$  Battery Using a Redox Mediator. *Nat. Chem.* **2013**, *5*, 489-494.
38. Sun, D.; Shen, Y.; Zhang, W.; Yu, L.; Yi, Z.; Yin, W.; Wang, D.; Huang, Y.; Wang, J.; Wang, D.; Goodenough, J. B. A Solution-Phase Bifunctional Catalyst for Lithium-Oxygen Batteries. *J. Am. Chem. Soc.* **2014**, *136*, 8941-8946.
39. Feng, N.; He, P.; Zhou, H. Enabling Catalytic Oxidation of  $\text{Li}_2\text{O}_2$  at the Liquid-Solid Interface: The Evolution of an Aprotic  $\text{Li-O}_2$  Battery. *ChemSusChem* **2015**, *8*, 600-602.

40. Lim, H.-D.; Song, H.; Kim, J.; Gwon, H.; Be, Y.; Park, K.-Y.; Hong, J.; Kim, H.; Kim, T.; Kim, Y. H.; Lepró, X.; Ovalle-Robles, R.; Baughman, R. H.; Kang, K. Superior Rechargeability and Efficiency of Lithium–Oxygen Batteries: Hierarchical Air Electrode Architecture Combined with a Soluble Catalyst. *Angew. Chem. Int. Ed.* **2014**, *53*, 1-7.
41. Ke, Q.; Guan, C.; Zhang, X.; Zheng, M.; Zhang, Y.-W.; Cai, Y.; Zhang, H.; Wang, J. *Adv. Mater.* **2016**.
42. Lu, X.; Wang, G.; Zhai, T.; Yu, M.; Gan, J.; Tong, Y.; Li, Y. Hydrogenated TiO<sub>2</sub> Nanotube Arrays for Supercapacitors. *Nano Lett.* **2012**, *12*, 1690-1696.
43. Liang, Z.; Zheng, G.; Li, W.; Seh, Z. W.; Yao, H.; Yan, K.; Kong, D.; Cui, Y. Sulfur Cathodes with Hydrogen Reduced Titanium Dioxide Inverse Opal Structure. *ACS Nano* **2014**, *8*, 5249-5256.
44. Shannon, R. D.; Pask, J. A. Kinetics of the Anatase-Rutile Transformation. *J. Am. Ceram. Soc.* **1965**, *48*, 391-398.
45. Vu, A.; Qian, Y.; Stein, A. Porous Electrode Materials for Lithium-Ion Batteries – How to Prepare Them and What Makes Them Special. *Adv. Energy Mater.* **2012**, *2*, 1056-1085.
46. Stephenson, D. E.; Walker, B. C.; Skelton, C. B.; Gorzkowski, E. P.; Rowenhorst, D. J.; Wheeler, D. R. Modeling 3D Microstructure and Ion Transport in Porous Li-Ion Battery Electrodes. *J. Electrochem. Soc.* **2011**, *158*, A781-A789.
47. Kim, O.-H.; Cho, Y.-H.; Kang, S. H.; Park, H.-Y.; Kim, M.; Lim, J. W.; Chung, D. Y.; Lee, M. J.; Choe, H.; Sung, Y.-E. Ordered Macroporous Platinum Electrode and Enhanced Mass Transfer in Fuel Cells Using Inverse Opal Structure. *Nat. Commun.* **2013**, *4*, 2473.
48. Cho, Y.-H.; Jung, N.; Kang, Y. S.; Chung, D. Y.; Lim, J. W.; Choe, H.; Cho, Y.-H.; Sung, Y.-E. Improved Mass Transfer Using a Pore Former in Cathode Catalyst Layer in the Direct Methanol Fuel Cell. *Int. J. Hydrogen Energ.* **2012**, *37*, 11969-11974.
49. Li, L.; Yan, J.; Wang, T.; Zhao, Z.-J.; Zhang, J.; Gong, J.; Guan, N. Sub-10 nm Rutile

- Titanium Dioxide Nanoparticles for Efficient Visible-Light-Driven Photocatalytic Hydrogen Production. *Nat. Commun.* **2015**, *6*, 5881-5890.
50. Mazza, T.; Barborini, E.; Piseri, P.; Milani, P.; Cattaneo, D.; Bassi, A. L.; Bottani, C. E.; Ducati, C. Raman Spectroscopy Characterization of TiO<sub>2</sub> Rutile Nanocrystals. *Phys. Rev. B* **2007**, *75*, 045416 (1-5).
  51. Lim, H.-D.; Lee, B. J.; Zheng, Y.; Hong, J.; Kim, J.; Gwon, H.; Ko, Y.; Lee, M.; Cho, K.; Kang, K. Rational Design of Redox Mediators for Advanced Li-O<sub>2</sub> Batteries. *Nat. Energy* **2016**, *1*, 16066.
  52. Naldoni, A.; Allieta, M.; Santangelo, S.; Marelli, M.; Fabbri, F.; Cappelli, S.; Bianchi, C. L.; Psaro, R.; Santo, V. D. Effect of Nature and Location of Defects on Bandgap Narrowing in Black TiO<sub>2</sub> Nanoparticles. *J. Am. Chem. Soc.* **2012**, *134*, 7600-7603.
  53. Chen, X.; Liu, L.; Yu, P. Y.; Mao, S. S. Increasing Solar Absorption for Photocatalysis with Black Hydrogenated Titanium Dioxide Nanocrystals. *Science* **2011**, *331*, 746-750.
  54. Cai, J.; Zhu, Y.; Liu, D.; Meng, M.; Hu, Z.; Jiang, Z. Synergistic Effect of Titanate-Anatase Heterostructure and Hydrogenation-Induced Surface Disorder on Photocatalytic Water Splitting. *ACS Catal.* **2015**, *5*, 1708-1716.
  55. Tian, M.; Mahjouri-Samani, M.; Eres, G.; Sachan, R.; Yoon, M.; Chisholm, M. F.; Wang, K.; Poretzky, A. A.; Rouleau, C. M.; Geohegan, D. B.; Duscher, G. Structure and Formation Mechanism of Black TiO<sub>2</sub> Nanoparticles. *ACS Nano* **2015**, *9*, 10482-10488.

## Appendix 1.

### Synergistic Improvement of Oxygen Reduction Reaction on Gold/Cerium-Phosphate Catalysts

#### A.1.1. Introduction

Fuel cells converting chemical energy to electrical energy have attracted a lot of interests as one of future-power-generation technologies for green economy. However, a low conversion efficiency caused by slow kinetics of oxygen reduction reaction (ORR) has been a major problem hindering practical application [1-6]. Among several types, alkaline fuel cells (AFCs) are a promising route for realizing the application of fuel cells, because of the advantages such as low anode-fuel crossover, tolerance for CO poisoning, feasible activities for non-Pt metals (e.g., Au, Ag, etc.), and non-precious metal oxides (Fe-, Co-, Ni-based oxides) [7-14]. Though non-precious metal oxides generally cost much less than Pt, they have lower electronic conductivity, and the activity is relatively low. Furthermore, the understanding of the reaction mechanisms on the catalyst is still lacking.

Progress in the *d*-band model, which describes the relation between catalytic activity and electronic structure of transition metals, allows us to systematically design and predict a brand-new catalyst on the basis of transition metals [15-17]. Of them, gold is

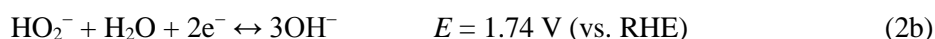
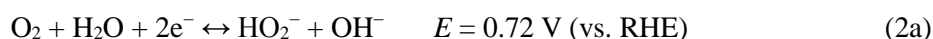
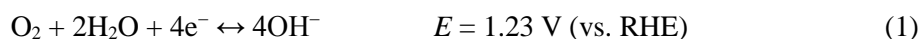
---

\*The work presented in Appendix 1 was published in *Int. J. Hydrogen Energ.* **39**, 10921 (2014) entitled, "Synergistic Improvement of Oxygen Reduction Reaction on Gold/Cerium-Phosphate Catalysts" **Joonhyeon Kang**,<sup>+</sup> Sujin Byun,<sup>+</sup> Seunghoon Nam, Suji Kang, Taeho Moon,<sup>\*</sup> and Byungwoo Park<sup>\*</sup>

known to be the most stable metal, which ensures long-term durability against dissolution.

The use of pure Au still brings up cost concerns, which is the major challenge for the application. The cost effectiveness can be adequately overcome by the introduction of Au-based composites taking advantage of the controlled electronic structure of Au. The ORR on Au surface does not occur via complete 4-electron reduction like on Pt, which encourages much effort to be made for Au to achieve comparable activity to that of Pt by alloying Au with other metals, or by combination with various metal oxides or metal phosphates [18-21].

In alkaline media, the ORR proceeds predominantly in three different pathways [22,23], as seen below, and the equilibrium potentials for each reaction at pH 13 are denoted in terms of a reversible hydrogen electrode (RHE), considering the dependence of the equilibrium potential on pH [24]:



The direct 4-electron reaction (Eq. (1)) reduces oxygen to water or hydroxyl ion as a reaction product. However, 2-electron (Eq. (2a)) or series 4-electron (Eq. (2a)  $\rightarrow$  Eq. (2b)) reaction generates hydrogen peroxides as bi-products or intermediates. The pathways are sensitive to the type and crystallographic orientation of transition metals. In the case of Au, (100) planes exhibit the highest activity through the series 4-electron

reduction pathway, whereas partial oxygen reduction to hydrogen peroxide (Eq. (2a)) occurs on (111) and (110) planes [25,26].

In the previous publications [20,21], we showed that the Au/AlPO<sub>4</sub> nanocomposite catalysts enabled 4-electron reduction in alkaline media with (111) and (110) Au orientations. The AlPO<sub>4</sub> in the binary nanocomposite played a role in enhancing the catalytic activity of Au by electronic interactions with Au, and did not participate in ORR. Therefore, ideas on finding other metal-phosphate compound that may have its own catalytic activity remained a future work to achieve better ORR efficiency.

In this paper, the Au/CePO<sub>4</sub>-binary nanocomposites are introduced as an effective oxygen-reduction catalyst in alkaline media. The ORR activity comparable with Pt is demonstrated through the serial 4-electron reduction pathway. The bi-functionality of the CePO<sub>4</sub> in Au/CePO<sub>4</sub> is suggested to explain the remarkably enhanced activity. Significantly, the own catalytic activity of CePO<sub>4</sub> for HO<sub>2</sub><sup>-</sup> intermediates is demonstrated, bringing synergistic effects with Au for more complete ORR.

### **A.1.2. Experimental Section**

The Au/CePO<sub>4</sub> nanocomposites were prepared by co-sputtering using Au and CePO<sub>4</sub> targets on ITO-coated glass at room temperature. In order to control the Au/CePO<sub>4</sub> ratio, Au-sputtering power was fixed to 10 W, and CePO<sub>4</sub>-sputtering power was changed between 20 W and 60 W. The as-deposited samples were annealed at 200°C for better adhesion to the ITO electrodes. In order to distinguish the effect of metal phosphates, the Au/AlPO<sub>4</sub> nanocomposites were prepared in the same manner [20]. For the comparison

of ORR activity, the pure Au, Pt, CePO<sub>4</sub>, and AlPO<sub>4</sub> films were also prepared.

Electrochemical characterizations, cyclic voltammetry (CV) and chronoamperometry were performed by using a potentiostat (CHI 604A: CH Instrumental Inc.). Hg/HgO and Pt wires were used as reference and counter electrodes, respectively. Oxygen reduction was measured in an O<sub>2</sub>-saturated 0.1 M NaOH solution under the oxygen flow of 30 sccm at a scan rate of 50 mV/s. H<sub>2</sub>O<sub>2</sub>-reduction measurements were carried out in a N<sub>2</sub>-purged 0.1 M NaOH solution, by adding 1.2 mM hydrogen peroxide. The surface orientation of Au in the Au/CePO<sub>4</sub> nanocomposites was estimated by underpotential deposition (UPD) using 1 mM lead nitrate (Pb(NO<sub>3</sub>)<sub>2</sub>·3H<sub>2</sub>O) dissolved in 0.1 M NaOH at a scan rate of 50 mV/s.

X-ray photoelectron spectroscopy (XPS, AXIS-HSI: KRATOS) was used to analyze the electronic states of the Au (with monochromatic Mg K $\alpha$  radiation), and the binding energy was calibrated by using the peak position of C 1s. The nanocomposite phase was identified by x-ray diffraction (XRD, D8 Advance: Bruker), and the grain size of Au was estimated using the Scherrer equation. The atomic ratios of Ce/Au in the Au/CePO<sub>4</sub> nanocomposites were confirmed to be 0.042, 0.053, and 0.086 with the CePO<sub>4</sub>-sputtering powers of 20, 40, and 60 W, respectively, as measured by an inductively coupled plasma-atomic emission spectrometer (ICP-AES, Optima-4300 DV: Perkin-Elmer).

### A.1.3. Results and Discussion

X-ray diffraction for the nanocomposites (Fig. 1) confirms polycrystalline Au phase with amorphous cerium phosphate. The grain sizes of Au were estimated to 43 nm (pure Au), 29 nm (Ce/Au = 0.042), 9 nm (Ce/Au = 0.053), and 7 nm (Ce/Au = 0.086), respectively, by the Scherrer equation of  $\Delta k$  vs.  $k$  (the scattering vector  $k = (4\pi/\lambda)\sin\theta$ ). The gradual decrease of Au-grain size with the increasing Ce/Au ratio is explained by the suppression of Au coarsening with CePO<sub>4</sub>.

The pathway for ORR on gold surface largely depends on the crystallographic surface orientation. Therefore, as shown in Fig. 2, UPD of Pb was conducted to characterize the Au surface in Au/CePO<sub>4</sub>. Since the ideal peak potentials for Pb desorption on Au (111), (100), and (110) are ~0.44, ~0.48, and ~0.56 V, respectively [27], the main desorption peaks are assigned to (111) and (110). In other words, Au (100) facets rarely exist in the nanocomposite, and this means that the Au/CePO<sub>4</sub> nanocomposite mainly has the pathway via partial oxygen reduction (Eq. (2a)) generating HO<sub>2</sub><sup>-</sup>. The electrochemical surface areas were estimated to approximately 1.91, 1.78, 2.29, and 1.61 cm<sup>2</sup> per cm<sup>2</sup> sample, respectively, for pure Au, Ce/Au = 0.042, 0.053, 0.086. The nanocomposite with Ce/Au = 0.053 exhibits the largest area, due to the optimization between Au coarsening (grain growth) and electronic percolation among the Au nanocrystals [28-30].

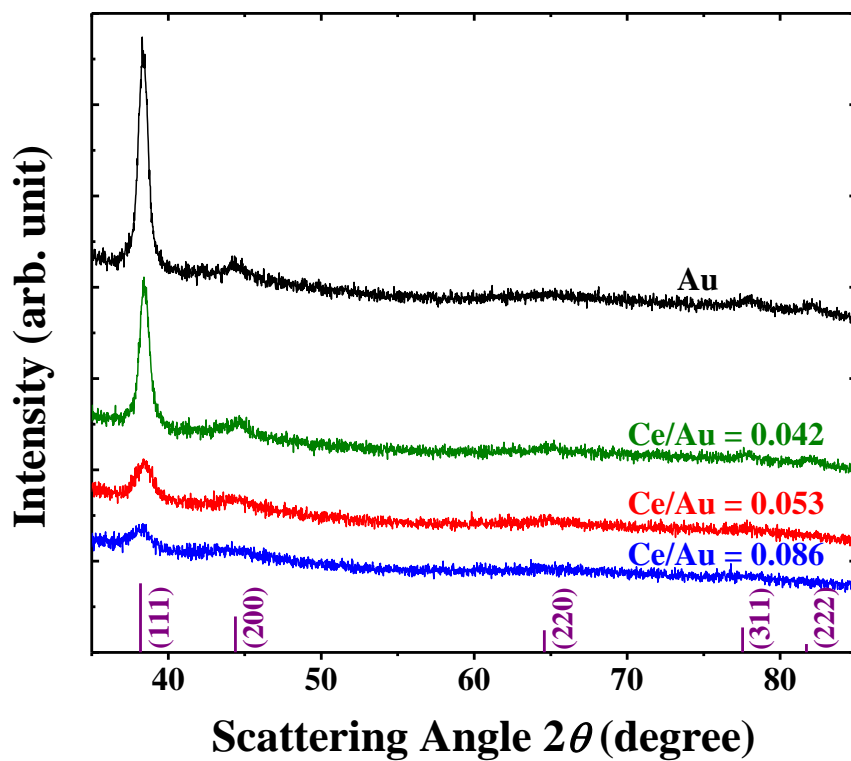


Fig. A1-1. (Color) X-ray diffraction of the Au thin film and Au/CePO<sub>4</sub> nanocomposites. The ideal peak positions and intensities for Au (JCPDS 04-0784) are marked at the bottom.

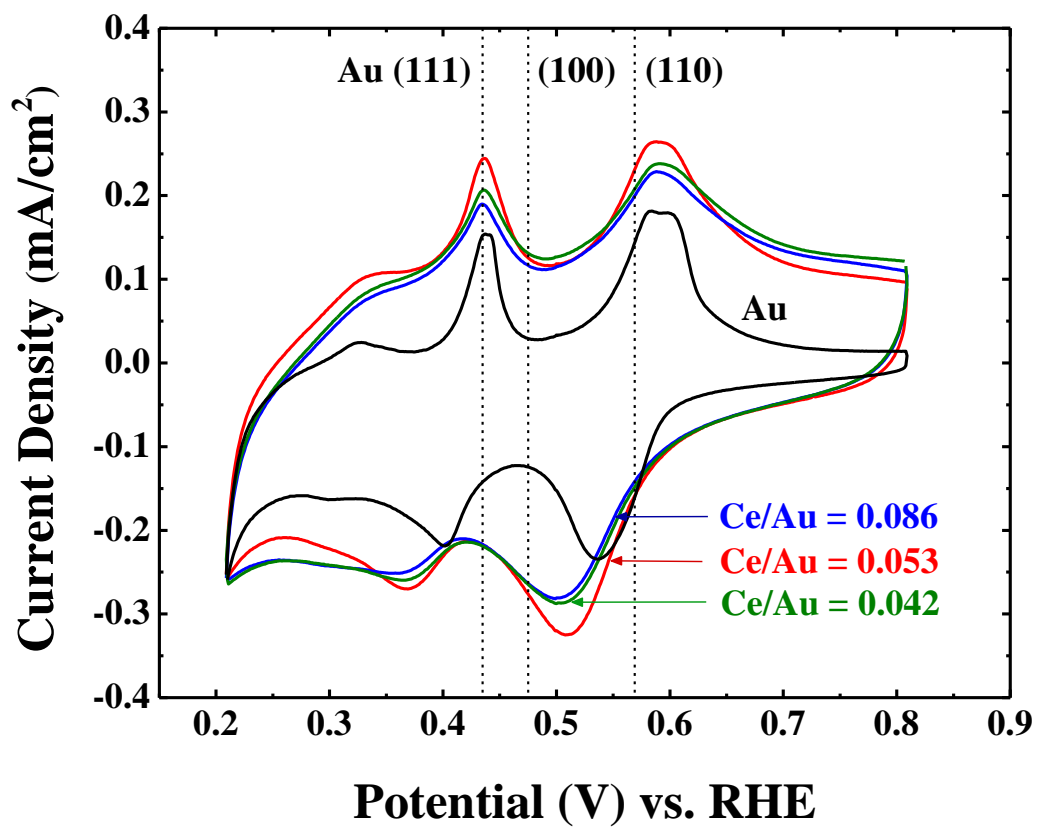


Fig. A1-2. (Color) Underpotential deposition (UPD) experiments of lead on Au and Au/CePO<sub>4</sub> nanocomposites. The desorption potential of lead on Au (111), (100), and (110) are marked with dashed lines.

To compare the ORR activities of Au and Au/CePO<sub>4</sub> composites, cyclic voltammograms were obtained in an O<sub>2</sub>-saturated solution (pH 13). By the incorporation of CePO<sub>4</sub> to Au, two distinctive features are shown compared to the pure Au, as shown in Fig. 3. First, reduction current is remarkably promoted within the potential region of approximately 0.6 - 0.9 V, with a positive shift of the onset potential. Second, the oxidation peak at ~0.9 V (assigned to oxidation of residual HO<sub>2</sub><sup>-</sup> [31,32]) are hardly observed on the reverse sweep, which implies that HO<sub>2</sub><sup>-</sup> were almost consumed during the prior cathodic sweep. In particular, the Au/CePO<sub>4</sub> nanocomposite with Ce/Au = 0.053 exhibits the most enhanced catalytic properties for oxygen reduction with a most-positive shift of the onset potential, up to over ~50 mV compared to pure Au. The reduction-current density is comparable to that of pure Pt, which is nearly twofold of pure Au, and the oxidative current peak on the reverse sweep (at ~0.9 V) is not observed.

The limiting current densities ( $i_L$ ) for two- and four- electron processes were estimated to -0.32 and -0.63 mA/cm<sup>2</sup>, respectively, from  $i_L = -DnFc^*/\delta$  [33], where  $D$  is the O<sub>2</sub>-diffusion coefficient ( $\sim 2.6 \times 10^{-5}$  cm<sup>2</sup>/s) [34],  $F$  is the Faraday constant (96,485 C/mol),  $c^*$  is the O<sub>2</sub>-bulk concentration ( $\sim 1.26$  mM) [35],  $n$  is the number of involved electrons, and  $\delta$  is the diffusion-layer thickness ( $\sim 200$   $\mu$ m), assuming no convection [36]. From the simple calculation, four-electron process is confirmed to be achieved in the Au/CePO<sub>4</sub> nanocomposite, which is further supported by the disappearance of the oxidative current for residual HO<sub>2</sub><sup>-</sup>.

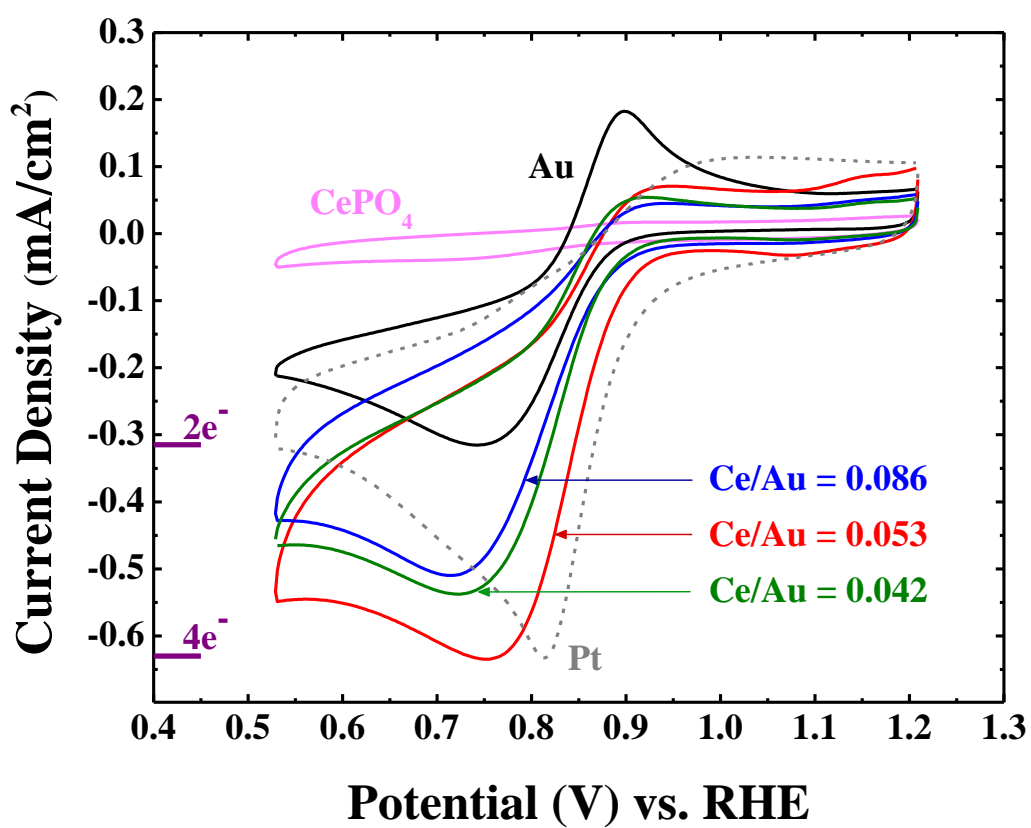


Fig. A1-3. (Color) Oxygen-reduction activities for the Au, Pt, and CePO<sub>4</sub> thin films, and Au/CePO<sub>4</sub> nanocomposites. The calculated current densities corresponding to two-electron and four-electron reactions are also marked, respectively.

To better understand why the Au composite with CePO<sub>4</sub> induces the remarkable enhancement of catalytic activity, the electronic modification of Au is observed by XPS (Fig. 4). While pure Au is identified by  $4f_{5/2}$  and  $4f_{7/2}$  of 87.7 and 84.0 eV, respectively [37,38], the binding energy shifts lower in the Au/CePO<sub>4</sub> nanocomposites, and this changed electronic structure is due to the electron transfer between CePO<sub>4</sub> and Au by the Fermi-level difference [39]. Many researchers have shown that the shift direction of core level ( $f$  band) is in accordance with that of valence level ( $d$  band) determining the reactivity of transition-metal surface [40-45].

Based on the results of Au- $4f$  shift toward lower binding energy, the position of the  $d$ -band center is estimated to be shifted up toward Fermi level. According to the  $d$ -band model, higher position of  $d$ -band centers (i.e., closer to the Fermi level) implies stronger bonds between adsorbates and metal surface, leading to further reduction of reactant molecules [46-49]. The XPS analyses reveal that combining Au with CePO<sub>4</sub> induces favorable shift of Au-electronic level, facilitating reduction kinetics for the chemisorbed reactants on the Au surface. Therefore, complete ORR can be achieved for the Au nanocrystals that are effectively interacted with CePO<sub>4</sub>.

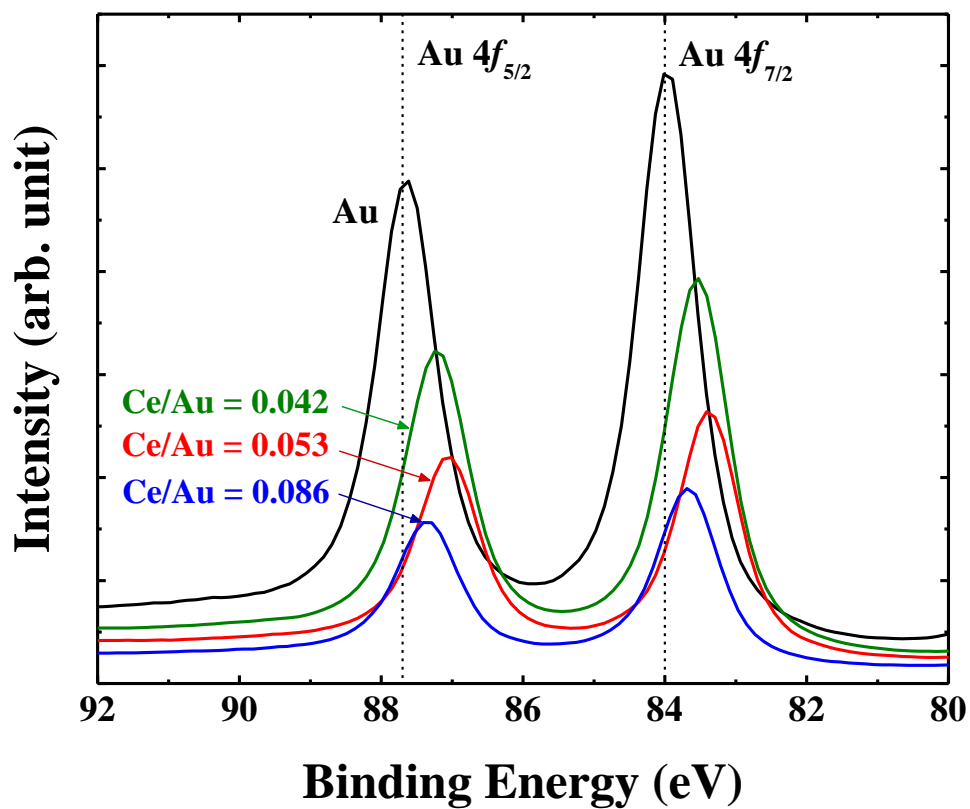


Fig. A1-4. (Color) Au 4f XPS spectra for the Au and Au/CePO<sub>4</sub> nanocomposite electrodes.

The dashed lines are from the standard Au.

The chronoamperometry with hydrogen peroxide can be a tool for identifying only the activity for the reduction of  $\text{HO}_2^-$  (Eq. (2b)) on the way to the whole serial 4-electron reduction path, since hydrogen peroxide mainly exists as a radical form ( $\text{HO}_2^-$ ) at pH 13 [24]. At the applied potential of 0.709 V (Fig. 5(a)), the pure  $\text{CePO}_4$  shows negligible current. As the applied potential becomes negative down to 0.509 V (Fig 5(b)), however, the reduction current for the pure  $\text{CePO}_4$  appears, which implies that  $\text{CePO}_4$  has its own catalytic activity on  $\text{HO}_2^-$ . Recently, our group reported the enhancement of ORR activity in  $\text{Au}/\text{AlPO}_4$  with the same thin-film composite geometry [20,21]. In order to compare the effect of metal phosphates on Au-catalytic properties, chronoamperometry and ORR experiments were performed again for the pure  $\text{AlPO}_4$  and the  $\text{Au}/\text{AlPO}_4$  nanocomposite (optimized by the composition,  $\text{Al}/\text{Au} = 0.087$ ), respectively. The chronoamperometry results of Fig. 5(c) reveal that the pure  $\text{AlPO}_4$  has no activity for  $\text{HO}_2^-$ , unlike the case of  $\text{CePO}_4$  (Fig. 5(b) vs. Fig. 5(c)). Therefore, it is evident that the initial oxygen reduction on the Au surface (Eq. (1)) leads to the formation of  $\text{HO}_2^-$ , and is extended to the reduction of  $\text{HO}_2^-$  in which the  $\text{CePO}_4$  itself can participate. This remarkable difference of the  $\text{HO}_2^-$  reduction between  $\text{AlPO}_4$  and  $\text{CePO}_4$  is directly reflected on the ORR curves, as shown in Fig. 5(d).

In the cathodic region below  $\sim 0.7$  V, the reduction current of  $\text{Au}/\text{CePO}_4$  is much higher than that of the  $\text{Au}/\text{AlPO}_4$ , and this is well explained by the reduction-activity difference of  $\text{HO}_2^-$  between  $\text{CePO}_4$  and  $\text{AlPO}_4$  in the similar voltage range. Furthermore, in the case of the  $\text{Au}/\text{CePO}_4$ , the anodic current peak at  $\sim 0.9$  V is hardly observed, unlike the  $\text{Au}/\text{AlPO}_4$ . This suggests that most of  $\text{HO}_2^-$  is reduced on the  $\text{Au}/\text{CePO}_4$  surface

through the functionality of the CePO<sub>4</sub>. The enhancement mechanisms by CePO<sub>4</sub> are schemed in Figs. 5(e) and (f).

Although CePO<sub>4</sub> itself did not have reactivity for oxygen, it exhibited considerable activity for the reaction intermediate. Therefore, CePO<sub>4</sub> can actively participate in the catalytic reaction by reducing the residual HO<sub>2</sub><sup>-</sup> produced from the uncompleted ORR on Au. Because unaltered pure Au has poor activity for HO<sub>2</sub><sup>-</sup>, the catalytic characteristic of CePO<sub>4</sub> is effectively complementary to Au. The bi-functionality of CePO<sub>4</sub>, both the modification of Au-electronic structure and the catalytic activity for HO<sub>2</sub><sup>-</sup>, brings synergy for more complete ORR in the Au/CePO<sub>4</sub> nanocomposites.

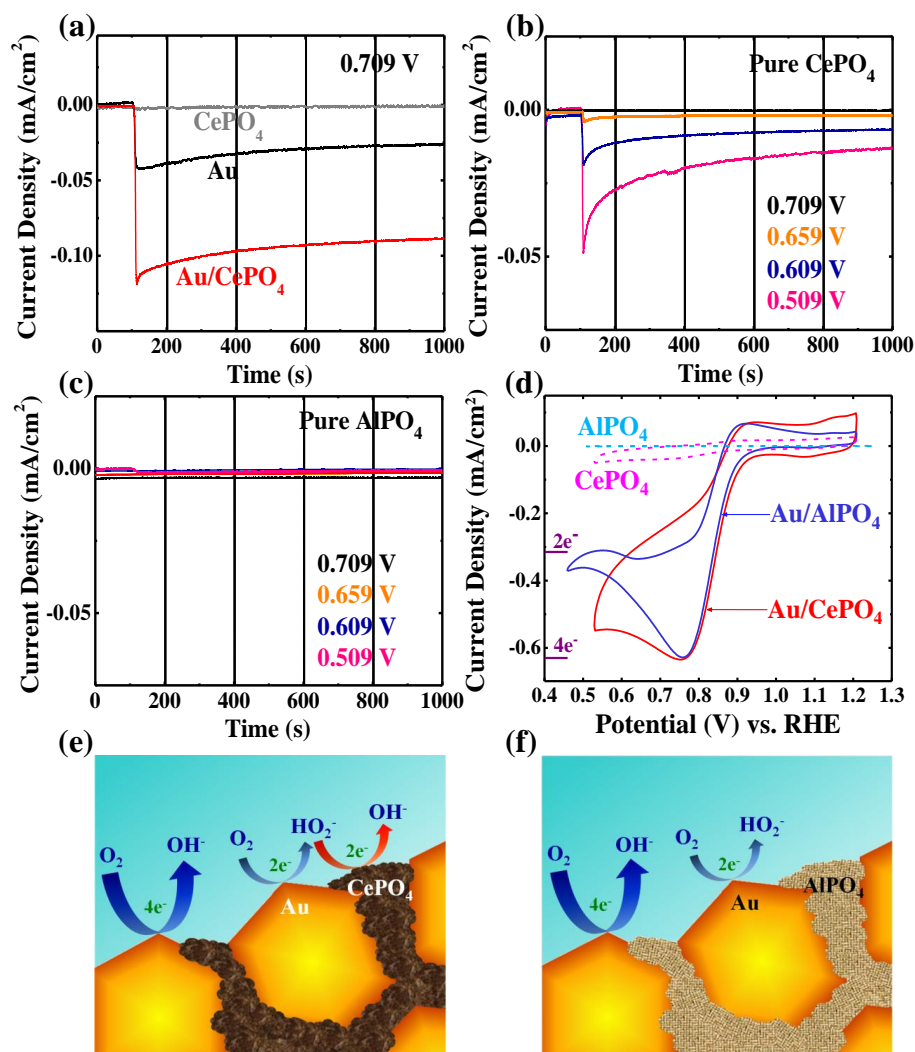


Fig. A1-5. (Color) ORR-enhancement mechanisms. (a-c) Hydrogen-peroxide reduction activities measured by chronoamperometry by adding H<sub>2</sub>O<sub>2</sub> at 100 s. (a) The Au, CePO<sub>4</sub>, and Au/CePO<sub>4</sub> nanocomposites at 0.709 V (vs. RHE). (b-c) The pure CePO<sub>4</sub> and AlPO<sub>4</sub> at different applied potentials. (d) ORR-activity comparisons between the Au/CePO<sub>4</sub> and Au/AlPO<sub>4</sub> nanocomposites. (e-f) Schemes representing the ORR mechanisms on (e) Au/CePO<sub>4</sub> and (f) Au/AlPO<sub>4</sub>.

#### **A.1.4. Conclusions**

Oxygen-reduction activity for the Au/CePO<sub>4</sub> nanocomposites was investigated in alkaline media. Compared to the pure Au showing partial 2-electron reduction, the binary composites exhibited nearly complete ORR through the serial 4-electron reduction pathway, fully reducing reaction intermediates. Two enhancement mechanisms were demonstrated to explain the role of CePO<sub>4</sub> in the composite catalyst. First, electronic interactions between the Au and CePO<sub>4</sub>, as revealed by XPS, enhanced the ORR kinetics for Au by the shift of Au-energy levels determining adsorption properties of reactant molecules on Au surface. Second, its own catalytic activity of CePO<sub>4</sub> for hydrogen-peroxide reduction, observed by chronoamperometry, was effectively complementary to Au having poor activity for hydrogen peroxide. The bi-functionality of both the electronic modification of Au and the catalytic activity for HO<sub>2</sub><sup>-</sup> conveys synergistic effect for efficient oxygen reduction. As a future work, performance with a full-cell configuration will be necessary to verify the potential for future applications as a fuel-cell cathode. Also, the proposed strategy combining the two catalyst materials, each of which plays a different role, furnishes an advanced insight into the design of a new catalyst.

### A.1.5. References

1. L. Carrette, K. A. Friedrich, U. Stimming. Fuel Cells-Fundamentals and Applications. *Fuel Cells* **1** (2001) 5-39.
2. K. E. Swider-Lyons, S. A. Campbell. Physical Chemistry Research Toward Proton Exchange Membrane Fuel Cell Advancement. *J. Phys. Chem. Lett.* **4** (2013) 393-401.
3. J. K. Nørskov, J. Rossmeisl, A. Logadottir, L. Lindqvist, J. R. Kitchin, T. Bligaard, H. Jónsson. Origin of the Overpotential for Oxygen Reduction at a Fuel-Cell Cathode. *J. Phys. Chem. B* **108** (2004) 17886-17892.
4. W. Sheng, H. A. Gasteiger, Y. Shao-Horn. Hydrogen Oxidation and Evolution Reaction Kinetics on Platinum: Acid vs Alkaline Electrolytes. *J. Electrochem. Soc.* **157** (2010) B1529-B1536.
5. T. He, E. Kreidler, L. Xiong, E. Ding. Combinatorial Screening and Nano-Synthesis of Platinum Binary Alloys for Oxygen Electroreduction. *J. Power Sources*, **165** (2007) 87-91.
6. M. Seo, Y. Yun, J. Lee, Y. Tak. Electrochemical Characteristics of Chloride Ion Modified Pt Cathode in Direct Methanol Fuel Cells. *J. Power Sources* **159** (2006) 59-62.
7. J. S. Spendelow, J. D. Goodpaster, P. J. A. Kenis, A. Wieckowski. Mechanism of CO Oxidation on Pt (111) in Alkaline Media. *J. Phys. Chem. B* **110** (2006) 9545-9555.
8. K. Matsuoka, K. Miyazaki, Y. Iriyama, K. Kikuchi, T. Abe, Z. Ogumi. Novel Anode Catalyst Containing Gold Nanoparticles for Use in Direct Methanol Fuel Cells. *J. Phys. Chem. C* **111** (2007) 3171-3174.
9. H. Bunazawa, Y. Yamazaki. Influence of Anion Ionomer Content and Silver Cathode Catalyst on the Performance of Alkaline Membrane Electrode Assemblies (MEAs) for Direct Methanol Fuel Cells (DMFCs). *J. Power Sources* **182** (2008) 48-51.
10. J. R. Varcoe, R. C. T. Slade. Prospects for Alkaline Anion-Exchange Membrane in

- Low Temperature Fuel Cells. *Fuel Cells* **5** (2005) 187-200.
11. J. R. Varcoe, R. C. T. Slade, G. L. Wright, Y. Chen. Steady-State dc and Impedance Investigations of H<sub>2</sub>/O<sub>2</sub> Alkaline Membrane Fuel Cells with Commercial Pt/C, Ag/C, and Au/C Cathodes. *J. Phys. Chem. B* **110** (2006) 21041-21049.
  12. Y. Liang, H. Wang, J. Zhou, Y. Li, J. Wang, T. Regier, H. Dai. Covalent Hybrid of Spinel Manganese-Cobalt Oxide and Graphene as Advanced Oxygen Reduction Electrocatalysts. *J. Am. Chem. Soc.* **134** (2012) 3517-3523.
  13. V. Neburchilov, H. Wang, J. J. Martin, W. Qu. A Review on Air Cathodes for Zinc-Air Fuel Cells. *J. Power Sources* **195** (2010) 1271-1291.
  14. M. De Koninck, B. Marsan. Mn<sub>x</sub>Cu<sub>1-x</sub>Co<sub>2</sub>O<sub>4</sub> Used as Bifunctional Electrocatalyst in Alkaline Medium. *Electrochim. Acta* **53** (2008) 7012-7021.
  15. J. Greeley, J. K. Nørskov, M. Mavrikakis. Electronic Structure and Catalysis on Metal Surfaces. *Annu. Rev. Phys. Chem.* **53** (2002) 319-348.
  16. J. K. Nørskov, T. Bligaard, J. Rossmeisl, C. H. Christensen. Towards the Computational Design of Solid Catalysts. *Nat. Chem.* **1** (2009) 37-46.
  17. T. Jiang, D. J. Mowbray, S. Dobrin, H. Falsig, B. Hvolbaek, T. Bligaard, J. K. Nørskov. Trends in CO Oxidation Rates for Metal Nanoparticles and Close-Packed, Stepped, and Kinked Surfaces. *J. Phys. Chem. C* **113** (2009) 10548-10553.
  18. M. Nie, P. K. Shen, Z. Wei. Nanocrystalline Tungsten Carbide Supported Au-Pd Electrocatalyst for Oxygen Reduction. *J. Power Sources* **167** (2007) 69-73.
  19. C. Lin, Y. Song, L. Cao, S. Chen. Oxygen Reduction Catalyzed by Au-TiO<sub>2</sub> Nanocomposites in Alkaline Media. *ACS Appl. Mater. Interfaces* **5** (2013) 13305-13311.
  20. Y. Park, B. Lee, C. Kim, J. Kim, S. Nam, Y. Oh, B. Park. Modification of Gold Catalysis with Aluminum Phosphate for Oxygen-Reduction Reaction. *J. Phys. Chem. C* **114** (2010) 3688-3692.
  21. Y. Park, S. Nam, Y. Oh, H. Choi, J. Park, B. Park. Electrochemical Promotion of

- Oxygen Reduction on Gold with Aluminum-Phosphate Overlayer. *J. Phys. Chem. C* **115** (2011) 7092-7096.
22. N. A. Anastasijević, V. B. Vesović, R. R. Adžić. Determination of the Kinetics Parameters of the Oxygen Reduction Reaction Using the Rotating Ring-Disk Electrode. *J. Electroanal. Chem.* **229** (1987) 305-316.
  23. L. An, T. S. Zhao, L. Zeng, X. H. Yan. Performance of an Alkaline Direct Ethanol Fuel Cell with Hydrogen Peroxide as Oxidant. *Int. J. Hydrogen Energy* **39** (2014) 2320-2324.
  24. M. Pourbaix, Atlas of Electrochemical Equilibria in Aqueous Solutions. National Association of Corrosion Engineers, Houston, 1974.
  25. R. R. Adžić, N. M. Marković, V. B. Vesović. Structural Effects in Electrocatalysis Oxygen Reduction on the Au (100) Single Crystal Electrode. *J. Electroanal. Chem.* **165** (1984) 105-120.
  26. N. M. Marković, R. R. Adžić, V. B. Vesović. Structural Effects in Electrocatalysis Oxygen Reduction on the Gold Single Crystal Electrodes with (110) and (111) Orientations. *J. Electroanal. Chem.* **165** (1984) 121-133.
  27. J. Hernández, J. Solla-Gullón, E. Herrero. Gold Nanoparticles Synthesized in a Water-in-Oil Microemulsion: Electrochemical Characterization and Effect of the Surface Structure on the Oxygen Reduction Reaction. *J. Electroanal. Chem.* **574** (2004) 185-196.
  28. C. Kim, B. Lee, Y. Park, B. Park, J. Lee, H. Kim. Iron-Phosphate/Platinum/Carbon Nanocomposites for Enhanced Electrocatalytic Stability. *Appl. Phys. Lett.* **91** (2007) 113101.
  29. J. Kang, S. Nam, Y. Oh, H. Choi, S. Wi, B. Lee, T. Hwang, S. Hong, B. Park. Electronic Effect in Methanol Dehydrogenation on Pt Surfaces: Potential Control during Methanol Electrooxidation. *J. Phys. Chem. Lett.* **4** (2013) 2931-2936.
  30. Y. Oh, S. Nam, S. Wi, J. Kang, T. Hwang, S. Lee, H. H. Park, J. Cabana, C. Kim, B. Park. Effective Wrapping of Graphene on Individual  $\text{Li}_4\text{Ti}_5\text{O}_{12}$  Grains for High-Rate

- Li-Ion Batteries. *J. Mater. Chem. A* **2** (2014) 2023-2027.
31. S. Štrbac, R. R. Adžić. The Influence of OH<sup>-</sup> Chemisorption on the Catalytic Properties of Gold Single Crystal Surfaces for Oxygen Reduction in Alkaline Solutions. *J. Electroanal. Chem.* **403** (1996) 169-181.
  32. E. I. Rogers, X.-J. Huang, E. J. F. Dickinson, C. Hardacre, R. G. Compton. Investigating the Mechanism and Electrode Kinetics of the Oxygen|Superoxide (O<sub>2</sub>|O<sub>2</sub><sup>-</sup>) Couple in Various Room-Temperature Ionic Liquids at Gold and Platinum Electrodes in the Temperature Range 298-318 K. *J. Phys. Chem. C* **113** (2009) 17811-17823.
  33. J. Bockris, A. Reddy. *Modern Electrochemistry*. Plenum Press, New York, 1970.
  34. I. M. Kolthoff, C. S. Miller. The Reduction of Oxygen at the Dropping Mercury Electrode. *J. Am. Chem. Soc.* **63** (1941) 1013-1017.
  35. W. Chen, J. Kim, S. Sun, S. Chen. Electrocatalytic Reduction of Oxygen by FePt Alloy Nanoparticles. *J. Phys. Chem. C* **112** (2008) 3891-3898.
  36. B. H. Ern , F. Ozanam, J.-N. Chazalviel. The Mechanism of Hydrogen Gas Evolution on GaAs Cathodes Elucidated by In Situ Infrared Spectroscopy. *J. Phys. Chem. B* **103** (1999) 2948-2962.
  37. K. Takahiro, S. Oizumi, A. Terai, K. Kawatsura, B. Tsuchiya, S. Nagata, S. Yamamoto, H. Naramoto, K. Narumi, M. Sasase. Core Level and Valence Band Photoemission Spectra of Au Clusters Embedded in Carbon. *J. Appl. Phys.* **100** (2006) 084325.
  38. J. F. Moulder, W. F. Stickle, P. E. Sobol, K. D. Bomben. *Handbook of X-Ray Photoelectron Spectroscopy*. Perkin-Elmer Corporation, Waltham, 1992.
  39. W. Vielstich, A. Lamm, H. A. Gasteiger. *Handbook of Fuel Cells*. John Wiley & Sons Ltd., New York, 2003, Vol. 2: Electrocatalysis.
  40. W. P. Zhou, A. Lewera, R. Larsen, R. I. Masel, P. S. Bagus, A. Wieckowski. Size Effects in Electronic and Catalytic Properties of Unsupported Palladium

- Nanoparticles in Electrooxidation of Formic Acid. *J. Phys. Chem. B* **110** (2006) 13393-13398.
41. B. Hammer, Y. Morikawa, J. K. Nørskov. CO Chemisorption at Metal Surfaces and Overlayers. *Phys. Rev. Lett.* **76** (1996) 2141-2144.
  42. T. Toda, H. Igarashi, H. Uchida, M. Watanabe. Enhancement of the Electroreduction of Oxygen on Pt Alloys with Fe, Ni, and Co. *J. Electrochem. Soc.* **146** (1999) 3750-3756.
  43. J. A. Rodriguez, D. W. Goodman. The Nature of the Metal-Metal Bond in Bimetallic Surfaces. *Science* **257** (1992) 897-903.
  44. V. Stamenkovic, B. S. Mun, K. J. J. Mayrhofer, P. N. Ross, N. M. Markovic, J. Rossmeisl, J. Greeley, J. K. Nørskov. Changing the Activity of Electrocatalysts for Oxygen Reduction by Tuning the Surface Electronic Structure. *Angew. Chem., Int. Ed.* **45** (2006) 2897-2901.
  45. M. A. Rigsby, W.-P. Zhou, A. Lewera, H. T. Duong, P. S. Bagus, W. Jaegermann, R. Hunger, A. Wieckowski. Experiment and Theory of Fuel Cell Catalysis: Methanol and Formic Acid Decomposition on Nanoparticle Pt/Ru. *J. Phys. Chem. C* **112** (2008) 15595-15601.
  46. B. Hammer, J. K. Nørskov. Electronic Factors Determining the Reactivity of Metal Surfaces. *Surf. Sci.* **343** (1995) 211-220.
  47. V. Pallassana, M. Neurock, L. B. Hansen, B. Hammer, J. K. Nørskov. Theoretical Analysis of Hydrogen Chemisorption on Pd (111), Re (0001) and Pd<sub>ML</sub>/Re (0001), Re<sub>ML</sub>/Pd (111) Pseudomorphic Overlayers. *Phys. Rev. B* **60** (1999) 6146-6154.
  48. A. Nilsson, L. G. M. Pettersson, B. Hammer, T. Bligaard, C. H. Christensen, J. K. Nørskov. The Electronic Structure Effect in Heterogeneous Catalysis. *Catal. Lett.* **100** (2005) 111-114.
  49. J. K. Nørskov, F. Abild-Pedersen, F. Studt, T. Bligaard. Density Functional Theory in Surface Chemistry. *Proc. Natl. Acad. Sci.* **108** (2011) 937-943.

## Appendix 2.: List of Publications and Presentations

### A.2.1. Publications (International):

1. **Joonhyeon Kang**, Jinyoung Kim, Sangheon Lee, Sungun Wi, Chunjoong Kim, Seunghoon Nam,\* Yongjoon Park,\* and Byungwoo Park,\* “Breathable Carbon-Free Electrode: Black TiO<sub>2</sub> with Hierarchically-Ordered Porous Structure for Stable Li-O<sub>2</sub> Batteries,” submitted to *Nat. Commun.*
2. **Joonhyeon Kang**,<sup>+</sup> Sujin Byun,<sup>+</sup> Seunghoon Nam, Suji Kang, Taeho Moon,\* and Byungwoo Park,\* “Synergistic Improvement of Oxygen Reduction Reaction on Gold/Cerium-Phosphate Catalysts,” *Int. J. Hydrogen Energ.* **39**, 10921 (2014).
3. **Joonhyeon Kang**, Seunghoon Nam, Yuhong Oh, Hongsik Choi, Sungun Wi, Byungho Lee, Taehyun Hwang, Saeromi Hong, and Byungwoo Park,\* “Electronic Effect in Methanol Dehydrogenation on Pt Surfaces: Potential Control during Methanol Electrooxidation,” *J. Phys. Chem. Lett.* **4**, 2931 (2013).
4. Sungun Wi,<sup>+</sup> Jungjin Park,<sup>+</sup> Sangheon Lee, **Joonhyeon Kang**, Taehyun Hwang, Kug-Seung Lee, Han-Koo Lee, Seunghoon Nam, Chunjoong Kim,\* Yung-Eun Sung,\* and Byungwoo Park,\* “Synchrotron-Based X-Ray Absorption Spectroscopy for the Electronic Structure of Li<sub>x</sub>Mn<sub>0.8</sub>Fe<sub>0.2</sub>PO<sub>4</sub> Mesocrystal in Li<sup>+</sup> Batteries,” *Nano Energy* **31**, 495 (2017).
5. Sungun Wi, Jaewon Kim, Sangheon Lee, **Joonhyeon Kang**, Kyung Hwan Kim, Kimin Park, Kunsu Kim, Seunghoon Nam,\* Chunjoong Kim,\* and Byungwoo Park,\* “Synchrotron-Based X-Ray Absorption Spectroscopy for the Electronic Structure of Li<sub>x</sub>Mn<sub>0.8</sub>Fe<sub>0.2</sub>PO<sub>4</sub> Mesocrystal in Li<sup>+</sup> Batteries,” *Electrochim. Acta* **216**, 203 (2016).

6. Sungun Wi,<sup>+</sup> Jaewon Kim,<sup>+</sup> Kimin Park,<sup>+</sup> Sangheon Lee, **Joonhyeon Kang**, Kyung Hwan Kim, Seunghoon Nam,<sup>\*</sup> Chunjoong Kim,<sup>\*</sup> and Byungwoo Park,<sup>\*</sup> “Evaluation of Graphene-Wrapped LiFePO<sub>4</sub> as Novel Cathode Materials for Li-Ion Batteries,” *RSC Adv.* **6**, 105081 (2016).
7. Hyungsub Woo, **Joonhyeon Kang**, Jaewook Kim, Chunjoong Kim,<sup>\*</sup> Seunghoon Nam,<sup>\*</sup> and Byungwoo Park,<sup>\*</sup> “Development of Carbon-Based Cathodes for Li-Air Batteries: Present and Future,” *Electron. Mater. Lett.* **12**, 551 (2016).
8. Sangheon Lee,<sup>+</sup> Joseph C. Flanagan,<sup>+</sup> **Joonhyeon Kang**, Jinhyun Kim, Moonsub Shim,<sup>\*</sup> and Byungwoo Park,<sup>\*</sup> “Integration of CdSe/CdSe<sub>x</sub>Te<sub>1-x</sub> Type-II Heterojunction Nanorods into Hierarchically Porous TiO<sub>2</sub> Electrode for Efficient Solar Energy Conversion,” *Sci. Rep.* **5**, 17472 (2015).
9. Woojin Lee, Taehyun Hwang, Sangheon Lee, Seung-Yoon Lee, **Joonhyeon Kang**, Byungho Lee, Jinhyun Kim, Taeho Moon,<sup>\*</sup> and Byungwoo Park,<sup>\*</sup> “Organic-Acid Texturing of Transparent Electrodes Toward Broadband Light Trapping in Thin-Film Solar Cells,” *Nano Energy* **17**, 180 (2015).
10. Seunghoon Nam, Seung Jae Yang, Sangheon Lee, Jaewon Kim, **Joonhyeon Kang**, Jun Young Oh, Chong Rae Park, Taeho Moon,<sup>\*</sup> Kyu Tae Lee,<sup>\*</sup> and Byungwoo Park,<sup>\*</sup> “Wrapping SnO<sub>2</sub> with Porosity-Tuned Graphene as a Strategy for High-Rate Performance in Lithium Battery Anodes,” *Carbon* **85**, 289 (2015).
11. Hongsik Choi, Taehyun Hwang, Sangheon Lee, Seunghoon Nam, **Joonhyeon Kang**, Byungho Lee, and Byungwoo Park,<sup>\*</sup> “The Construction of Tandem Dye-Sensitized Solar Cells from Chemically-Derived Nanoporous Photoelectrodes,” *J. Power Sources* **274**, 937 (2015).

12. Sungun Wi,<sup>+</sup> Hyungsub Woo,<sup>+</sup> Sangheon Lee, **Joonhyeon Kang**, Jaewon Kim, Subin An, Chohui Kim, Seunghoon Nam, Chunjoong Kim, and Byungwoo Park,<sup>\*</sup> “Reduced Graphene Oxide/Carbon Double-Coated 3-D Porous ZnO Aggregates as High-Performance Li-Ion Anode Materials,” *Nanoscale Res. Lett.* **10**, 204 (2015).
13. Yuhong Oh,<sup>+</sup> Seunghoon Nam,<sup>+</sup> Sungun Wi, **Joonhyeon Kang**, Taehyun Hwang, Sangheon Lee, Helen Hejin Park, Jordi Cabana, Chunjoong Kim,<sup>\*</sup> and Byungwoo Park,<sup>\*</sup> “Effective Wrapping of Graphene on Individual Li<sub>4</sub>Ti<sub>5</sub>O<sub>12</sub> Grains for High-Rate Li-Ion Batteries,” *J. Mater. Chem. A* **2**, 2023 (2014).
14. Sungun Wi, Jaewon Kim, Seunghoon Nam, **Joonhyeon Kang**, Sangheon Lee, Hyungsub Woo, Moosang Lee, Chong Ho Sonu, Taeho Moon,<sup>\*</sup> and Byungwoo Park,<sup>\*</sup> “Enhanced Rate Capability of LiMn<sub>0.9</sub>Mg<sub>0.1</sub>PO<sub>4</sub> Nanoplates by Reduced Graphene Oxide/Carbon Double Coating for Li-Ion Batteries,” *Curr. Appl. Phys.* **14**, 725 (2014).
15. Hongsik Choi, Jongmin Kim, Changwoo Nahm, Chohui Kim, Seunghoon Nam, **Joonhyeon Kang**, Byungho Lee, Taehyun Hwang, Suji Kang, Dong Joo Choi, Young-Ho Kim,<sup>\*</sup> and Byungwoo Park,<sup>\*</sup> “The Role of ZnO-Coating-Layer Thickness on the Recombination in CdS Quantum-Dot-Sensitized Solar Cells,” *Nano Energy* **2**, 1218 (2013).
16. Jongmin Kim, Hongsik Choi, Changwoo Nahm, Chohui Kim, Seunghoon Nam, Suji Kang, Dae-Ryong Jung, Jae Ik Kim, **Joonhyeon Kang**, and Byungwoo Park,<sup>\*</sup> “The Role of a TiCl<sub>4</sub> Treatment on the Performance of CdS Quantum-Dot-Sensitized Solar Cells,” *J. Power Sources* **220**, 108 (2012).

17. Yuhong Oh, **Joonhyeon Kang**, Seunghoon Nam, Sujin Byun, and Byungwoo Park,\*  
“Pt/AlPO<sub>4</sub> Nanocomposite Thin-Film Electrodes for Ethanol Electrooxidation,”  
*Mater. Chem. Phys.* **135**, 188 (2012).
  
18. Jungjin Park, Yuhong Oh, Yejun Park, Seunghoon Nam, Joonhee Moon, **Joonhyeon Kang**, Dae-Ryong Jung, Sujin Byun, and Byungwoo Park,\* “Methanol Oxidation in Nanostructured Platinum/Cerium-Phosphate Thin Films,” *Curr. Appl. Phys.* **11**, S2 (2011).

### **A.2.2. Presentations (International):**

1. **Joonhyeon Kang**, Sujin Byun, Yuhong Oh, Seunghoon Nam, Suji Kang, and Byungwoo Park, “Correlation between Catalytic Activity for Methanol Dehydrogenation and Surface Electronic Structure of Platinum,” *Materials Research Society (MRS) Fall Meeting*. Boston, MA, November 2012.  
[Oral by **J. Kang**]
2. Sangheon Lee, Joseph C. Flanagan, **Joonhyeon Kang**, Jinhyun Kim, Moonsub Shim, and Byungwoo Park, “Integration of II-VI Nanorods in Sensitized Photovoltaics via Open-Structured Photoanode and Co-Sensitization Strategy,” *Materials Research Society (MRS) Fall Meeting*. Boston, MA, November 26-December 2, 2016.
3. Sangheon Lee, Joseph C. Flanagan, **Joonhyeon Kang**, Jinhyun Kim, Moonsub Shim, and Byungwoo Park, “Integration of II-VI Nanorods in Sensitized Photovoltaics via Open-Structured Photoanode and Co-Sensitization Strategy,” *International Conference on Electronic Materials and Nanotechnology for Green Environment (ENGE2016)*. Jeju, Korea, November 6-9, 2016.
4. Sangheon Lee, Joseph C. Flanagan, **Joonhyeon Kang**, Jinhyun Kim, Moonsub Shim, and Byungwoo Park, “Integration of II-VI Nanorods in Sensitized Photovoltaics via Open-Structured Photoanode and Co-Sensitization Strategy,” *Global Photovoltaic Conference 2015 (GPVC2015)*. Busan, Korea, November 15-20, 2015.
5. Sungun Wi, **Joonhyeon Kang**, Jaewon Kim, Hyungsub Woo, Sangheon Lee, and Byungwoo Park, “Reduced Graphene Oxide/Carbon Double-Coated 3-D Porous  $\text{LiMn}_{0.8}\text{Fe}_{0.2}\text{PO}_4$  Aggregates as High-Rate Cathode Materials for Li-Ion Battery,” *Materials Research Society (MRS) Spring Meeting*. San Francisco, CA, April 2015.

6. Hongsik Choi, Sangheon Lee, Taehyun Hwang, Seunghoon Nam, **Joonhyeon Kang**, Byungho Lee, and Byungwoo Park, “The Construction of Tandem Dye-Sensitized Solar Cells from Chemically-Derived Nanoporous Photoelectrodes,” *Materials Research Society (MRS) Spring Meeting*. San Francisco, CA, April 2015.
7. Woojin Lee, Taehyun Hwang, Seung-Yoon Lee, **Joonhyeon Kang**, Taeho Moon, and Byungwoo Park, “Organic-Acid Texturing of Transparent Electrodes Toward Broadband Light Trapping in Thin-Film Solar Cells,” *Materials Research Society (MRS) Spring Meeting*. San Francisco, CA, April 2015.
8. Seunghoon Nam, Jaewon Kim, Seung Jae Yang, Sangheon Lee, **Joonhyeon Kang**, Jun Young Oh, Chong Rae Park, Taeho Moon, Kyu Tae Lee, and Byungwoo Park, “Smart Wrapping Strategy for SnO<sub>2</sub> with Porosity-Tuned Graphene for High Rate Lithium-Anodic Performance,” *Materials Research Society (MRS) Spring Meeting*. San Francisco, CA, April 2015.
9. Seunghoon Nam, Sangheon Lee, Jaewon Kim, **Joonhyeon Kang**, and Byungwoo Park, “Smart Wrapping Strategy for SnO<sub>2</sub> with Porosity-Tuned Graphene for High Rate Lithium-Anodic Performance,” *International Conference on Electronic Materials and Nanotechnology for Green Environment (ENGE2014)*. Jeju, Korea, November 16-19, 2014.
10. Hongsik Choi, Taehyun Hwang, Sangheon Lee, Seunghoon Nam, **Joonhyeon Kang**, Byungho Lee, and Byungwoo Park, “The Construction of Tandem Dye-Sensitized Solar Cells from Chemically-Derived Nanoporous Photoelectrodes,” *International Conference on Electronic Materials and Nanotechnology for Green Environment (ENGE2014)*. Jeju, Korea, November 16-19, 2014.

11. Woojin Lee, Taehyun Hwang, Seung-Yoon Lee, **Joonhyeon Kang**, Taeho Moon, and Byungwoo Park, “Organic-Acid Texturing of Transparent Electrodes Toward Broadband Light Trapping in Thin-Film Solar Cells,” *International Conference on Electronic Materials and Nanotechnology for Green Environment (ENGE2014)*. Jeju, Korea, November 16-19, 2014.
12. Sungun Wi, Seunghoon Nam, **Joonhyeon Kang**, Jaewon Kim, Hyungsub Woo, and Byungwoo Park, “Reduced Graphene Oxide/Carbon Double-Coated 3-D Porous  $\text{LiMn}_{0.8}\text{Fe}_{0.2}\text{PO}_4$  Aggregates as High-Rate Cathode Materials for Li-Ion Battery,” *International Conference on Electronic Materials and Nanotechnology for Green Environment (ENGE2014)*. Jeju, Korea, November 16-19, 2014.
13. Yuhong Oh, Seunghoon Nam, Sungun Wi, **Joonhyeon Kang**, Taehyun Hwang, Sangheon Lee, Jordi Cabana, Chunjoong Kim, and Byungwoo Park, “Inexpensive Wrapping of Graphene on Individual  $\text{Li}_4\text{Ti}_5\text{O}_{12}$  Grains for Superior-Rate Li-Ion Batteries,” *Materials Research Society (MRS) Fall Meeting*. Boston, MA, December 2013.
14. Yuhong Oh, Seunghoon Nam, Sungun Wi, **Joonhyeon Kang**, Taehyun Hwang, Sangheon Lee, and Byungwoo Park, “Inexpensive Wrapping of Graphene on Individual  $\text{Li}_4\text{Ti}_5\text{O}_{12}$  Grains for Superior-Rate Li-Ion Batteries,” *The 9th Tsinghua University - University of Tokyo - Seoul National University Student Workshop*. Seoul, Korea, October 9-12, 2013.
15. Byungwoo Park, Hongsik Choi, Jae Ik Kim, Seunghoon Nam, Woojin Lee, Sungun Wi, Chohui Kim, and **Joonhyeon Kang**, “Nanoscale Interface Control for Photoluminescence and Solar-Cell Applications,” *The 9th Tsinghua University - University of Tokyo - Seoul National University Student Workshop*. Seoul, Korea, October 9-12, 2013.

16. Woojin Lee, Jae Ik Kim, Seung-Yoon Lee, Jongmin Kim, **Joonhyeon Kang**, Suji Kang, Taeho Moon, and Byungwoo Park, "Light Scattering Behavior of Highly Textured ZnO:Al Thin Films by Oxalic and Hydrochloric Acids," *Materials Research Society (MRS) Fall Meeting*. Boston, MA, November 2012.
17. Woojin Lee, Jae Ik Kim, Seung-Yoon Lee, Jongmin Kim, **Joonhyeon Kang**, Suji Kang, Taeho Moon, and Byungwoo Park, "Light Scattering Behavior of Highly Textured ZnO:Al Thin Films by Oxalic and Hydrochloric Acids," *Global Photovoltaic Conference 2012 (GPVC2012)*. Busan, Korea, November 19-21, 2012.
18. Hongsik Choi, Jongmin Kim, Changwoo Nahm, Chohui Kim, Seunghoon Nam, **Joonhyeon Kang**, Byungho Lee, and Byungwoo Park, "Improved Photovoltaic Performance of CdS Quantum-Dot-Sensitized Solar Cell through ZnO Coating," *The 13th Korea - Japan Student Symposium (Seoul National University - Tohoku University)*. Seoul, Korea, November 7-9, 2012.
19. Woojin Lee, Jae Ik Kim, Seung-Yoon Lee, Jongmin Kim, **Joonhyeon Kang**, Suji Kang, Taeho Moon, and Byungwoo Park, "Light Scattering Behavior of Highly Textured ZnO:Al Thin Films by Oxalic and Hydrochloric Acids," *The 13th Korea - Japan Student Symposium (Seoul National University - Tohoku University)*. Seoul, Korea, November 7-9, 2012.
20. Sujin Byun, **Joonhyeon Kang**, Yuhong Oh, Suji Kang, and Byungwoo Park, "Oxygen Reduction on Gold/Cerium Phosphate Electrocatalyst for Alkaline Fuel Cells," *The 13th Korea - Japan Student Symposium (Seoul National University - Tohoku University)*. Seoul, Korea, November 7-9, 2012.
21. Sungjun Lee, Jongmin Kim, Hongsik Choi, Woojin Lee, **Joonhyeon Kang**, Suji Kang, and Byungwoo Park, "Post-Annealing Effects on the Structural and Optical Properties of Zn(S,O) Thin Films," *The 13th Korea - Japan Student Symposium (Seoul National University - Tohoku University)*. Seoul, Korea, November 7-9, 2012.

## 국문 초록

최근 우리 사회의 에너지 의존도가 급격하게 증가하고 있는 가운데, 가장 중요한 천연자원인 석유의 매장량은 점차 감소하고 있으며, 머지 않아 고갈될 것으로 예상되고 있다. 또한 급속한 산업화에 따른 자동차, 발전소, 공장 등에 의한 각종 화석연료 사용량의 증가는 온실효과 및 지구온난화 현상을 초래함으로써 인간의 생존을 위협해 오고 있다. 이러한 상황에서 친환경적 전력원인 태양전지, 연료전지, 리튬 이온 전지 등에 대한 전세계적인 관심과 수요는 꾸준히 증가하고 있으며, 특히 이를 이용하는 전기 자동차, 하이브리드 전기 자동차 등이 기존의 화석 연료 기반의 자동차들을 효과적으로 대체할 수 있다면 에너지원의 고갈과 지구온난화 현상과 같은 문제들을 해결할 수 있을 것으로 기대되고 있다. 전기자동차로의 완전한 전환을 위해서는 긴 주행거리와 안정성이 보장되어야 하며, 이는 전기 화학 시스템 및 전극 물질의 특성에 의해 결정되지만, 현재의 리튬 이온 전지의 기술 수준으로는 이를 만족 시키기 어려운 실정이다.

이의 대안으로서 금속 공기 전지와 연료 전지는 기본적으로 금속 (또는 수소)과 산소 사이의 화학 반응을 통해 유사한 방식으로 작동한다. 이러한 전기화학 시스템은 경량 원소 간의 반응을 기반으로 하기 때문에 양극에 무거운 전이 금속을 포함하는 리튬 이온 전지에 비해 이론적인 에너지 밀도가 상대적으로 높다. 각 시스템의 양극에서는 산소 환원 반응이 공통적으로 일어나므로 이러한 발전된 전기화학 기술을 실현하기 위해서는 산소 환원 반응에 대한 근본적인 이해가 필요하다.

연료 전지와 금속 공기 전지 중 하나인 리튬 공기 전지 시스템은 산소 환원 반응을 공통적으로 이용하지만 상세한 반응 메커니즘과 생성물의 종류 및 이에 따른 전기화학적 특성은 매우 상이하다. 따라서 이러한

시스템으로부터 높은 에너지 밀도와 안정성을 확보하기 위해서는 각 시스템에 대한 이해와 이를 바탕으로 한 전략적인 접근이 필요할 것이다.

본 논문에서는 수용성 및 비수용성 전해질에서의 산소환원반응 메커니즘에 대한 근본적인 이해를 바탕으로 연료 전지 및 리튬 공기 전지에 알맞은 전극의 설계 방향을 제안한다. 두 시스템 모두 산소를 연료로 사용하며 전극 특성에 크게 의존하는 촉매 반응을 포함하지만, 사용되는 전해질과 생성물은 전혀 다른 특성을 갖는다. 연료 전지의 경우 산소 환원 반응을 통해 수용성 전해질에 용해되는 물을 생성하지만, 비수용성 전해질을 사용하는 리튬 공기 전지는 방전시 불용성 고체인 과산화 리튬을 양극 표면에 축적시키게 된다. 따라서, 각 시스템은 전기 화학적 성능을 향상시키기 위해 상이한 전략을 필요로 한다.

1 장에서는 촉매 반응과 연료 전지에 대한 기본 개념을 소개하며, 산소 환원 반응 및 메탄올 산화 반응에 대한 촉매 특성을 향상시키기 위한 전략을 제시한다. 다음으로는 리튬 공기 전지에 대한 간략한 소개와 함께 수용성/비수용성 전해질에서의 산소환원반응의 차이점을 중심으로 연료전지와 리튬 공기 전지를 비교하고자 한다. 마지막으로, 현재 리튬 공기 전지의 중요한 문제들과 이를 극복하기 위한 다양한 해결책을 제시한다.

2 장에서는 촉매 반응 및 촉매의 역할에 대한 이해를 위해 백금 표면의 전자 구조를 변화시키면서 메탄올 산화 반응에 대한 촉매 특성 변화를 관찰하고자 하였다. 이를 위해, 백금전극의 전위를 체계적으로 제어하고, 메탄올 산화 반응의 경로를 단순화시킴으로써, 불필요한 영향을 배제하고 백금 표면의 전자 구조에 의한 메탄올탈수소화반응의 활성화도 변화를 관찰할 수 있었다. 관찰한 바에 의하면, 백금의 메탄올 탈수소소화 활성화는 페르미 준위에 대한 백금 촉매의 d 밴드 중심의 위치가 낮을 때 감소하며, 이러한

상호관계는 직접 메탄을 연료의 음극으로서 최적화된 촉매를 설계하고자 할 때에 필요한 기본 원리를 제공할 것이다.

3 장에서는 앞서 다룬 연료 전지의 촉매 반응에 대한 이해를 바탕으로 하되, 리튬 공기 전지의 독특한 메커니즘을 고려하여 고효율, 고수명의 리튬 공기 전지용 양극을 설계하고자 하였다. 부반응에 취약한 탄소 및 바인더를 포함하지 않는 양극물질로서 이산화 티타늄을 이용하였고, 수소 열처리를 통해 계층적으로 배열된 다공성 구조를 갖는 전극을 개발하였다. 이러한 구조의 전극은 산소 공극 또는 +3 가의 티타늄 이온으로부터 유도된 높은 전자 전도성과 함께 전극의 막힘 현상 없이 반응 분자들이 신속하게 확산되고 반응하며 방전 생성물을 효과적으로 수용할 수 있는 마이크론 크기의 공극과 넓은 표면적을 갖는다. 마지막으로, 이러한 전극 구조에 용해성 촉매를 적용함으로써, 기존에 문제가 되고 있는 충전시 과전압 증가와 수명 단축 현상을 효과적으로 해결할 수 있었다.

**주요어:** 연료전지, 리튬 공기 전지, 산소 환원 반응, 촉매 반응, 촉매, 전이 금속, 수용성 전해질, 비수용성 전해질, 백금, 전자 구조, 메탄올 탈수소화 반응, 방전, 충전, 양극, 이산화 티타늄, 용해성 촉매

**학번:** 2010-20574